Argon oxy-hydrogen combustion for power generation employing Linear Joule Cycle Engine Generator

Thesis by

Ugochukwu Charles Ngwaka

In Partial Fulfilment of the Requirements

for the Degree of

Doctor of Philosophy

School of Engineering
Mechanical Engineering
Newcastle University
United Kingdom

January 2021

Abstract

The global awareness of the unfavourable environmental effects due to fossil fuels' continuous use as the primary energy source has increased significantly. In order to tackle the adverse environmental consequences, innovative technologies will play a significant role. As a result, this thesis presents an investigation of the Linear Joule Engine Generator (LJEG) and its potential for zero-emissions power generation. It is believed that the results of the investigation will guide the further development of the LJEG. A background study on LJEG related technologies was conducted, focusing on the challenges and advantages of the reciprocating Joule Cycle engine and the free-piston engine generator. The semi-closed cycle argon-oxy-hydrogen combustion LJEG was identified as the potential technology path towards LJEG development. This version of LJEG operated on dry friction principle, and an accurate friction model is required for a proper analysis of the engine. A novel friction model of the LJEG is proposed, and the proposed model validation was against test data from a lab-scale LJEG prototype. The dynamic and thermodynamic model of the LJEG was developed, and the numeric model validation was executed with the prototype's test data. The performance characteristics of the LJEG with different inputs and operating conditions were analysed. Results indicated that the friction model and the dynamic and thermodynamic model were reliable. The performance indicators of the LJEG depended on the input and operational parameters, and the most essential included the working fluid type, cycle pressure, valve timing, and electric load. The valve timing and electric load are optimised depending on preference between engine efficiency and power output. Operational parameter optimisation indicated that the efficiency decreased with extended expander intake duration but could improve with extended expander exhaust duration. Power output increased with longer expander intake duration; however, its relationship with compressor/expander diameter ratio (CER) depended on adopted expander exhaust duration. Substituting air with argon as the major working fluid resulted in over 60% improved indicated efficiency, and peak efficiencies of 40% and 60% are achieved with CER of 0.70 and 0.93, respectively. However, there could be a need for further fluid flow investigation; since the working volume of the expander and compressor is not fixed but could vary according to operation, and the fluid flow in the LJEG is pulsating.

Acknowledgments

I want to thank my first supervision team, Professor Tony Roskilly, Dr Dawei Wu, and Dr Andrew Smallbone, for their guidance, support, and encouragement in the PhD journey.

I want to express my appreciation and thanks to my second supervision team, Dr Julian Happian-Smith, Dr Serkan Turkmen and Dr Dehong Huo; your input, support and sacrifice, is well appreciated.

Dr Boru Jia, thanks for giving me a good start; your input was a relief source during this journey's early days. Special thanks to Mr Ben Towell, Mr Chris Lawrence and Mr Ian Douglass for their support and work on the prototype.

Many thanks to Sir Joseph Swan Centre for Energy Research staff, especially Dr Yaodong Wang, Mrs Jan Fairless and Mr John Richardson.

I am indebted to my wife, Amaa, for her affection, support, sacrifice and endurance. I will not forget to thank my kids for their interesting distractions; it could not have been this fun without them. Many thanks to my parents, siblings and friends for their various supports, I appreciate.

All the Glory be to God for the great things He is doing.

Publications

Publications related to this research and included in the thesis:

I. Ugochukwu Ngwaka, Dawei Wu, Julian Happian-Smith, Boru Jia, Andrew Smallbone, Chidiebere Diyoke, and Anthony Paul Roskilly. "Parametric analysis of a semi-closed-loop linear joule engine generator using argon and oxy-hydrogen combustion." *Energy* 217 (2021): 119357. https://doi.org/10.1016/j.energy.2020.119357

II. Ugochukwu Ngwaka, Boru Jia, Christopher Lawrence, Dawei Wu, Andrew Smallbone, and Anthony Paul Roskilly. "The characteristics of a Linear Joule Engine Generator operating on a dry friction principle." *Applied energy* 237 (2019): 49-59. https://doi.org/10.1016/j.apenergy.2018.12.081

III. Jia, Boru, Dawei Wu, Andrew Smallbone, Ugochukwu Ngwaka, and Anthony Paul Roskilly. "Dynamic and thermodynamic characteristics of a linear Joule engine generator with different operating conditions." *Energy conversion and management* 173 (2018): 375-382. https://doi.org/10.1016/j.enconman.2018.07.098

Publications related to this research but not included in the thesis:

IV. Ugochukwu Ngwaka, Andrew Smallbone, Boru Jia, Christopher Lawrence, Ben Towell, Sumit Roy, K. V. Shivaprasad, and Anthony Paul Roskilly. "Evaluation of performance characteristics of a novel hydrogen-fuelled free-piston engine generator." *International Journal of Hydrogen Energy* (2020). https://doi.org/10.1016/j.ijhydene.2020.02.072

The link between the publications and content of the thesis

Publication (i): A greater content of this publication could be found in Chapter 8 of the thesis.

Publication (ii): Greater content of this publication could be found in Chapter 7 of the thesis.

Publication (iii): Some of the content of this publication could be found in Chapters 5 and 6 of the thesis.

Contents

List of Figures

List of Tables

Nomenclature

A	Condenser total heat transfer area (m^2)
a_1	Friction parameter (-)
a_2	Friction parameter (-)
A_c	Compressor piston area (m^2)
A_d	Reference flow area (m^2)
A_e	Expander piston area (m^2)
A_{re}	Reactor surface area (m^2)
c	Damping coefficient (-)
C_d	Discharge coefficient (-)
$F(t)$	Excitation force (N)
$\overrightarrow{F_e}$	Pressure force from linear expander (N)
$\overrightarrow{F_{el}}$	Pressure force from left chamber of the expander (N)
$\overrightarrow{F_{er}}$	Pressure force from right chamber of the expander (N)
$\overrightarrow{F_c}$	Pressure force from linear compressor (N)
$\overrightarrow{F_{cl}}$	Pressure force from left chamber of the compressor (N)
$\overrightarrow{F_{cr}}$	Pressure force from right chamber of the compressor (N)
F_f	Friction force (N)
F_{fd}	Dry contact friction force (N)
F_{fl}	Friction force relative to retardation phase (N)
F_{fp}	Pressure friction force (N)
F_{fu}	Friction force relative to acceleration phase (N)
$\overrightarrow{F_g}$	Generator force (N)
F_{net}	Resultant force (N)
f	Friction function (-)
f_s	Static friction coefficient (-)
f_d	Dynamic friction coefficient (-)
G	Linear generator load constant (N/(m·s^{-1})
h	Coefficient of heat transfer in the expander (W/m^2·K)
h_a	Enthalpy of argon flowing into the condenser (J/kg)

h_{ac}	Enthalpy of argon flowing out of the condenser (J/kg)
h_{cw}	Enthalpy of water flowing out of the condenser (J/kg)
h_e	Specific enthalpy of the mass flow through the expander (J/kg)
h_{in}	Specific enthalpy of the intake gas to the reactor (J/kg)
h_s	Enthalpy of saturated steam flowing into the condenser (J/kg)
h_{out}	Specific enthalpy of the exhaust gas from the reactor (J/kg)
k	Spring constant (-)
L	Length (m)
m	Moving mass (kg)
$\dot{m}$	Mass flowrate through valves (kg/s)
$\dot{m}_a$	Argon content flowing into the condenser (kg/s)
$\dot{m}_c$	Mass flowrate through the compressor (kg/s)
$\dot{m}_{cf}$	Condenser cooling fluid flow rate (kg/s)
$\dot{m}_f$	Mass flowrate of the hydrogen injected to the reactor (kg/s)
$\dot{m}_e$	Mass flowrate through the expander (kg/s)
$\dot{m}_{in}$	Mass flow into the reactor (kg/s)
$\dot{m}_s$	Steam flowing into the condenser (kg/s)
$\dot{m}_{out}$	Mass flowrate out of the reactor (kg/s)
N	Ring normal pressure force (N)
P_a	Atmospheric pressure (bar)
p_c	Pressure in the compressor (Pa)
p_{cl}	Pressure in the left compressor (Pa)
p_{cr}	Pressure in the right compressor (Pa)
p_d	Downstream pressure (Pa)
p_e	Pressure in the expander (Pa)
p_{el}	Pressure in the left expander (Pa)
p_{er}	Pressure in the right expander (Pa)
p_u	Upstream pressure (Pa)
$p_{i/o}$	Suction or discharge compressor fluid pressure (Pa)
P	Generator power output (W)
Pd	Product

$\dot{Q}$	Heat duty (J/s)
$\dot{Q}_{add}$	Heat addition (J/s)
$\dot{Q}_{cf}$	Condenser cooling fluid heat absorption quantity (J/s)
$\dot{Q}_{h}$	Heat flow rate (J/s)
$\dot{Q}_{ht}$	Heat transfer from the reactor to the environment (J/s)
Q_{fuel}	Energy carried in fuel (W)
$\dot{Q}_{rx}$	Heat of reaction (J/s)
R	Gas constant (J/kgK)
Re	Reagent
T_0	Temperature of the environment (K)
T_{cfo}	Condenser outlet temperature of the cooling fluid (K)
T_{cfi}	Condenser inlet temperature of the cooling fluid (K)
T_c	Average outlet temperature of the fluid flowing out of the condenser (K)
T_{in}	Temperature of the intake mass flow into the reactor (K)
T_{out}	Temperature of the exhaust mass flow out of the reactor (K)
T_{re}	Temperature in the reactor (K)
T_u	Temperature of upstream (K)
T_w	Average surface temperature of expander cylinder wall (K)
x	Piston displacement (m)
$\dot{x}$	Piston sliding velocity $(\mathrm{m/s})$
$\dot{x}_m$	Mean piston velocity $(\mathrm{m/s})$
$\ddot{x}$	Piston acceleration $(^{\mathrm{m}}/_{\mathrm{s}^2})$
$\ddot{x}_m$	Mean piston acceleration $(^{\mathrm{m}}/_{\mathrm{s}^2})$
U	Overall heat transfer coefficient (W/K·m^2)
V	Instantaneous cylinder volume (m^3)
V_c	Working volume of linear compressor (m^3)
V_e	Working volume of linear expander (m^3)
z_1	Friction parameter (-)
z_2	Friction parameter (-)
α	Coefficient of the reactor heat transfer (W/K·m^2)

γ	Heat capacity ratio (-)
ΔT_{lm}	The logarithmic mean temperature difference (K)
η	System efficiency (%)
$\rho_{i/o}$	Suction/discharge compressor fluid density $(\mathrm{kg/m^3})$

Abbreviations

ArH_2R	Argon-Hydrogen Reactor
BDC	Bottom Dead Centre
CER	Compressor/Expander diameter Ratio
CHP	Combined Heat and Power
ECU	Engine Control Unit
EEVC	Expander Exhaust Valve Closing
EEVO	Expander Exhaust Valve Opening
EIVC	Expander Intake Valve Closing
EIVO	Expander Intake Valve Opening
EVC	Exhaust Valve Closing
EVO	Exhaust Valve Opening
GLC	Generator load coefficient
IVC	Intake Valve Closing
ICE	Internal Combustion Engine
IVO	Intake Valve Opening
LEG	Linear Electric Generators
LJEG	Linear Joule Engine Generator
NOx	Oxides of Nitrogen
RJCE	Reciprocating Joule Cycle Engines
SP	Specific Power
TDC	Top Dead Centre

Chapter 1: General introduction

1.1 Background

There has been a significant increase in global awareness within the public, scientific community, governmental institutions and industrial sector on the adverse environmental effects resulting from the continuous use of fossil fuels as the primary energy source. The use of these fossil fuels has been unprecedented because of the need to satisfy the ever-growing energy demand caused by the human population and economic growth and development. The world annual energy consumption increased by 2.3% in 2018, and it is expected to continue increasing in the foreseeable future [1]; however, fossil fuels energy sources accounted for 82% of the total global energy consumption in 2018 [2]. The transportation and electricity generation sector was responsible for 33% of the global energy consumed in 2018 [2]. Studies carried out by ExxonMobil [3], BP [4], and International Energy Agency (IEA) [1] indicated that there would be continuous growth in energy demands for the transportation and power generation sector in the near future. This implied that if fossil fuels continue to be the primary energy source, the associated environmental impact both for the local pollutants, which pose health risks to humans, such as carbon monoxide, oxides of nitrogen and particulates, and carbon dioxide (CO_2), would be of immediate concern. According to recent studies, the global average CO_2 concentration increased by 45% since the mid-18th century, from 280 parts per million (ppm) [5] to 406 ppm as of 2017 [6]. Subsequently, the global energy-related CO_2 emissions increased by 1.7% in 2018 [1], to 35 Gt, and it has been estimated that the global energy-related CO_2 emissions would increase at an average rate of 0.6% per year between now and 2050 [2]. The increase in emissions of CO_2 from the combustion of fossil fuels has led to an increasing concern about global warming [7]-[8]. The presence of a high concentration of CO_2 and other greenhouse gases in the Earth's atmosphere has been linked to a series of ecological and environmental problems, including desertification, global warming, and ocean acidification.

Recently, many governments worldwide have come up with environmental legislation to tackle energy-related emissions and mitigate the threat posed by global warming. In order to comply with emissions regulations, some alternative technologies have been proposed to tackle the environmental impact of emissions from fossil fuels, and adopting alternative fuels would be one of them [9]-[10]. Hydrogen is among the alternative fuels; it is the most abundant element on earth and can be considered a potential “endless” energy source [11]. Hydrogen has the advantages of high efficiency and ultra-low combustion emissions in engine applications [12]. As a result of hydrogen fuel advantages, it is considered an ideal fuel to power unconventional technologies like the Linear Joule Engine Generator.

The concept of the Linear Joule Engine Generator (LJEG) was first proposed in 2012 by Mikalsen and Roskilly [13] for potential application in micro-scale Combined Heat and Power (CHP) systems. In 2014, Wu and Roskilly [14] presented the first preliminary design of the LJEG for power generation and carried out a parametric analysis of the engine components; since then, an open cycle prototype of the LJEG has been developed and tested successfully at Newcastle University [15]. The LJEG combined the principles of the Reciprocating Joule Cycle Engines (RJCE) and Linear Electric Generators (LEG). The configuration of an LJEG makes it easily adapted to almost any type of fuel without any need for significant engine modification. The external combustion made the LJEG more adaptable to different combustion modes that could reduce oxides of nitrogen (NOx) and particulate matter (PM) emissions without any need for significant engine modification [16]. This ease of adaptability makes the LJEG a potentially credible technology for a zero-carbon power source in a future hydrogen economy.

There has been some research interest in RJCE related technologies some years ago from Plymouth University UK [17], The Polytechnic University of Hauts-de-France [18] and Newcastle University UK [19] [20]. However, most of the existing research on RJCE and LEG focused on engine development and performance predictions based on open-loop air-standard technology. Very few studies have investigated the semi-closed cycle LJEG and the use of zero-carbon fuels in any of the combined technologies. This research investigates the technical feasibility and performance of a zero-carbon semi-closed-loop LJEG using hydrogen fuel and continuous external combustion for heat addition and noble gas as the primary working fluid. The proposed choice of noble-gas-oxy-hydrogen combustion in the semi-closed-loop LJEG eliminates the oxides of nitrogen and carbon emissions and improved efficiency. The research seeks to answer the following questions;

what is the technical feasibility of the engine-generator, what would be the system performance and output, what would be the main variable/s that would influence the system operation, and how could the system be optimised for better performance and output. In order to achieve zero-carbon emissions, it is believed that electrolysis driven production of hydrogen and oxygen from water offered a means to use low-cost excess electricity and utilise this energy when required with no carbon emissions. This excess electricity to hydrogen and oxygen via electrolysis is a strong candidate for scaling up energy storage capacity. Target applications for LJEG powered by hydrogen and oxygen produced via electrolysis include:

1. Emergency/uninterrupted power systems: The variability in renewable sources for power generation currently presented a problem. Zero emission LJEG was an option to smooth the variability in renewable sources and for peak-shaving application.
2. On-board vehicle range-extender/generator: The LJEG presents an opportunity to refuel a vehicle rapidly and thus extending the operating range by generating electricity on-demand or charging battery on-board vehicles.
3. Micro Combined Heat and Power (µCHP): The LJEG was a strong complementary technology to this and could be used as a conventional CHP system powered with renewable energy and yielding no local exhaust gas emissions.
4. Auxiliary Power Unit (APU): Rather than being used to power propulsion on-board vehicles, a smaller unit could power on-board systems at high efficiency on aircraft, ships or on other more extensive forms of transport.

1.2 Research aim and objectives

This research focused on Linear Joule Cycle Engine Generator; it aimed to develop a semi-closed cycle Linear Joule Cycle Engine Generator, which uses noble gas as the primary working fluid and powered by hydrogen and oxygen reaction. The main objectives of the study were as follows:

1. Understand and analyse the friction characteristics of a dry lubrication LJEG and develop a numerical friction sub-model for the LJEG; this friction sub-model would be integrated into the LJEG dynamic and thermodynamic model.

2. Develop an advanced complete cycle numerical model for the semi-closed cycle zero-emissions noble gas-oxy-hydrogen powered Linear Joule Engine Generator and validate the LJEG model against test results.
3. Investigate the characteristics and the performance of the LJEG to identify factors and variables that would influence the engine operation.
4. Examine the influence of design, input and operational variables on the performance of the LJEG through sensitivity analysis and analyse what performance improvements could be obtained through the implementation of technologies appropriate to larger-scale systems.

1.3 Structure of the Text

The flowchart showing the arrangement of this thesis and the relationship between each chapter is shown in *Figure 1*. The main contents of the thesis were organised in chapters, and the brief contents of the chapters are described as follows:

- Chapter 2 presents a comprehensive background study of the state of the art of reciprocating Joule cycle technology, free piston engine technology, and the use of noble gas as working fluid in hydrogen-fuelled engines, evaluating reported applications and their performance.
- Chapter 3 presents the methodology adopted in this research.
- Chapter 4 discusses the engine configuration, test rig description and operation, and data acquisition and processing.

- Chapter 5 presents the full-cycle model development of the LJEG; the full-cycle model constitutes the combustion, dynamic and thermodynamic models developed to investigate the technical feasibility of the engine operation.
- Chapter 6 presents the full-cycle numerical model validation; simulation results are presented, showing the operational characteristics of the LJEG, along with the influence of the main engine design and operational variables.
- Chapter 7 investigates the friction characteristics of an LJEG and presents a novel numerical friction sub-model for the LJEG. The developed numerical friction model validation was carried out with test data from the LJEG test rig.

- Chapter 8 investigates the performance and parametric analysis of the LJEG. The performance and stability response of the LJEG resulting from changes in the operational and geometric variables were analysed. The potential advantage of the coupling of the multiple LJEG was investigated.
- Chapter 9 presents the summary and conclusions of the whole thesis, the results were summarised and evaluated, and discussions on further works were suggested.

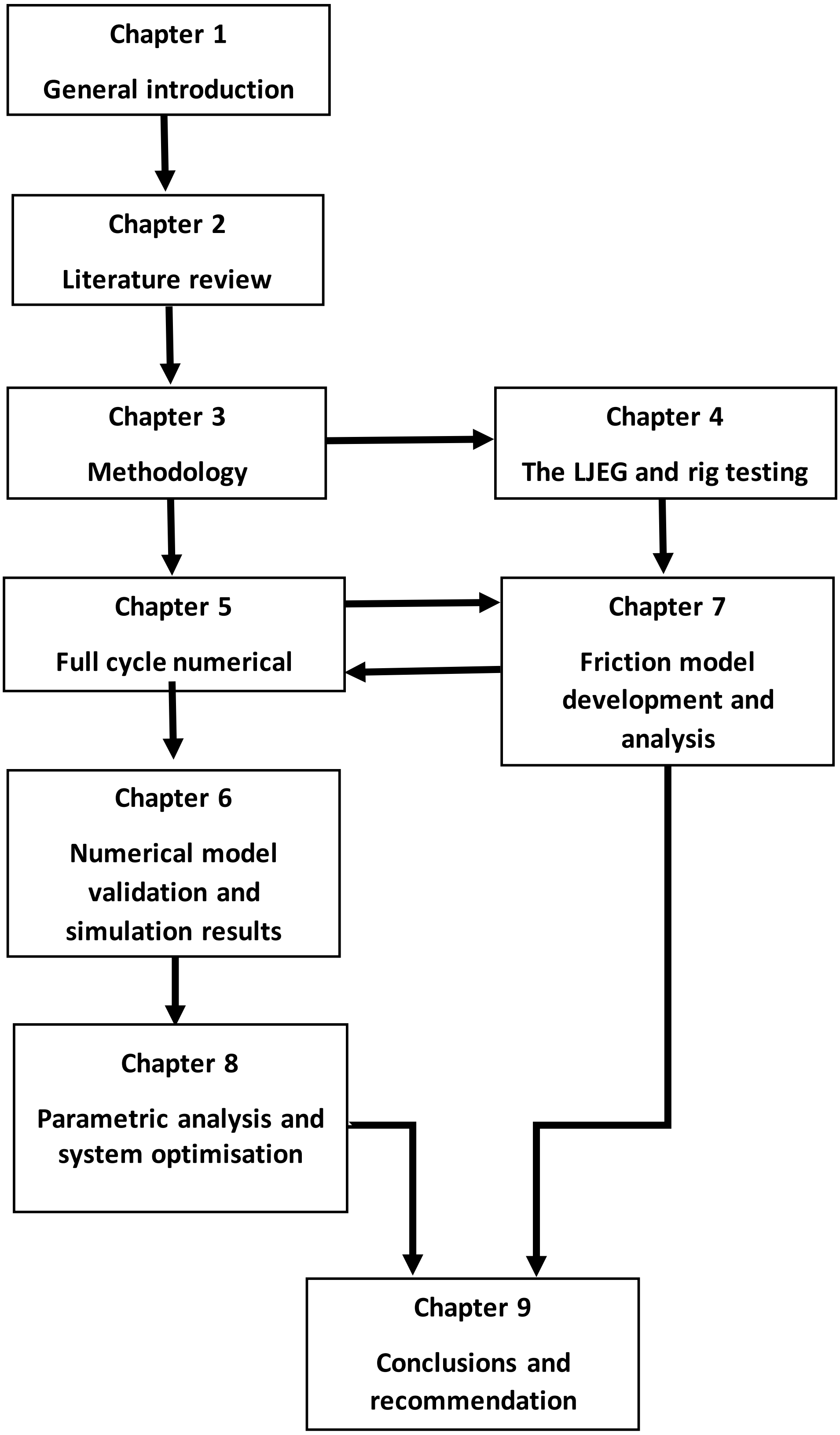

Figure 1-1. Flowchart showing the arrangement of this thesis and the relationship between chapters

Chapter 2: Literature review

2.1 Introduction

The United Nations Framework Convention on Climate Change Treaty adopted in December 2015 in Paris set a global target to keep a global temperature rise this century to well below 2 degrees Celsius above pre-industrial levels and afterwards to 1.5 degrees Celsius [21]. This agreement seems to have encouraged great responses from some governments and the industrial sector to reduce carbon emissions. In 2019, the UK became one of the first major economies to pass laws to bring all its greenhouse gas emissions to net-zero by 2050 [22]. Perhaps, achieving this target would require accelerated development and implementation of innovative decarbonisation technologies. In order to achieve the net-zero emissions target, the main choices available are energy efficiency improvement, sustainable use of biomass, carbon capture and storage, and renewable energy sources [23]. Renewable energy sourced hydrogen could play a significant role in revolutionary decarbonisation technologies, and this is because it could be accomplished with net-zero emissions.

J O Bockris was among the early scholars to present the idea of adopting hydrogen as a replacement for conventional fossil fuels in the 1970s [24] [25]. The concept involved using piped hydrogen as fuel in the industrial sector, transportation sector, and household energy and termed the scenario a "hydrogen economy" [26]. Since then, the global demand for hydrogen has increased four-fold from 18.2 mega tonnes in 1975 to 73.9 mega tonnes in 2018 [27]. The International Energy Agency (IEA) studies considered that between 2025 and 2050, that hydrogen production in the EU4 would exceed 120 TWh [28]. This would represent a systematic shift towards the so-called “Hydrogen Economy” driven by the UK government’s commitment to expanding the mix of renewable energy and thus the need to offset renewable energy supply and demand intermittency. The industry automotive roadmaps [29] anticipated that passenger vehicles will not commit to purely electric solutions but prefer the flexibility of on-board range extenders. The Low Carbon Partnership [30] estimated that the most feasible path to the decarbonisation of the heavy-duty truck industry was the use of hydrogen as fuel.

At the time of writing, the research interest on hydrogen production technology was diverse and ranged from fossil fuel resources, nuclear energy, and undoubtedly many renewable energy sources. A few mature and several developing hydrogen production technologies existed, and the widely used technologies included fossil-fuel steam reforming, partial oxidation, autothermal reforming, gasification of solid fuels, electrolysis of water and industrial residual hydrogen [31]. Hydrogen production technology could be categorised into fossil fuel-based and renewable-based. The majority of hydrogen production comes from fossil fuel sources, and hydrogen production from fossil fuel sources accounted for 96% of the commercial hydrogen. In contrast, water electrolysis accounted for 4% [32]. In 2018, renewably sourced hydrogen produced was 0.37 mega tonnes, representing more than 0.5% of the total hydrogen demand that year [27]. However, it is expected by 2030 that renewably sourced hydrogen production could reach 7.9 mega tonnes, representing about 10% of the global demand in 2030 [33].

At the moment, hydrogen fuel cell systems, which convert the chemical energy of hydrogen and oxygen into electrical energy, is the most widely available hydrogen power generation technology [34]. Nevertheless, the definite requirement for high-purity hydrogen in the fuel cell system to prevent catalyst poisoning and efficiency decline could be of concern, as well as low power densities encountered in fuel cell systems [35]. With the increasing demands in electricity generation in transportation, industries and domestic use, and the net-zero emissions requirement, there is a great need to develop an alternative and innovative hydrogen-fuelled power generation technology to compete with the hydrogen fuel cells. Therefore, this research is focusing on the use of hydrogen for power generation in the LJEG.

2.1.1 Summary

The commercially available hydrogen production technologies include fossil fuel steam reforming and partial oxidation, biomass gasification, and water electrolysis [36] [37]. Steam reforming and partial oxidation are the most widely established hydrogen production technologies and are more economically feasible than the others are, but they have a comparably high carbon footprint [38] [39]. However, it is believed that hydrogen produced through electrolysis would increase significantly in future if electricity from renewable sources became increasingly available [31] [40]. The argon-oxy-hydrogen LJEG engine would be powered by electrolysis driven production of hydrogen and oxygen from water. This would use an off-peak renewable source of electricity, as it seems to be the reasonable means commercially available to produce large quantities of hydrogen and oxygen without a significant carbon footprint or by-products associated with fossil fuels. Consequently, off-peak renewable sourced electricity-powered electrolysis is the only probable technology path at the moment for the required oxygen and hydrogen for the LJEG.

As mentioned section 1.1 that the LJEG is considered to combine the principles of the Reciprocating Joule Cycle Engines (RJCE) and Free Piston Engine Generator (FPEG); the next three sections of this Chapter discuss the literature of the FPEG technology, the RJCE and noble gas circulation in hydrogen fuelled combustion, respectively.

2.2 Free-Piston Engine Technology

Pescara proposed the concept of the free-piston engine (FPE) in the 1920s for air compression applications, and a patent for spark ignition and compression ignition types were registered in 1927 [41] and 1928 [42], respectively. However, research on FPE was active until the early 1960s, and lately, there has been renewed attention by researchers in the development of FPE. Several research groups have reported on various prototypes and their test results [43]. The recent interest in FPE was attributed to advances made in system control and real-time actuation technologies and the strict emission standard imposed by some governments [44]; they have enabled the FPE to become a feasible future technology.

In FPE, the piston assembly moved in a free linear motion between the operating top dead centre (OTDC) and the operating bottom dead centre (OBDC). Gas and load forces acting upon the piston/s controlled the piston assembly motion. The mechanical energy generated by the back and forth movement of the piston assembly could be used by any relevant target application/load. As any physical boundary did not restrict the motion of the piston assembly, the demand for a crankshaft mechanism was eliminated [45]. Due to the elimination of the crankshaft mechanism, no side forces act between the piston and cylinder liner, and frictional losses are lower [46]. Some of the advantages of FPE over traditional piston engines included its simple mechanical structure, with very few moving parts; this made FPE compact with a potentially high power-density [47], and it is understood to have higher efficiency than a traditional piston engine of comparable size [48]. Furthermore, the FPE could operate with a variable compression ratio; this advantage made the use of alternative fuels possible [43].

The FPE could be categorised according to its form of energy input. Therefore, two distinct categories of FPF existed; the internally powered free-piston engines (IPFPE) and the externally powered free-piston engines (EPFPF). The IPFPE are the internal combustion free-piston engines, which produced the pressure energy inside the piston cylinder. In contrast, in the EPFPE, the pressure energy was produced externally and supplied to the piston cylinder.

Several concepts of IPFPE have been developed over time for different purposes, which included the free-piston engine compressor (FPEC), the free-piston engine gas generator (FPEGG), the free-piston engine linear generator (FPELG), and the hydraulic free-piston engine (HFPE).

The free-piston engine compressor (FPEC) was among the first successful applications of the FPE technology and was the first version initially developed by Pescara [41]. The FPEC used the mechanical energy obtained from the piston assembly to power a compressor.

The free-piston engine gas generator (FPEGG) seemed to be the most successful FPE application to date. FPEGG used the exhaust gas from the FPE to drive a gas turbine and generate mechanical power. SIGMA GS-34 was one of the reported engines developed that worked on the principles of FPEGG [49].

The free-piston engine linear generator (FPELG) combined FPE with a linear electric generator. The generator was used to harvest the mechanical energy from the piston assembly and convert the energy to electricity. FPELG has been proposed for advanced power sources and hybrid electric vehicles [50].

The hydraulic free-piston engine (HFPE) combined FPE with a hydraulic system: the mechanical energy of the piston assembly was converted into hydraulic energy. HFPE technology is being proposed for hydraulic powered systems [51].

Externally powered free-piston engines (EPFPE) seemed to be a relatively new technology with one of the early documented reports published in 1999 [52]. However, this thesis mainly focused on externally powered free-piston engine technology; therefore, more attention was paid to recent developments in EPFPE in the next section.

2.2.1 Externally Powered Free-Piston Engines

Alan Kornhauser conducted a fundamental design and developed the dynamic and thermodynamic model of a double-acting free-piston expander coupled to a double-acting free-piston compressor in Matlab [53]. The fundamental results revealed that most of the design characteristics were dependent on the cycle pressure ratio, intake and exhaust valve timing and the specific heat ratio of the working fluid. The author affirmed that for an efficient engine to be developed, the engines' expanders and compressors would operate with dead volume, exhibit mechanical friction and heat transfer losses, and losses in the valves would be inevitable.

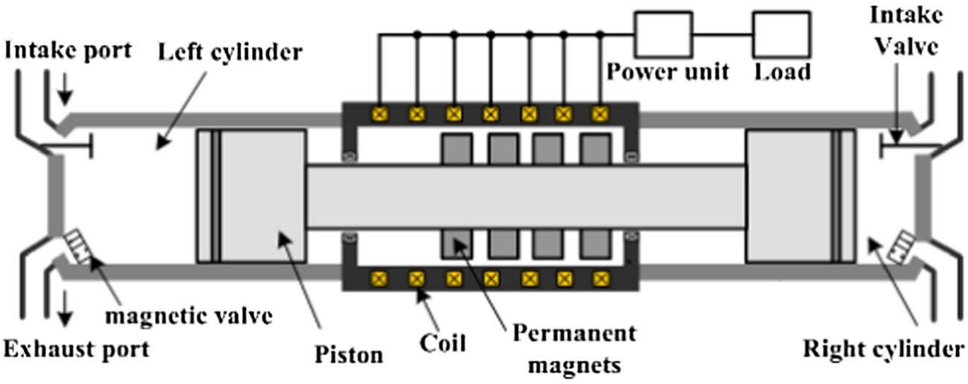

Figure 2-1. Configuration of free-piston linear expander [47].

A team from Newcastle University experimentally investigated the characteristics of a two-stroke air-driven free-piston linear expander designed to use low-grade heat for electric power generation [47]. The engine configuration is shown in Figure 2-1, it consisted of dual pistons in two different cylinders and connected by a rod in a linear structure and a permanent magnet linear generator installed on the connecting rod. Compressed air, supplied by an external compressor, was used as the energy source that drove the expansion process alternatively in each cylinder. The test results showed that the peak voltage, piston assembly peak velocity and energy conversion efficiency exhibited a linear relationship with the driven pressure. The operation frequency increased with the driven pressure but seemed more sensitive to the pressure at the relatively low-pressure region. Similarly, the output voltage was sensitive to the piston assembly velocity. The energy conversion efficiency increased with pressure and could reach up to 55% with a pressure of 3.75 bar.

Xu et al. [54] developed an integrated model of the two-stroke compressed air driven free-piston linear expander generator reported in [47] in Matlab/Simulink, and the influences of the geometric and operating variables on the system performance were investigated. The results indicated that the voltage, stroke, frequency, generator efficiency and conversion efficiency increased with the intake pressure. The efficiency of the generator decreased with increased load, and the power output increased with pressure but decreased with the load. The simulation results suggested that the peak intake pressure should be limited to 4 bar to avoid the risk of the piston colliding with the cylinder head. However, at 4 bar, the optimal generator conversion and electrical efficiencies were 93.6% and 45.6%, respectively.

Researchers from Xi'an Jiaotong University presented a design and a prototype of a double-acting free-piston expander. The schematic of the air test rig is shown in Figure 2-2, and the expander prototype is shown in Figure 2-3. An expander powered auxiliary compressor was connected directly to the expander. The auxiliary compressor was arranged in parallel with the primary compressor for work recovery in the trans-critical CO_2 cycle [55]. The test prototype was validated using an air test. The slider-based inlet and outlet control strategy was adopted to realise the expansion process in the expander. The prototype operation was stable at a wide range of pressure ratios. The test results showed that the isentropic expander indicated efficiency calculated using the pressure and volume (P~V) diagram to be around 62% at a 2.36 pressure ratio.

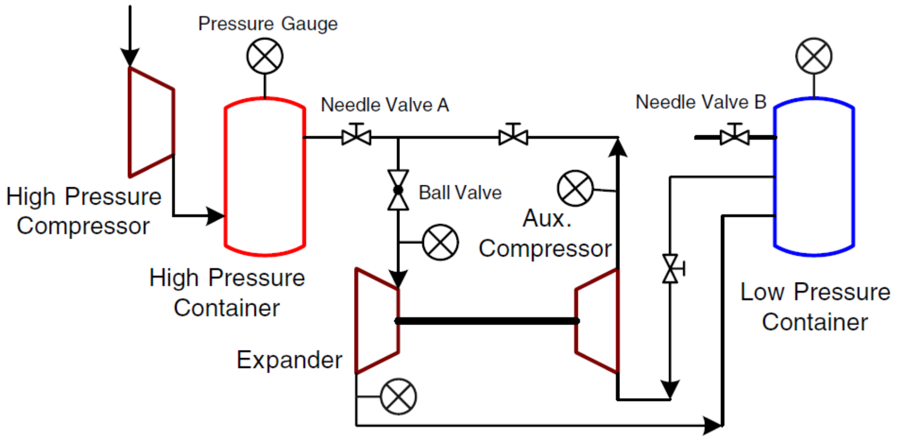

Figure 2-2. Schematic of the air test rig for the free-piston expander [55].

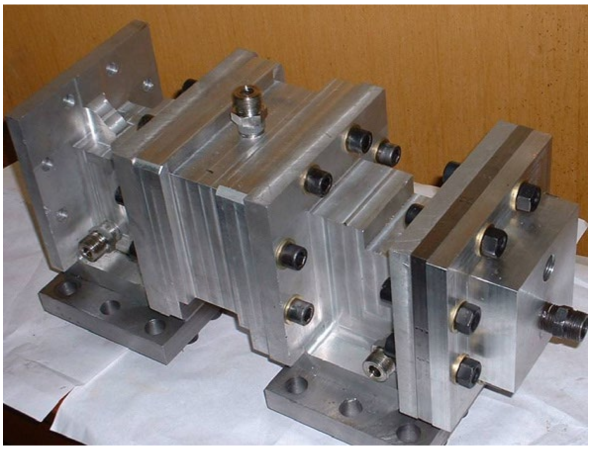

Figure 2-3. The double acting free piston expander prototype [55].

Researchers from the University of Notre Dame examined a closed cycle small-scale free piston expander (in micro-electromechanical system range) to convert low-temperature waste heat sources into usable power [56]. The reciprocating action of the expander was achieved by the expansion of the working fluid at the minimum cycle volume generated by external thermal energy input on the contact surface, and the expander design was based on the sliding piston concept. The essential design and operating parameters that could affect the system performance were selected, including external load, piston mass, input heat rate and duration of heat input, and parametric sweeping to identify the optimal performance. The simulation results indicated that increased heat input in the expander increased the power output but decreased the operating frequency. The simulated efficiency was between 0.1 and 0.2%. The low efficiency was associated with small heat input resulting in a peak pressure of 1.08 bar and low operating temperature gradients of about 5 ^{o}K.

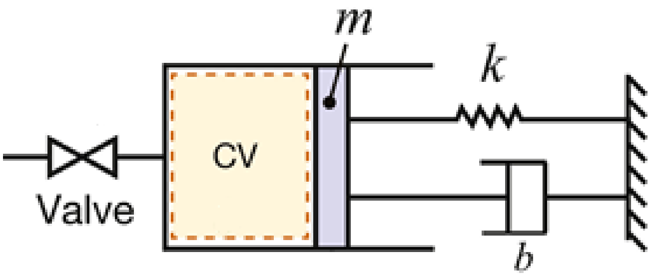

Figure 2-4. Schematic sketch of the open cycle mini FPE [57].

The research team further investigated the characteristics and performance of an open cycle centimetre scale free-piston expander through physics-based models [57] [58]. The authors adopted the simplified spring-mass-damper free-piston engine analysis in developing the engine model, and hot compressed air was the working fluid. The schematic sketch of the mini engine design is shown in Figure 2-4, and it consisted of a single-piston cylinder, a damper and a bounce chamber. CV denotes control volume, k is the spring constant, b is the damping coefficient, and m is piston assembly mass. The valve was used for both the injection and exhaust of the working fluid. The simulation results identified the essential parameters that positively affected the engine's performance, and they include; higher intake pressure, longer intake duration, lower loads, and larger piston assembly mass and softer springs. However, the intake pressure and the intake duration were identified as the most critical performance parameters that significantly influenced the power output and efficiency of the engine. The simulation predicted indicated efficiency of 18% at peak intake pressure, temperature and load of 2.5 bar, 373 K and 7 N-s/m, respectively [57]. Analysis of results indicated that for a fixed intake duration, increased intake working fluid temperature did not significantly affect engine efficiency, and there was an optimal intake duration, which maximised energy conversion efficiency. Equally, using higher specific heat ratio fluid led to proportional improved system efficiency in the engine [58].

A research group from Jilin University presented a design of an organic Rankine cycle (ORC) coupled with a free-piston compressor. It developed a simulation model of the engine in GT-suite to predict the characteristics of the system under various working conditions [59] [60]. The system was designed to recover waste heat from exhaust gas generated by a stationary compressed natural gas-powered internal combustion engine compressor and assist in compressing the natural gas from about 4 bar to 14 bar. The schematic diagram of the ORC free-piston compressor is shown in Figure 2-5, and it consisted of a double-acting free-piston expander placed in-between two single-acting piston compressors, an evaporator, a condenser and working fluid pumps and tanks. Superheated vapour was injected into either side of the expander and flash boiled into supersaturated vapour. At the same time, it produced expansion in the expander, and the same procedure was carried out at the other side of the expander to produce a continuous back and forth movement of the expander piston. The expander piston rod was connected to the two compressor pistons at both ends to produce compression alternatively on the two compressors while the double-acting expander piston reciprocated. Analysis of the simulation parametric sweep results indicated that optimal performance was obtained when the ratio of the expander area to the compressor area was 2.5 and the compressor output pressure was at 11 bar. The system achieved an indicated efficiency of 53.2% at these given operating conditions, and the effective efficiency was 26.5% [60].

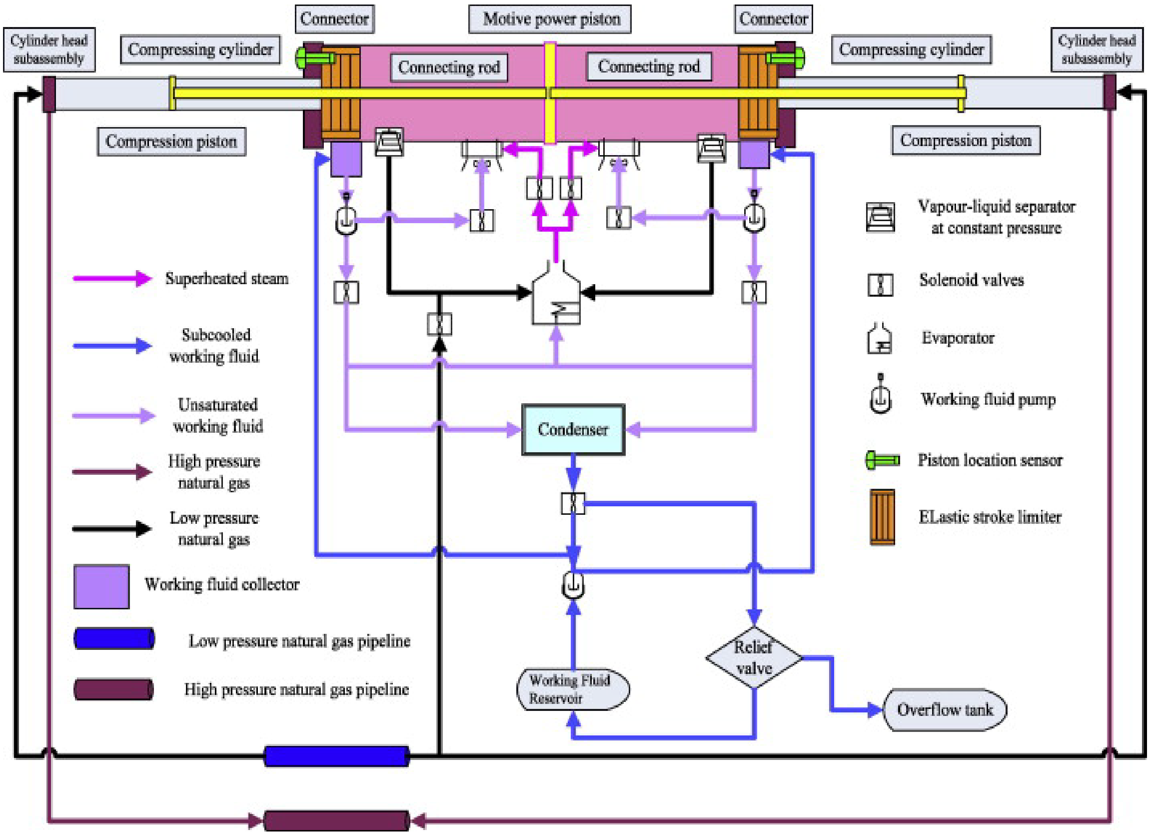

Figure 2-5. Schematic diagram of the ORC-Free-Piston Compressor [59].

Researchers from the Beijing University of Technology built a free-piston expander-linear generator test rig suitable for a small-scale organic Rankine cycle waste heat recovery. The team further developed dynamic and thermodynamic numerical models of the engine to investigate the dynamics and performance characteristics of the engine at various operating settings. The picture of the engine and the schematic diagram of the test rig is shown in Figure 2-6 and Figure 2-7, respectively. The engine comprises dual pistons in two separate cylinders and is connected by a rod in a linear structure and a linear generator installed on the connecting rod. Air was used as a working fluid and was supplied by an external compressor, and compressed air was the energy source that drove the expansion process alternatively in each cylinder.

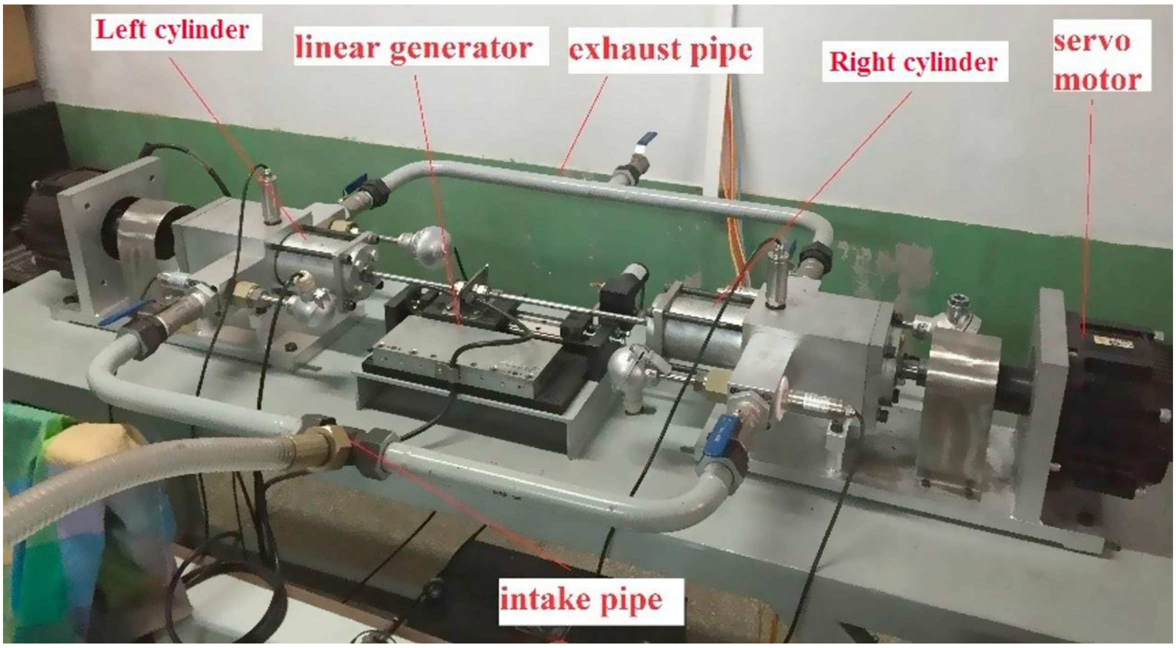

Figure 2-6. Picture of the free-piston expander linear generator (FPE-LG) prototype [61].

The test results revealed that the piston assembly moved at a high and relatively constant speed at the middle stroke portion. Intake pressure and valve timing significantly influenced the engine's piston assembly dynamics and power output [62] [61]. The indicated efficiency decreased with increased intake pressure, and the motion stability of the engine improved with increased intake pressure [61], [63]. Investigations into valve timing operation indicated that expander recompression resulted in improved power output, and optimal performance at different valve timing varied depending on the operating frequency. The power output increased with the intake pressure, and peak power was realised at peak velocity [64]. Increased operation frequency resulted in decreased piston amplitude and motion symmetry. It occurred because whilst the operation frequency increased, the intake duration would continue to decrease, which would result in the reduction in the quantity of compressed air intake per cycle. The conversion efficiency of the engine increased with the intake pressure. At a frequency of 2.0 Hz and intake pressure of 2.6 bar, the engine achieved an electrical conversion efficiency of 45.82% and a power output of over 64 W [65].

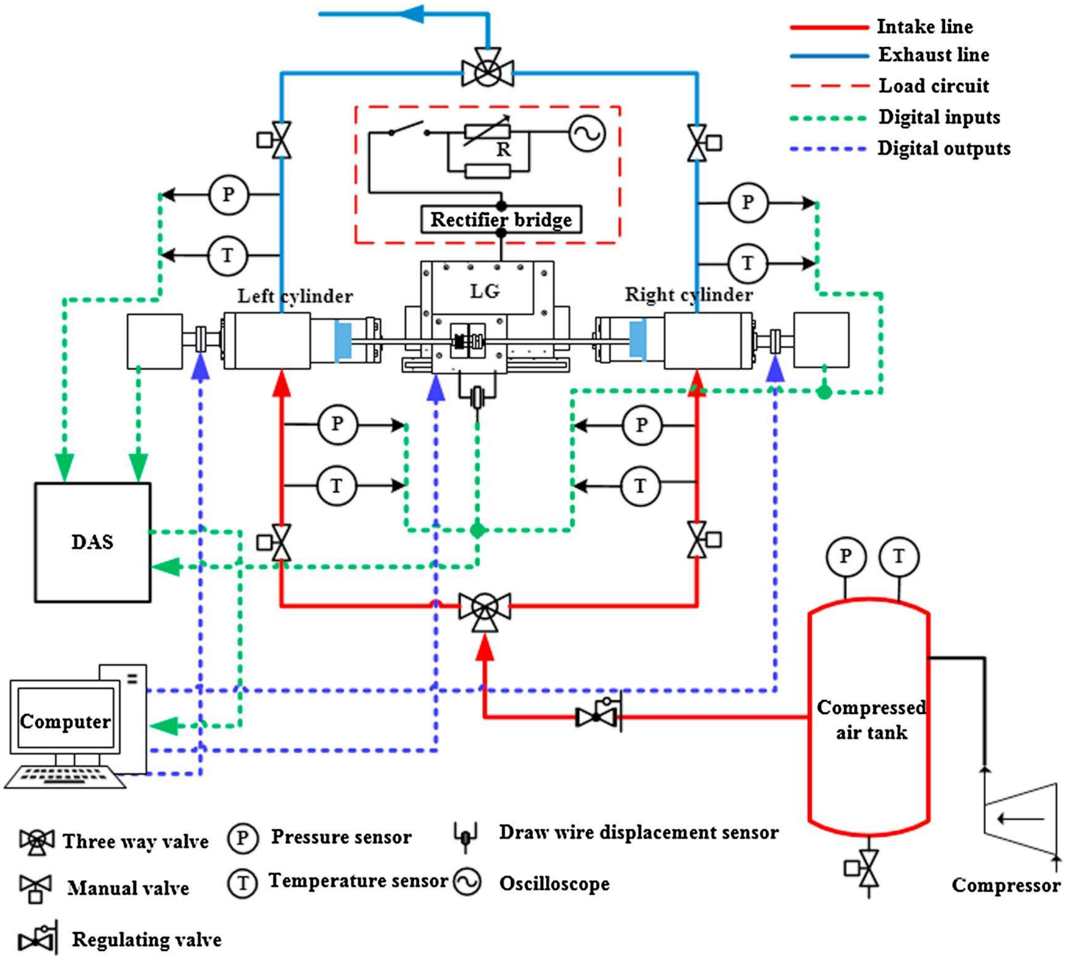

Figure 2-7. The schematic diagram of the FPE-LG test rig [61].

Further investigation revealed that at a relatively high intake pressure of 10 bar and an operating frequency of 15 Hz, the peak power output of 676W was achieved [66]. The power output increased with external load up to a particular load and remained nearly constant after that. The efficiency increased with external load up to the optimal load and decreased afterwards [67]. Investigations on the influence of intake temperature revealed that the peak power output increased with intake temperature [68]. Finally, the team recommended the proper sizing of the linear generator for operation stability and performance enhancement [69].

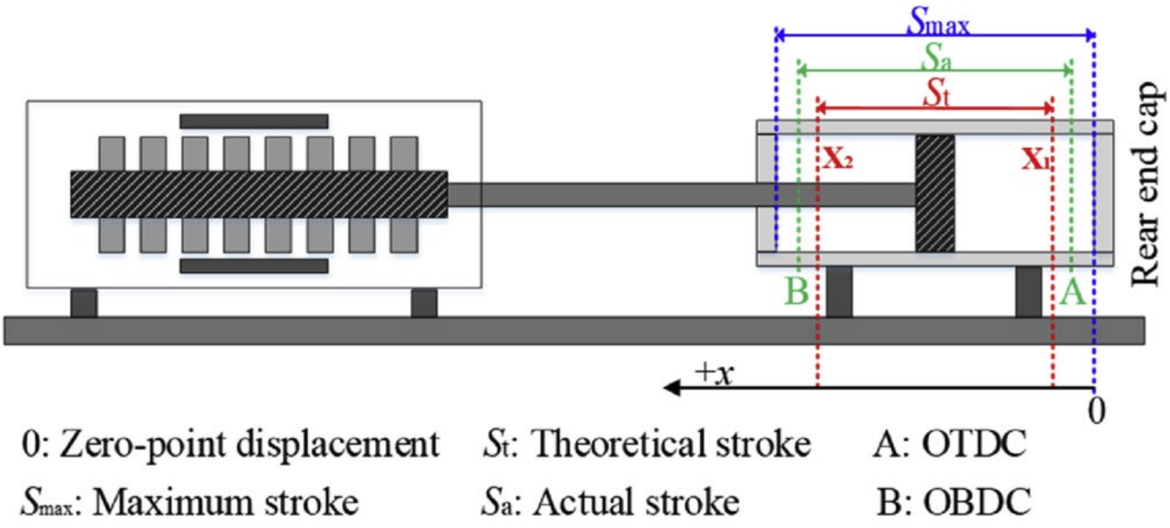

Figure 2-8. Schematic diagram of single-piston FPE-LG [70].

The same research group from the Beijing University of Technology proposed a double-acting free-piston expander generator and developed an air test rig to investigate its characteristics. The schematic diagram of single-piston FPE-LG is shown in Figure 2-8, and the test rig consisted of an externally powered air compressor, a single double-acting free piston in a cylinder at one end and a linear generator at the opposite end. Both the double-acting piston and the generator were linked by a connecting rod. Analysis of the test results indicated that most of the characteristics exhibited by the double cylinder free-piston expander generator type were observed in the single cylinder double-acting free-piston type [71]. Nevertheless, the peak power and indicated efficiency increased linearly with intake duration and, the double-acting free-piston expander type appeared to have a relatively lower efficiency [72], [70].

2.2.2 Summary

The externally powered free-piston engine seems to have received a fewer research interest compared with the internal combustion free-piston engines counterparts. However, in the last four years, interests in EPFPE have grown considerably, especially for applications in waste heat recovery, gas compression and power generation. Most of the air-standard experimental studies reported a stable operation and attractive conversion efficiencies. It would be reasonable to think that since air-standard tests were stable and exhibited attractive efficiencies, using noble gas with a higher specific heats ratio would support stable operation and probably greater efficiencies.

2.3 Reciprocating Joule Cycle Engine

The Reciprocating Joule Cycle (RJC) engine was first proposed by Warren and Bjerkle in 1969 [73], and the engine was aimed for automotive application. The proposed open cycle engine could be arranged in a V-engine or in-line engine configuration with even numbers of cylinders for an equal number of compressors and expanders. The results suggested that the engine could be compact, operate with improved fuel economy between 20% and 30%, and produce fewer emissions than the traditional internal combustion engines.

In 1984, Decher [74] presented a different design version of the Joule Cycle engine. The design used positive displacement compressors and expanders, and the engine was called the “Britalus engine”. The pistons were encased within the cam and execute a simple harmonic motion with the aid of a three-lobed cam, a rotor and a central manifold. The reciprocating action of the pistons in their respective cylinders was produced when the pistons contacted the inside surface of the cam while the rotor turned around the manifold. The engine design seemed promising based on an air cycle analysis. It was reported that the compression and expansion adiabatic efficiencies of the engine as configured were excellent at all load conditions. The author suggested that improved performance would be obtained by increasing the expander intake temperature. The use of ceramic materials in some vital parts of the engine to withstand high operating temperature was recommended.

In 1989, Tsongas and White developed a thermodynamic numerical model based on an air-standard open Joule cycle, without regeneration, to predict a Joule Cycle Engine's thermodynamic performance with reciprocating piston compressor expander components [75]. The model incorporated the major irreversibilities applicable to such engines, including friction, heat transfer, pressure and mass losses. The results based on the Britalus engine concept identified the maximum temperature, the compressor speed, and the pressure ratio as the key operating parameters. The authors predicted an indicated efficiency of 38%; however, it was emphasised that friction and heat transfer must be determined experimentally if accurate model results are expected. It suggested that such a model could be used to perform a preliminary engine design, and conduct parametric and sensitivity analyses to evaluate the influence of different parameters on engine performance.

Richard Rosa presented a design of a 100 kW closed-loop RJC engine [76] which could use high-grade fuel as well as low-grade fuels such as coal and any form of processed and unprocessed biomass. The design was meant to find its application in power trucks and tractors and stationary applications such as an irrigation pump. The proposed engine configuration is illustrated in Figure 2-9. The engine incorporated a cooler to cool the compressor inlet fluid and a regenerator to preheat inlet fluid. The vertically aligned compressor and expander were solidly coupled with a traditional crankshaft mechanism. The expander inlet temperatures and pressures were 1100 ^{o}K and 30.4 bar, respectively, and the engine cycle pressure ratio was fixed at 2.5, and air was the working fluid. A cycle indicated efficiency of 35% and power density of 0.361 kW/kg were achieved when the expander and compressor efficiencies were both 85%.

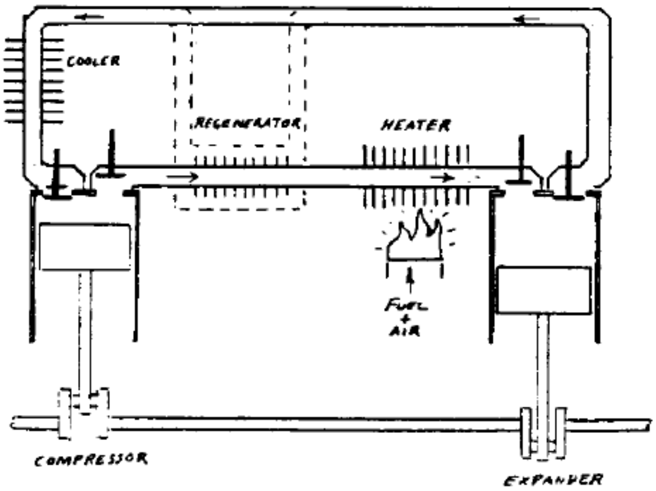

Figure 2-9. RJC engine configuration presented by Rosa [76].

In 1992 researchers from West Virginia University presented a design [77] and a numerical simulation model [78] of an ideal open-cycle air-standard model of the RJC engine. The proposed engine consisted of a piston compressor, a piston expander, termed power piston and a combustion zone. The pistons, which could be in multi-cylinder configurations, were operated on a common crankshaft mechanism. The ideal air-standard analysis of the engine operating with a pressure ratio of 48.5 [77] and 35.1 [78] showed that the indicated efficiency of the engine was between that of an ideal Joule and Diesel cycles. The optimum displacement ratio (ratio of expander piston displacement to that of the compressor displacement) was between 1.25 and 2.0. Analysis of the results showed that the ideal indicated efficiency increased with the pressure ratio. The design offered an additional degree of freedom due to the flexibility of the expansion ratio. However, the analysis did not consider the major engine irreversibilities such as heat loss, pressure losses, blow-by and friction.

In 2003 researchers from the University of Plymouth [17] presented a design and developed a steady-state thermodynamic model of an air-standard open-cycle RJC engine. The engine was proposed as a suitable prime mover for micro-CHP applications, small stand-alone power units and hybrid vehicles. Figure 2-10 shows the schematic of the proposed engine. The engine incorporated an external combustor to a parallel-aligned compressor and expander, coupled with a traditional crankshaft mechanism and a recuperator attached to the combustor inlet and expander exhaust. The RJC model incorporated the frictional losses, leakages and pressure drop losses. The model simulation results showed that the efficiency of the RJC engine was most significantly affected by the frictional losses within the engine and that losses due to leakage were less of a problem than the pressure drop losses. The results indicated that with the maximum design temperature fixed at 1300 ^{o}C, the nominal working pressure ratio at 7, and the ratio of expander to compressor swept volume fixed at 2.3, the electrical efficiency of 50% could be achieved without considering thermal losses. It was suggested that improved efficiency could be achieved by minimising the pistons sealing requirements to ensure a less frictional loss and that low frictional loss could be achieved by using a relatively low-pressure ratio.

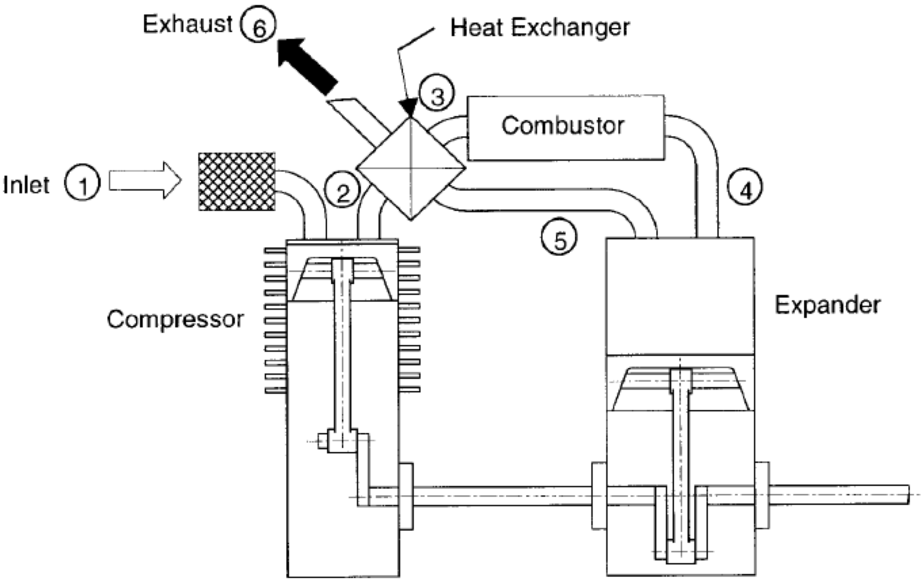

Figure 2-10. RJC engine configuration presented by Bell and Partridge [17].

In 2004 Moss, Roskilly and Nanda presented a 5 kWe design of an air-standard RJC engine for CHP application [19]. Figure 2-11 shows the configuration of the RJC engine, the pistons were in a V-cylinder pattern and linked with a crankshaft mechanism, and a recuperator attached to the combustor inlet and expander exhaust. The static model results proved that efficiency is maximised by high peak temperatures, high-pressure ratio and low engine speed. High temperatures were crucial for reliable system performance, but its application was limited by the availability of system components that could withstand such temperatures. Electrical efficiency of 35% and a thermal output of 8.12 kW could be achieved at a peak temperature of 1423 ^{o}K. In addition to the overall engine efficiency depending on the thermodynamic parameters, it was also strongly dependent on the frictional losses. The results suggested that any practical design would need to reduce friction loss where possible due to the low mean effective pressure of the cycle. Likewise, the cylinder clearance volumes should be kept as small as possible since this will improve the volumetric efficiency and minimises the required cylinder size.

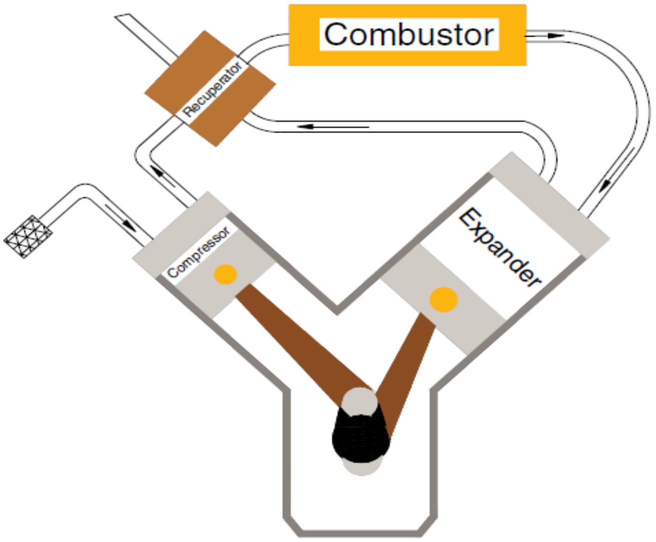

Figure 2-11. RJC engine configuration presented by Moss, Roskilly and Nanda [19].

In 2005 a research team from the University of Pau and the Adour Region, France, presented an energy, exergy and cost analysis of a natural gas-powered open-cycle air-standard RJC engine for micro-cogeneration applications [79]. The RJC design consisted of a two-stage compressor with a double-acting piston, a single-stage expander with a double-acting piston, a combustion chamber, a preheater, a heater, a recuperator and an inter-cooler. The results indicated that with the maximum operating temperature at 1373 ^{o}K, the nominal working pressure ratio at 6.0 and engine speed at 1000 rpm; indicated efficiency of over 40%, electrical efficiency of over 29% and combined efficiency of over 65% could be achieved [80]. Similarly, the same research team conducted a thermodynamic model investigation on the coupling of a two-stage parabolic trough solar concentrator with an open-cycle air-standard RJC engine for medium temperature CHP application in 2007 [81]. The design consisted of a single-stage compressor and expander, a solar heat source (heater) and a recuperator. The heater peak temperature and nominal working pressure ratio were 995 ^{o}K and 3.0, respectively. The thermodynamic performance results with reference to the heater thermal output produced an indicated efficiency of over 39%, electrical efficiency of 27% and combined efficiency of over 80%.

In 2010, Wojewoda and Kazimierski presented a dynamic model to describe the performance characteristics of an RJC engine [82]. The engine worked in a closed-cycle mode, and air was used as the working fluid. The proposed engine could find its use suitable for the propulsion of small ships and small nuclear submarines. The engine comprised an expander, a compressor, a heater, a cooler and, two recirculation blowers to enhance the rate of air circulation in the heat exchangers when the engine valves are closed. The compressor and expander were connected to a conventional crankshaft mechanism, and a traditional camshaft operated all the valves. The highly pressurised engine (compression from 17 to 95 bar) could produce over 25 kW power and achieve an electrical efficiency of up to 31% at an engine speed of 3000 rpm and maximum heater temperature of 1273 °K. The results indicated that the compressor/expander volume ratio for the optimal engine performance was considered to be about 0.75 when the heater volume is five times the expander volume.

Toure and Stouffs presented a steady-state thermodynamic model of an open-cycle air-standard RJC engine suitable for low power thermal energy conversion from renewable energy sources like biomass or solar energy [83]. The RJC design consisted of a compressor, an expander, a heater, and a recuperator. Parametric optimisation results showed that it was more beneficial to close the expander exhaust valve before TDC so that the expansion dead volume was recompressed to enhance the engine performances. The model simulation results indicated that with heater temperature at 900 °K, an indicated efficiency of over 46% could be achieved at a pressure ratio between 2.0 and 3.2 when the expansion dead volume was recompressed. Over 42% indicated efficiency could well be achieved if there was no recompression of expander dead volume. The compressor/expander volume ratio for optimal power output and indicated efficiency was estimated to be about 0.5 if there was recompression and about 0.56 when there was no recompression.

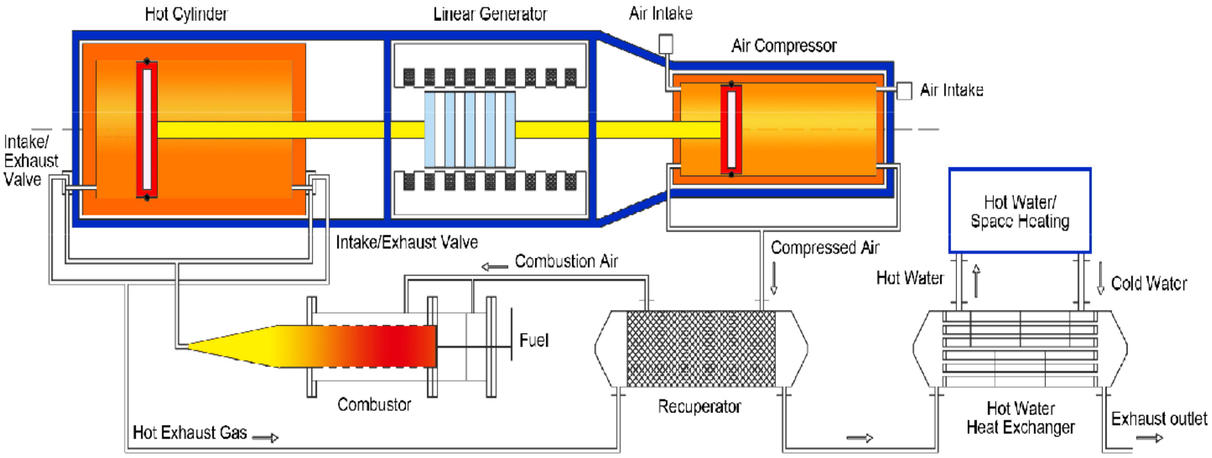

Figure 2-12. Free-piston reciprocating Joule cycle system for CHP applications [13].

Mikalsen and Roskilly took a different approach and incorporated free-piston technology in RJC engine design for CHP applications [13]. The engine design is shown in Figure 2-12, and it consisted of a double-acting free piston expander and compressor, a constant pressure external combustor and a recuperator. It reported that the availability of components that can withstand high temperatures, lightweight materials for the piston assembly components, lubrication and sealing could present problems in practical designs. The model simulation predicted an electrical efficiency of 32 % at a pressure ratio of 6.0 and a frequency of 36.4 Hz.

Lontsi et al. presented a dynamic model of an on open cycle, air standard RJC engine, suitable for small-scale solar energy conversion and micro-cogeneration using biomass or gas effluents at high temperatures applications. A thermodynamic performance analysis [84] and operational optimisation [85] were carried out through numerical model simulation. The modelled RJC configuration consisted of a compressor, an expander, a heater (heat exchanger), and the expander and compressor were linked with a crankshaft mechanism. The parameters defining the engine model specifications include; peak heater temperature of 873 ^{o}K, cycle pressure ratio of 4.0 and speed of 480 rpm. Simulation results showed that satisfactory stable performance could be achieved with regards to the RJC engine configuration without heat recovery. The results indicated that the engine could recover from disturbances (delay of closing the expansion cylinder inlet valve and compressor inlet pressure drop) after a rapid transient phase and quickly stabilise. Indicated efficiency of 29% was achieved without considering the heat losses, friction losses, pressure drop in the heater and the thermal inertia of metallic parts of the engine [85]. Similarly, an indicated efficiency of 23% was achieved without considering the heat losses and the thermal inertia in the heater [84]. The authors recommended using a regeneration cycle to recover the waste heat from hot gases downstream of the expander for improved engine performances.

Creyx et al. [18] presented a static thermodynamic model of an open cycle air-standard RJC engine suitable for micro-cogeneration applications and compared the results with available results in the literature. The RJC design consisted of a compressor, an expander and a heater. A conventional crankshaft mechanism connected the compressor and expander. Sensitive analysis was performed on the main engine parameters to determine the optimal working conditions, and incomplete expansion and expansion dead volume recompression was considered in the simulation. The simulation results revealed that incomplete expansion and expansion dead volume recompression would improve the engine performance. The engine frictional losses and pressure drop across the valves and the heater were not evaluated. Engine indicated efficiency of 37.6 % was achieved at a pressure ratio of 6.0, the heater peak temperature of 923 ^{o}K, engine speed of 600 rpm, 30% incomplete expansion and 28% expansion dead volume recompression. The same research team developed a dynamic model of the RJC engine for a domestic biomass micro-CHP using the Bond graph method [86]. The engine configuration and operation were the same as the study described in [18]. The influence of pressure and temperature on engine performance was evaluated at a temperature 823 ^{o}K. The results indicated that the optimal engine performance was achieved when the expander pressure is between 6 and 8 bar, at higher temperatures, and optimised expander intake and exhaust valve closing with an engine speed of about 800 rpm. Friction losses represent between 56 and 72% of the engine's indicated mean effective pressure (IMEP) for engine speed range between 600 and 1400 rpm, and friction losses seemed to increase with the rotational speed. However, it was suggested that it might be beneficial to incorporate a preheater to the RJC engine to enable increased energy flux supply to the expansion cylinder for improved system performance [87].

Stanciu and Bădescu investigated an open-cycle air-standard RJC engine coupled with a solar parabolic trough collector, and a dynamic model of the system was developed [88]. The RJC engine had a similar configuration to the one presented by Creyx et al. [86], and it was crankshaft operated. The results showed that the main parameters influencing the performance of the engine were the heat input, engine rotation speed, working fluid mass flow rates, and the expander inlet temperature and pressure. The authors identified that working fluid under-compression or over-expansion in the compressor cylinder and under-expansion or over-compression in the expander cylinder affected the operations of the RJC engine. This abnormal compression and expansion were attributed to the variation of working fluid temperatures in the heater (parabolic trough collector). The over-compression and over-expansion faults were fixed by either increasing the working fluid temperature inside the heater or decreasing the values of some geometrical parameters of the expander. It suggested that one of the ways to increase the heater temperature without recourse to the heat input was by decreasing the engine speed, thereby increasing the working fluid resident time in the heater. The engine performance results indicated that with the heater temperature at 800 ^{o}K, an indicated efficiency of over 26% could be achieved at a pressure ratio between 4.0 and 4.2 and an engine speed of 480 rpm.

Researchers from the University of Liège developed a prototype of an open-cycle air-standard RJC engine to be coupled with a biomass-fired heater for micro-CHP applications [89]. The schematic representation of the RJC test rig is shown in Figure 2-13. The engine was developed by modifying an existing 12-litre, 6-cylinder in-line internal combustion engine (ICE). Four of the cylinders operated in expander mode and two cylinders in compressor mode. An electrical air heater coupled with the engine mimics the biomass heater. A commercial compressor provided additional airflow. The engine was coupled to an induction machine, and the induction machine could work in either generator mode or motor mode. A preliminary investigation conducted on the prototype could not work as expected because the heater could not attain the design inlet temperature of the expander, which is 1073 ^{o}K. Secondly, there were high leakages in the compressor and expander cylinders, and the cut-off length of the expander was too long. The authors developed a semi-empirical model of the prototype, incorporated a commercial turbocharger in the model and operated all the cylinders in expander mode. The simulation results indicated that with a compressor supply pressure of 2 bar, an electrical efficiency of 6.5% and a combined efficiency of 70.5% was achieved.

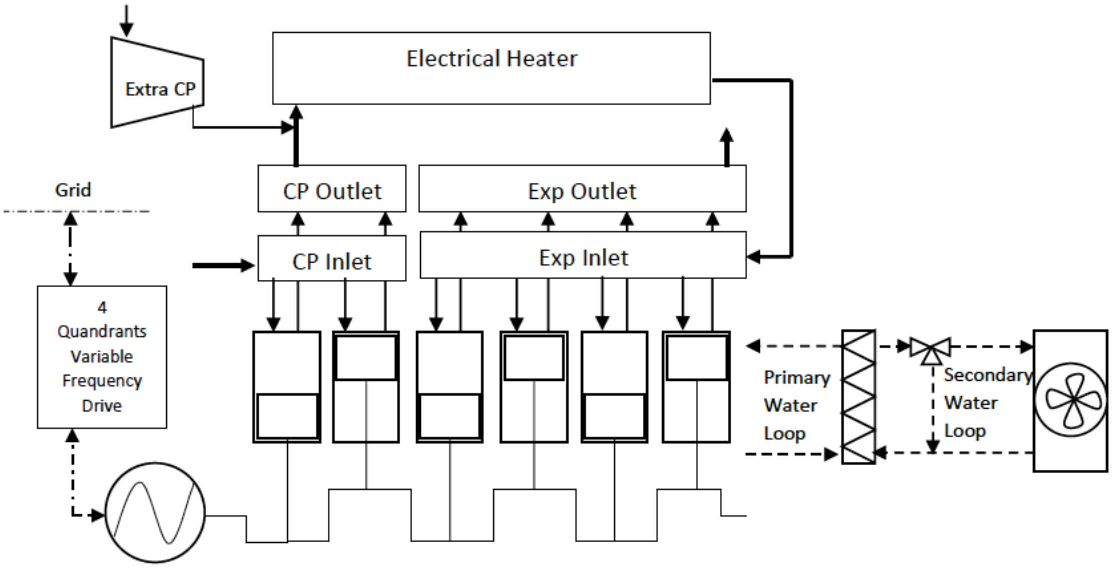

Figure 2-13. Schematic representation of the RJC test rig [89].

A team from the National Technical University of Athens presented an open-cycle air-standard RJC engine design [90]. The engine's main components were the compressor, heater, and expander, and the engine did not employ a regeneration process. A crankshaft mechanism drove the compressor and expander. Irreverserbilities such as pressure drops in the heater (heat exchanger), flow areas, and heat transfer were considered, but frictional losses were not considered in determining the engine performance. The focus of the study was on the effect of heat exchanger geometry and configuration and the influence of heat source temperature on engine performance. The simulation results of the heat exchanger configuration and geometry indicated that increasing the number of passes while maintaining the size of the heat exchanger transfer area improved the heat transfer rate, efficiency and power output. High-pressure drops on the hot side characterised an increase in the number of tubes passing. This implied that the hot side flow area's reduction caused by an increased number of tube passing must be offset; this offset could be achieved by decreasing the hot side flow path at each pass. The heat flow rate, the power output and the efficiency increased with heat source temperature.

Further investigation of compressor and expander valve timing on the performance and operating characteristics of the engine was conducted [91]. The results revealed that delay in closing the compressor exhaust valve could lead to increased compressor work and decreased expander work, leading to about a 10% decrease in power and efficiency. Also, advancing the expander exhaust valve opening from OBDC could lead to over 2.5% improvement in power and efficiency. However, the engine specific power output remains higher for retarded expander inlet valve closing timing.

Recently Ndame and Stouffs presented a design and a thermodynamic model of an open-cycle air-standard liquid piston RJC engine, suitable for low power solar energy conversion, micro-CHP applications and waste heat recovery [92]. The engine is composed of two compression and two expansion cylinders, consisting of a U-tube partly filled with water, a solid piston enclosed in each tube, a recuperator, a heater, a buffer tank and a flywheel mechanism. A solid cylinder head sealed the water surface in the upper part of the tube. Fundamentally, the system was composed of two RJC engines operating in phase opposition. The model simulation results showed that indicated efficiency of over 35% could be achieved with an expander inlet temperature of 633 ^{o}K, the pressure ratio of 3.0 and engine speed of 37.8 rpm. The results also revealed that the engine indicated efficiency decreased with increased engine rotation speed, and recompression of expansion dead volume seems to improve the engine performance.

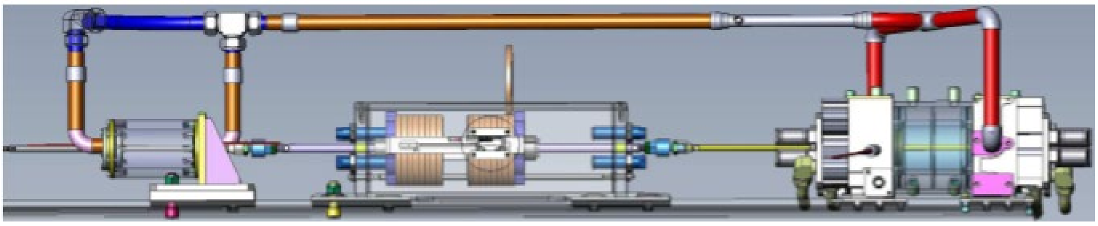

Figure 2-14. 3D design diagram of the Linear Joule-cycle Engine prototype [14].

Wu and Roskilly from Newcastle University [14] conducted a parametric study on an open cycle air standard linear Joule cycle engine through numerical model simulation. The 3D design picture of the engine is presented in Figure 2-14. The simulation result achieved an optimal electrical efficiency of 32 % at a peak temperature of 1073 ^{o}K, pressure ratio 5.9, engine speed 3.64 Hz and an expander to compressor volume ratio of 1.5. Wu et al. [93] presented a coupled dynamic model of the linear Joule cycle engine with an embedded permanent magnet linear alternator. The detailed sub-model of the linear alternator responding forces eliminated any underestimation of their impact on the kinetics of the moving mass. The coupled model also enabled an integrated design of the linear Joule engine and the linear alternator. The model simulation predicted an indicated efficiency of 34% and electrical efficiency of 30%.

2.3.1 Summary

Research interest in reciprocating Joule cycle engines has increased over the years. The technology seems attractive because of the reported performance output and the inherent external heat input ability; its heat input could be supplied by most conventional fuel sources, both processed and unprocessed, as well as solar energy. Most of the existing research focused on engine development and thermodynamic performance prediction based on conventional air-standard crankshaft engine configuration. Very few studies have investigated RJCE in free-piston configuration and the use of alternative working fluid.

Some authors recommended notable improvements for enhanced engine performance, and they include a reduction in friction losses and intelligent valve timing. However, with advances in control and automation technology, implementing intelligent valve timing operation would provide a solution to valve timing operation, and friction losses could be minimised by adopting free-piston engine technology. The next section of this chapter examines some reported studies on using alternative working fluids in the hydrogen-fuelled engine.

2.4 Noble gas circulation in hydrogen fuelled engines

The LJEG technology development provided an alternative way to use hydrogen fuel, which mimics fuel cells to convert chemical energy into electricity. Hydrogen is considered the most attractive zero-carbon alternative fuel with no Greenhouse Gas (GHG) emissions, and there have been successful hydrogen applications in non-traditional engine technology

[94]. The use of noble gases as a working fluid instead of nitrogen on hydrogen combustion has been investigated by different authors [95] [96] [97] [98]. Replacing nitrogen with noble gas in hydrogen combustion can significantly boost the cycle efficiency due to the higher specific heat ratio of noble gases [99]. It also has the advantage of eliminating the production of oxides of nitrogen (NOx) caused by the absence of nitrogen, shortened the ignition time delay [100], [101] and lead to increased combustion flame temperatures [102] [103]. There seemed to be an agreement on the choice of argon to other noble gases in hydrogen-oxygen-noble gas combustion technology. Shahsavan and Mack [103] analysed the use of hydrogen fuel in constant volume combustion and compared the mixtures of oxygen with nitrogen, argon, and xenon. The results indicated that argon appears to be a better-working fluid for hydrogen combustion. However, both argon and xenon provided higher temperatures and OH mass fractions in comparison to nitrogen. Argon also showed a far better mixing rate of the injected fuel compared to xenon due to higher diffusivity [100] [101] [104]. *Fuel diffusivity* is a vital parameter desired, especially in non-premixed combustion [99], which was obtainable in hydrogen-oxygen-argon combustion [101]. High diffusivity enhanced better fuel and oxidiser mixing in non-premixed combustion [105]. Argon is abundantly available, comparatively easy and inexpensive to obtain as a by-product of cryogenic air separation [106]. Additionally, argon gas facilitates the creation of gas-tight seals [107], and unlike nitrogen, the specific heat ratio of argon does not decrease at high temperatures [61] [109].

The concept of the argon-oxygen mixture in place of air as a working fluid in engine combustion is not new. Laumann and Reynolds first proposed it in 1978 for a closed-loop hydrogen-fuelled internal combustion engine intending to increase the engine's efficiency and eliminate emissions [110]. De Boer and Hulet took Laumann's concept further in 1980. The researchers developed an internal combustion engine test rig with the aim to power space systems, submarines and zero-emissions vehicles [111]. The preliminary investigation results indicated an inherent tendency for efficiency improvement essentially influenced by the use of an argon-oxygen mixture. Additionally, it was challenging to operate the engine at stoichiometric mixtures of hydrogen and oxygen due to knock and a high tendency of self-ignition. In 1982 Ikegami, Miwa and Shioji experimentally tested argon circulation on a compressed ignition hydrogen-oxygen fuelled engine. They concluded that the compression-ignition operation of the hydrogen engine with the argon-oxygen mixture was stable and manageable. The researchers achieved increased indicated thermal efficiencies close to 50% using compression ratios between 10 and 16 and reported an increased cycle temperature and pressures [112].

Researchers from Toyota Motor Corporation [107] investigated the effect of oxygen and argon mixture on a closed-cycle hydrogen-fuelled internal combustion engine. The results showed the efficiency improved from 32% to 41% when the working fluid was switched from air to oxygen-argon mixture, resulting in an efficiency improvement of 28% at a pressure ratio of 6.0. The results suggested that an excess oxygen ratio of at least 1.1 was required to maintain stable and total hydrogen combustion. However, if the excess oxygen ratio increased beyond the necessary level, the efficiency deteriorated.

Similarly, researchers at the University of California [113] experimentally investigated hydrogen-oxygen-argon combustion and hydrogen-air combustion in a single-cylinder variable-compression ratio spark-ignition internal combustion engine. An efficiency improvement of 36% with hydrogen-oxygen-argon mixtures compared with hydrogen-air mixtures at a compression ratio of 6.0 was achieved. It suggested that operating hydrogen-oxygen-argon mixtures at low loads was more effective because the lower compression ratio resulted in a substantially more significant portion of the gas residing in the adiabatic core than in the boundary zone and crevices, thereby leading to less heat transfer and complete combustion.

A research team from Tongji University experimentally compared using air and oxygen-argon mixture in a hydrogen-fuelled spark-ignition internal combustion engine. The results indicated that higher Indicated mean effective pressure (IMEP) and better combustion stability is achieved with oxygen-argon mixture compared with air [114], and the use of oxygen-argon mixture could promote combustion reaction [115].

Researchers from Kyoto University experimentally investigated the combustion characteristics of hydrogen jets in an argon-oxygen atmosphere in a constant volume combustion vessel [116]. The combustion of hydrogen in argon-oxygen mixtures was described to be stable [109]. The authors investigated the effects of injection pressure, ambient pressure and ambient temperature on a direct injection pre-burning system. The results indicated that ignition delay increased as the ambient temperature decreased, jet penetration decreased with increased ambient pressure, and increased with injection pressure [117]. However, under direct hydrogen injection, it is recommended to control the combustion through hydrogen injection rate and ambient conditions [118].

Aznar et al. [108] experimented with hydrogen and methane combustion in air and an argon-oxygen atmosphere in spark-ignition and compression-ignition internal combustion engines. The results indicated that running the engine with an argon-oxygen mixture in spark ignition mode led to improvements in efficiency up to 40% relative to the spark-ignited oxygen-nitrogen mixture. In comparison, an efficiency improvement of 50% is achieved in argon-oxygen mixture compression ignition mode compared to the spark-ignited oxygen-nitrogen mixture. In a similar investigation by the same authors [119], the results indicated that a stable engine operation was achieved under both compression ignition and spark ignition operation modes. An optimal argon-oxygen mixture ratio of 85% argon and 15% oxygen was established; this argon-oxygen mixture ratio achieved an efficiency improvement of 34% relative to air at the same compression ratio for a port injection operation. The direct injection experiments showed that indicated thermal efficiency of 44% was achieved. It corresponds to an efficiency improvement of 50% relative to the air being used as the oxidiser for port fuel injected spark ignition operation at the same compression ratio. The authors suggested future research on a closed-cycle operation by recycling the exhausted argon.

In a similar study by the same research team on the internal combustion engine, Aznar et al. [120] maintained that the use of an argon-oxygen mixture (argon 15% and oxygen 85%) resulted in improved system efficiency, enhanced the heat release rate and generated a higher pressure rise. The results showed a reduction in engine heat losses and an overall increase in the indicated mean effective pressure, despite lesser oxygen content in the working fluid. The observed improved efficiencies were attributed to the higher specific heat ratio of the working fluid and a reduction in the heat losses to the cylinder walls. Less heat loss observed with argon-oxygen mixture could be caused by the lower thermal conductivity of argon relative to the air or could be attributed to the quicker cooling of the working fluid, which decreased the temperature gradient across the cylinder wall during the exhaust stroke. Because of this, the exhaust temperatures for combustion of the argon-oxygen mixture were 100 ^oK to 150 ^oK less than in the case of air.

Li et al. [121] experimentally studied the effects of argon dilution on a multi-point injection spark-ignited, heavy-duty natural gas engine. Argon was added into the intake charge at 50% load. The results indicated that as the percentage of argon increased in the intake charge, the density of air-argon mixture at intake temperature increased, the mixture gas constant decreased, the thermal diffusivity increased, the specific heat ratio increased while the specific heat capacity slightly decreased. The efficiency increased by 3.5% when the percentage of argon in air mixture increased from 0% to 18.6% if the engine cycle was assumed an Otto cycle. The authors concluded that argon dilution was superior to carbon dioxide and nitrogen for efficiency improvement [122].

Moneib et al. [123] investigated the combustion characteristics of a variable compression gasoline engine under an argon-air mixture. The argon concentration varied between 0% and 15%, while oxygen concentration was kept constant at 21% throughout the experiment. The results indicated that increasing the argon concentration resulted in increased engine volumetric efficiency, increased combustion peak temperatures, increased heat release rate, and faster combustion. The brake mean effective pressure (BMEP) and brake power increased with argon concentration. Specific fuel consumption decreased with an increase in argon concentration, and the brake thermal efficiency increased with argon concentration.

The use of argon instead of nitrogen would result in increased ambient density in the combustion chamber due to the difference in molecular weight of nitrogen (molecular weight 14) and argon (molecular weight 40). Increased ambient density might lead to mixing difficulty in the direct injection process when a lighter gas is injected in a denser atmosphere. Deng et al. [124] investigated oxygen direct injection and hydrogen direct injection in an argon atmosphere to achieve a better mixture in a high-pressure constant-volume combustion vessel. The experimental studies were focused on jet entrainment rate and penetration at varying injection pressure. It was found that an increase in injection pressure increased the penetration length of hydrogen and oxygen jets. However, the increasing rate of jet penetration length decreased with the development of gas jets, resulting from the increasing ambient gas entrained in the jet. The increase of ambient pressure led to decreased jet penetration length for both hydrogen and oxygen injection. The entrainment rate of both hydrogen and oxygen jets increased with jet development and injection pressure. It indicated that the ambient gas is continuously entrained with both hydrogen and oxygen jet development as well. The jet entrainment rates for both hydrogen and oxygen increased generally with the ambient pressure. However, the rate of oxygen jet entrainment decreased when the ambient pressure is increased to 1.2 MPa; the reason for decreased oxygen jet entrainment rate is attributed to lower jet penetration. The authors recommended the use of a hydrogen direct injection strategy. The same research team, Deng et al. [125], investigated the effects of argon-oxygen mixtures on natural gas fuelled compressed ignition engine. The test results showed that at 82% argon composition, the engine achieved a peak indicated thermal efficiency of 47.8%, a 33% efficiency improvement compared with air used as the oxidiser. The ignition delay and combustion time become relatively shorter under the argon-oxygen atmosphere.

A research team from Shanghai Jiao Tong University [126] numerically investigated the effects of argon, nitrogen, nitrogen-carbon dioxide mixture and carbon dioxide atmosphere on the exergy losses of premixed hydrogen flames. The losses were categorised into exergy loss through incomplete combustion, chemical reaction, heat conduction and mass diffusion. Among the four categories, chemical reactions were the dominant source for exergy loss from entropy generation and then followed by heat conduction, mass diffusion and incomplete combustion. The simulation results indicated that exergy losses through chemical reactions, heat conduction and mass diffusion in the nitrogen atmosphere were greater when compared with the argon atmosphere. In comparison, losses through incomplete combustion were more significant in an argon atmosphere.

2.4.1 Summary

The use of argon-oxygen mixture instead of air in natural gas, methane, gasoline, and hydrogen combustion have been investigated both through experiments and numerical modelling and mainly for application in internal combustion engines. Closed-cycle applications of conventional fuel combustion, i.e. gasoline and methane, in an argon-oxygen mixture, may not be attractive because the need to separate and remove the unwanted combustion products from the closed cycle would be complicated with the technology available. However, hydrogen combustion in an argon-oxygen mixture will produce steam, and steam could be condensed to water and be removed from the cycle without many complexities. Argon-oxy-hydrogen combustion in ICE raised an additional challenge with engine knock resulting from higher combustion temperatures, limiting the operational cycle range. However, engine knocking will not present a challenge in LJEG with argon-oxy-hydrogen combustion, and this is because of its inherent out of cylinder combustion and the ability to regulate the temperature of the external reactor.

Chapter 3: Research methodology

This chapter presents the detailed systematic course of action taken to endeavour to answer the research questions. Therefore, to achieve the research objectives outlined in section 1.2 of the thesis, the following methodology was adopted:

3.1 Prototype testing

Experimental tests were conducted on the proof-of-concept open-cycle LJEG test rig at low temperatures and pressures to understand the operation of the LJEG and generate test data for further engine analysis and simulation model validation. The data collected for interpretation and validation during testing are as follows:

- Piston assembly displacement
- Expander and compressor cylinder pressure
- Time
- Temperature
- Valves opening and closing timing
- Working fluid mass flowrates

The piston velocity, acceleration, pressure and inertia forces on the pistons, engine indicated work and indicated efficiency were calculated from the experimental results for further investigations. Testing operation and data acquisition and processing were reported in Chapter 4 of the thesis.

3.2 Friction force analysis

In order to understand the dynamics of the LJEG, a detailed analysis of the LJEG dry friction characterisation was conducted. The behaviour of various system variables on friction properties was identified. As a result, a novel friction model for an LJEG was developed. Calibration of the dry friction numeric model was conducted, and the model was validated against test data from the test rig.

Some of the variables that determined the friction of an LJEG include:

- Piston ring force
- System pressure
- Piston sliding velocity
- Piston Acceleration
- The nature of the piston-cylinder liner interface

3.3 Full cycle modelling

A complete numerical model, which includes the dynamic model coupled with the engine friction model, thermodynamic and combustion model of a semi-closed loop argon-oxy-hydrogen combustion LJEG was developed. The dynamic and thermodynamic models were developed in Matlab/Simulink. The combustion model was developed in Matlab/Simulink/Thermolib. The dynamic and thermodynamic models and the combustion model were validated independently with test data before the separate models were coupled into a full-cycle model. The full-cycle model was used to describe the behaviour and performance of both the air-standard open-cycle LJEG and the semi-closed cycle LJEG and identify the factors that influenced the engine operations and the linear machine electricity generation. The coupled model considered the following:

- Forces acting on the main components of the engine
- Friction acting on the engine
- Heat transfer loss from the cylinder to the ambient
- Load of the generator
- Operating pressure cycle
- Mass flow through the individual valves
- Different valve timing operations
- Compression and expansion processes
- Combustion processes and operation temperature
- Heat addition and removal processes
- Design parameters of the linear electric machine
- Geometric size ratios of the expander and compressor

The model was used to investigate the following:

- Engine performance; including cycle pressures, temperatures, and fluid flow rates
- Engine output; including indicated work, indicted power, and electric power
- Piston dynamics; including piston displacement, velocity, acceleration and friction
- Fuel efficiency, electrical efficiency
- Optimal working conditions; including valve timing, fuel input, temperature, electric load force, power density etc.

3.4 System analysis

An investigation of the operational performance and a parametric analysis of the LJEG with the coupled model was undertaken. The performance and stability response of the LJEG resulting from changes in the operational and geometric variables were studied to identify the optimal operating conditions and valve control strategies. The main variables analysed include:

- The ratio of expander and compressor diameter
- The expander inlet and outlet valve timing
- The system cycle pressure
- Generator load
- Operation temperature

As the reactor of the LJEG operates intermittently, the technical feasibility of coupling multiple LJEG with a single reactor was investigated at various expander intake and exhaust valve timing to further optimise the system.

Chapter 4: The LJEG

4.1 Engine description

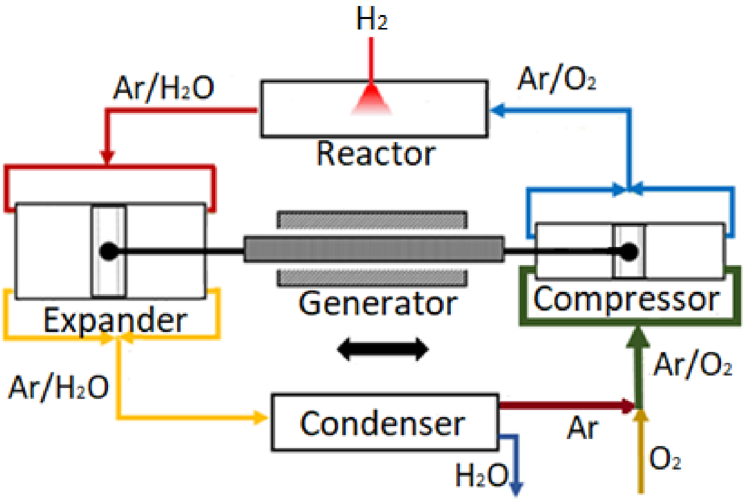

Figure 4-1. Schematic configuration of the proposed semi-closed cycle Linear Joule-cycle Engine Generator with Argon-Hydrogen Reactor.

The schematic configuration of the proposed semi-closed cycle Linear Joule-cycle Engine Generator with Argon-Hydrogen reactor LJEG is presented in Figure 4-1. The main components of the semi-closed-loop LJEG include a linear expander, a linear compressor, a linear alternator, a condenser and an external combustion chamber. A double-acting free piston is placed in the expander cylinder (left side) and the compressor cylinder (right side), respectively. The left and right pistons and cylinders are arranged in direct opposites. A rigid connecting rod connected the two opposite cylinder chambers (piston and cylinder) without sideways pressure on the piston, and the linear alternator is installed on the piston connecting rod. The intake and exhaust valves are located on the ends of the expander and the compressor to draw in and expel the working fluid. The thermodynamic cycle commenced from the compressor, where the working fluid is compressed before this compressed working fluid is fed into the external reactor. Hydrogen is supplied to the reactor, and it is combusted with oxygen. The energy of the working fluid is raised at constant pressure in the reactor. The working fluid with elevated temperature and pressure from the reactor is injected into the expander to produce expansion work in the expander. The expansion work is used to drive the compressor for pressure build-up and the linear generator for electricity.

Gaseous argon is the selected primary working fluid, and oxygen is fed into the argon line connected to the compressor inlet valve. The hydrogen supplied to the reactor would react with oxygen in the compressed argon/oxygen mixture to produce heat and water vapour. The temperature of the products of the combustion post-expansion is cooled in the condenser, and liquid water is removed from the closed system leaving pure argon to loop back into the cycle.

The theoretical thermodynamic cycle of a semi-closed cycle LJEG is shown in Figure 4-2, and this consisted of four processes. A-B represents the adiabatic and reversible compression of the argon/oxygen mixture in the compressor. B-C represents the constant pressure fuel combustion idealised as constant pressure heat addition when hydrogen is mixed with the pressurised argon/oxygen mixture combustion at constant pressure occurs in the reactor. C-D represents the reversible and adiabatic expansion when high-temperature and high-pressure gases enter two separate expander chambers and expand in the chambers alternatively. This expansion pushes the piston resulting in linear back and forth motion. The mechanical power from the linear motion partly drove the compressor piston for the compression process. The remaining power was the output to drive the linear generator for electricity generation. D-A represents the constant pressure heat rejection process. This involves the constant pressure ejection of heat to the environment through the condenser. Alongside this, water is discharged from the cycle, leaving only pure argon for the next cycle.

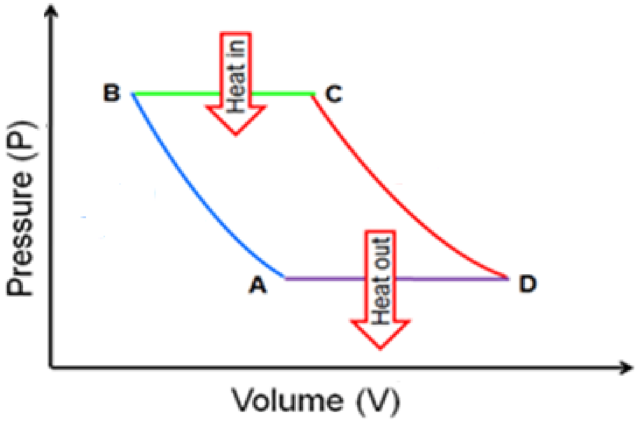

Figure 4-2. Linear Joule Cycle P-V diagram.

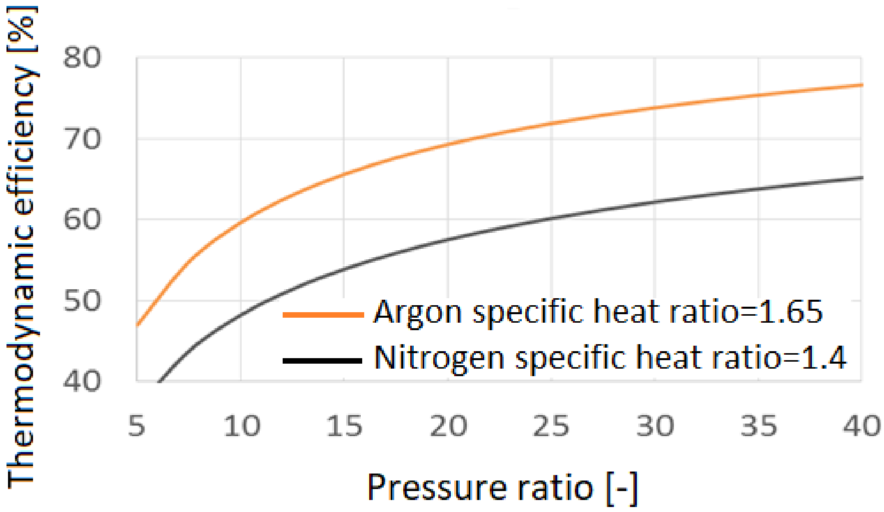

Figure 4-3. Linear Joule Cycle ideal thermodynamic efficiency as a function of pressure ratio and primary working fluid.

One of the benefits of exploiting the properties of argon as an inert working fluid is clearly shown in the relationship between the ideal thermodynamic efficiency of the Joule cycle over a range of pressure ratios as presented in Figure 4-3. The use of argon as the primary working fluid increased the efficiency of the cycle relative to nitrogen in the order of 25%, and this is because of the relative differences between the specific heat ratio of argon (γ=1.65) and nitrogen (γ=1.4). Detailed logic behind the choice of argon as the primary working fluid are presented in subsequent chapters.

4.2 Testing rig description and data acquisition

The schematic configuration of the open-cycle air-standard LJEG is illustrated in Figure 4-4. The picture of the first-generation prototype test rig of the LJEG developed at Newcastle University, as well as its Solidworks image, are shown in Figure 4-5. The first generation LJEG prototype was operated as an air-standard open-cycle engine and had no condenser nor oxy-hydrogen-argon reactor. Instead, an electric heater was substituted for the oxy-hydrogen-argon reactor and air was used as the working fluid during testing. The pressure and temperature of the working fluid at testing were lower than the proposed pressure of 7 bar and temperature of 1100 K for the engine. Moving mass plates were attached to the connecting rod to act as the translator of the linear alternator, and as such, it had no alternator attached. The arrangement of the pistons and cylinders as well as the other operations were identical with the descriptions stated in section 4.1 Engine description. The first-generation prototype main specifications are shown in Table 4-1.

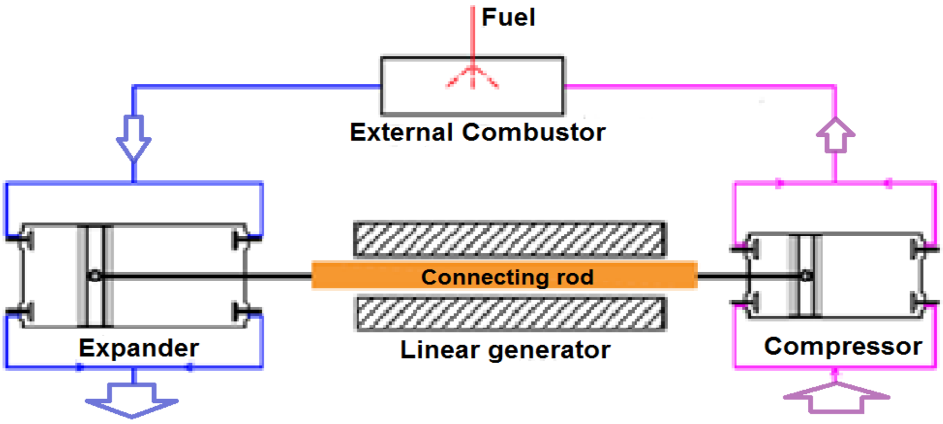

Figure 4-4. Schematic configuration of the open-loop air-standard Linear Joule-cycle Engine.

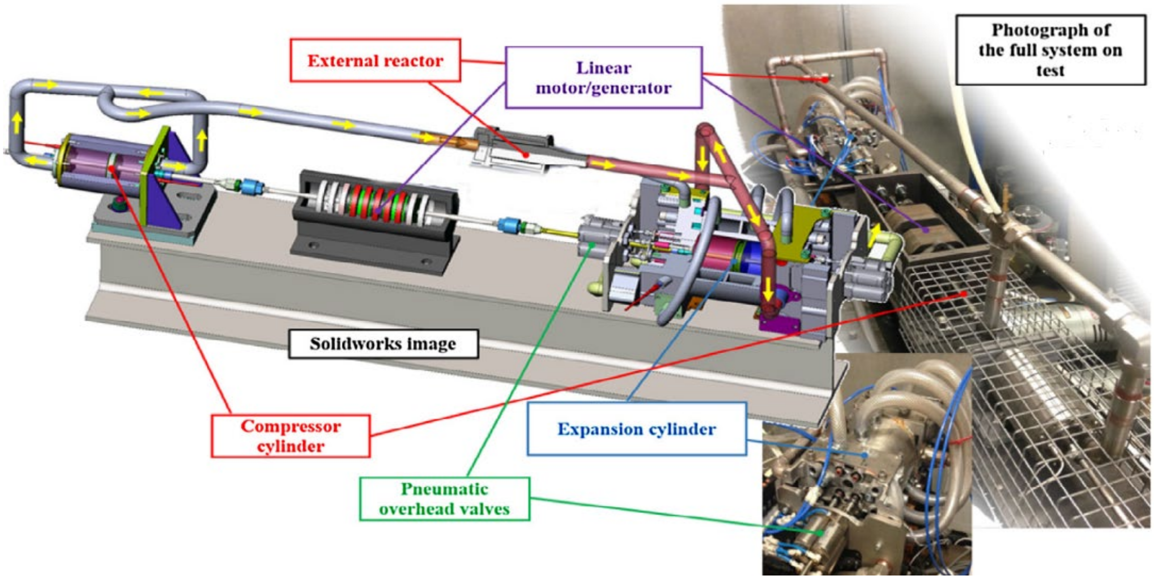

Figure 4-5. First-generation prototype of the Linear Joule Engine Generator at Newcastle University.

Table 4-1 First generation prototype specifications.

	Parameters [Unit]	Value
System	Piston assembly mass [kg]	8.5
Expander	Maximum stroke [mm]	120.0
	Effective bore [mm]	80.0
	Inlet pressure [bar]	2.0 – 2.8
	Inlet temperature [K]	300 - 473
	Valve diameter (inlet x 2) [mm]	25.61
	Valve diameter (exhaust x 2) [mm]	23.37
	Valve lift [mm]	8.13
Compressor	Maximum stroke [mm]	120.0
	Effective bore [mm]	70.0
	Inlet pressure [bar]	1.0
	Outlet pressure [bar]	2.2 – 2.7
	Valve diameter (inlet x 2) [mm]	3 off 6.75 mm holes and 3 off 3 mm holes
	Valve diameter (exhaust x 2) [mm]	25
	Valve lift [mm]	4.5
Linear generator	Moving mass plates [kg]	0 - 20

The temperature of the compressed air (working fluid) supplied by an external compressed air tank (not shown in Figure 4-5) was raised in the reactor by an electric heater during the starting operation and subsequently supplied to the expander. The high temperature compressed air underwent an expansion in the expander and, as a result, drove the compressor. The compressed air tank continued to provide the compressed air until engine stability was achieved. Once the engine was stable, the compressed air tank was switched off, and the compressor line of the engine supplied the compressed working fluid through the reactor to the expanders. Compression and expansion occurred concurrently in the compressor and expander and alternated between the left and right sections of the double-acting piston chamber for both the compressor and the expander. These simultaneous and alternating processes in the expanders and compressors provided the oscillatory motion of the piston assembly.

The expander inlet valve opened when the expander piston reached its Operation Top Dead Centre (OTDC) and closed at a time determined by other variables. The expander exhaust valve opened when the expander piston reached its Operation Bottom Dead Centre (OBDC) and closed at OTDC or earlier if expander recompression was needed. The compressor inlet valve opened when the compressor piston reached OTDC and closed when the compressor piston reached OBDC. The compressor outlet valve opened when a predetermined pressure was achieved and closed at OTDC. A linear actuated valve control system controlled the inlet and exhaust valves of both the compressor and the expander.

The expander intake and exhaust valves were of poppet valve type with adjustable lift, and the compressor intake and outlet valves were of flap valve type with adjustable lift. An electro-pneumatic system based on a Festo actuator was used to control the opening and closing timing of the intake and exhaust valves. The flow rates were measured using an Aalborg thermal mass flow meter, AVL piezoelectric transducer sensors measured the pressures, and the air temperatures were measured with type K thermocouples. The piston positions were measured using variable inductor displacement sensors and a linear encoder attached to the connecting rod of the piston assembly.

The structure for data acquisition and control processes are shown in Figure 4-6. These processes were implemented using the National Instrument CompactRIO system. The algorithm for control, monitoring, and display of the real-time signals were developed in LabVIEW. Screenshots of the developed program for data acquisition/display and system control in LabVIEW is displayed in Figure 4-7. The actuators and sensors were all connected to input/output (I/O) modules on the CompactRIO system for data collection. The data were collected through the I/O modules and temporarily stored in the CompactRIO memory, then streamed to the host computer. The measured piston displacement, compressors' and expanders' pressure, the temperatures of the reactor, compressor and expander, and the working fluid flowrates were all used as feedback signals to control the intake and exhaust valve timings. Data interpretation were carried out using a MATLAB script written to read the measured data and scale the measured quantity to basic engineering units. During a series of engine tests, data were collected for over 20 to 40 consecutive sequential cycles and post-processed. Data post-processing was performed with MATLAB scripts. The average cycle values of each measured set of data were used when the percentage of deviation between the mean value and any value is less than 5%.

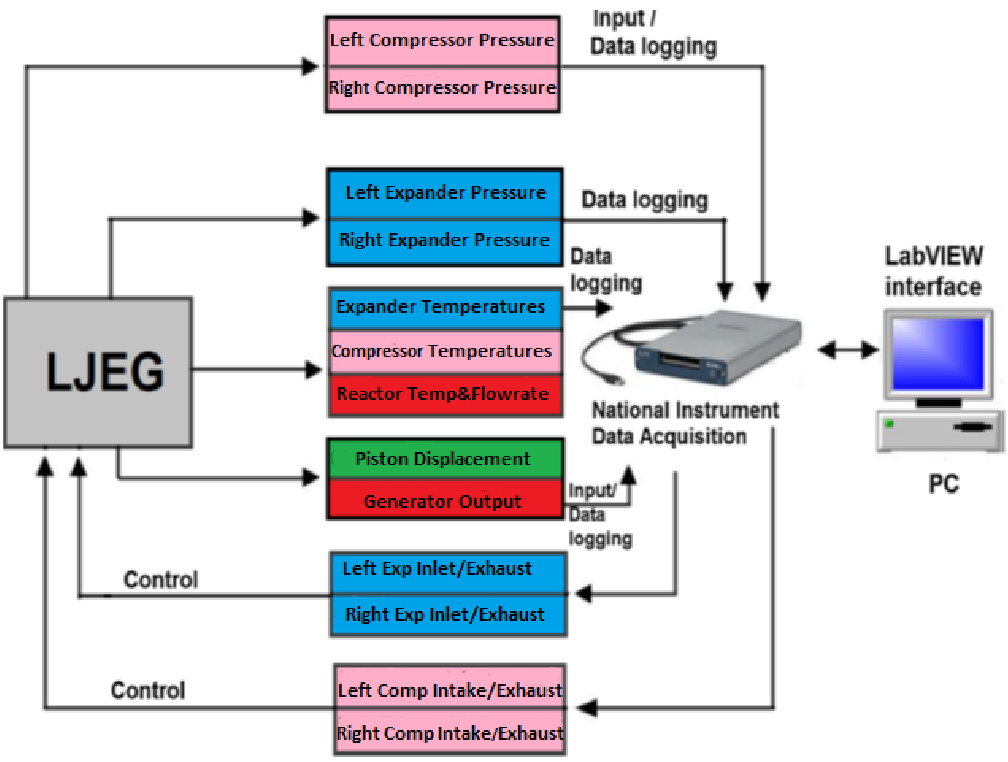

Figure 4-6. Prototype data acquisition and control system configuration.

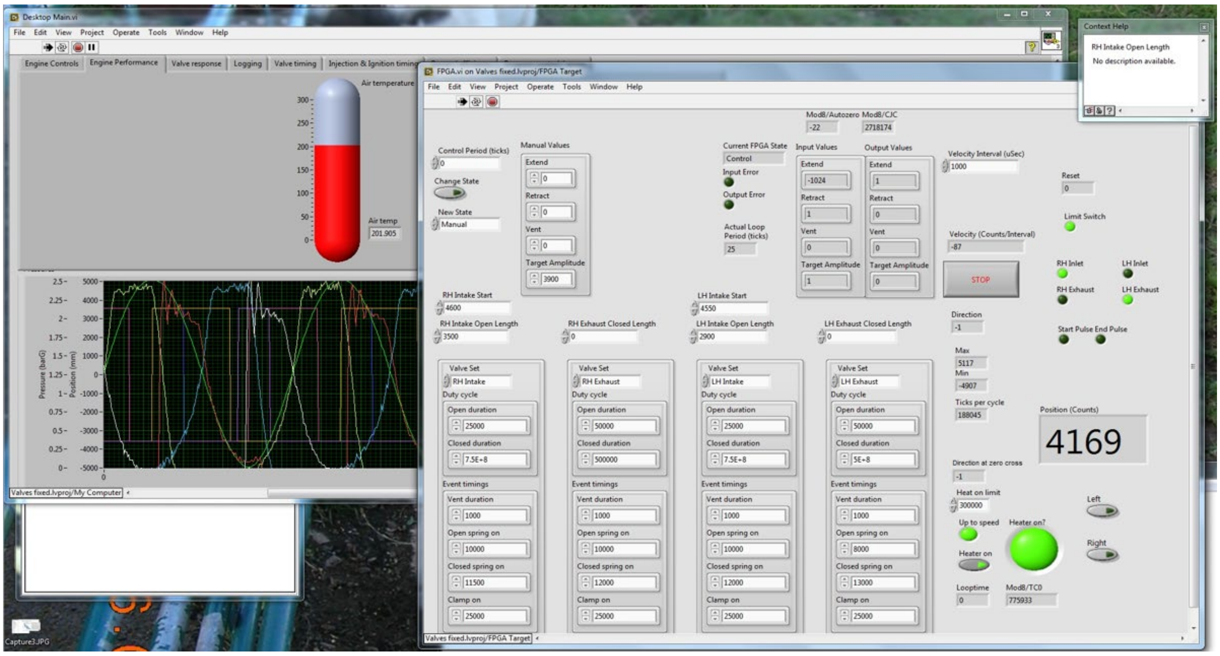

Air temp 201.905

Context Help: RH Intake Open Length. No description available.

Mod8/Autozero -22
Mod8/CJC 2718174
Control Period (ticks) 0
Change State
New State Manual
Manual Values: Extend 0; Retract 0; Vent 0; Target Amplitude 3900
Current FPGA State Control
Input Error
Output Error
Actual Loop Period (ticks) 25
Input Values: Extend -1024; Retract 1; Vent 0; Target Amplitude 1
Output Values: Extend 1; Retract 0; Vent 0; Target Amplitude 0
Velocity Interval (uSec) 1000
Velocity (Counts/Interval) -87
Reset 0
Limit Switch
RH Inlet
LH Inlet
RH Exhaust
LH Exhaust
Start Pulse End Pulse
RH Intake Start 4600
RH Intake Open Length 3500
RH Exhaust Closed Length 0
LH Intake Start 4550
LH Intake Open Length 2900
LH Exhaust Closed Length 0
Direction -1
Max 5117
Min -4907
Ticks per cycle 188045
Position (Counts) 4169
Direction at zero cross -1
Heat on limit 300000
Up to speed
Heater on?
Heater on
Left
Right
Looptime 0
Mod8/TC0 775933

Valve Set	RH Intake	RH Exhaust	LH Intake	LH Exhaust
Duty cycle: Open duration	25000	50000	25000	50000
Closed duration	7.5E+8	500000	7.5E+8	5E+8
Event timings: Vent duration	1000	1000	1000	1000
Open spring on	10000	10000	10000	8000
Closed spring on	11500	12000	12000	13000
Clamp on	25000	25000	25000	25000

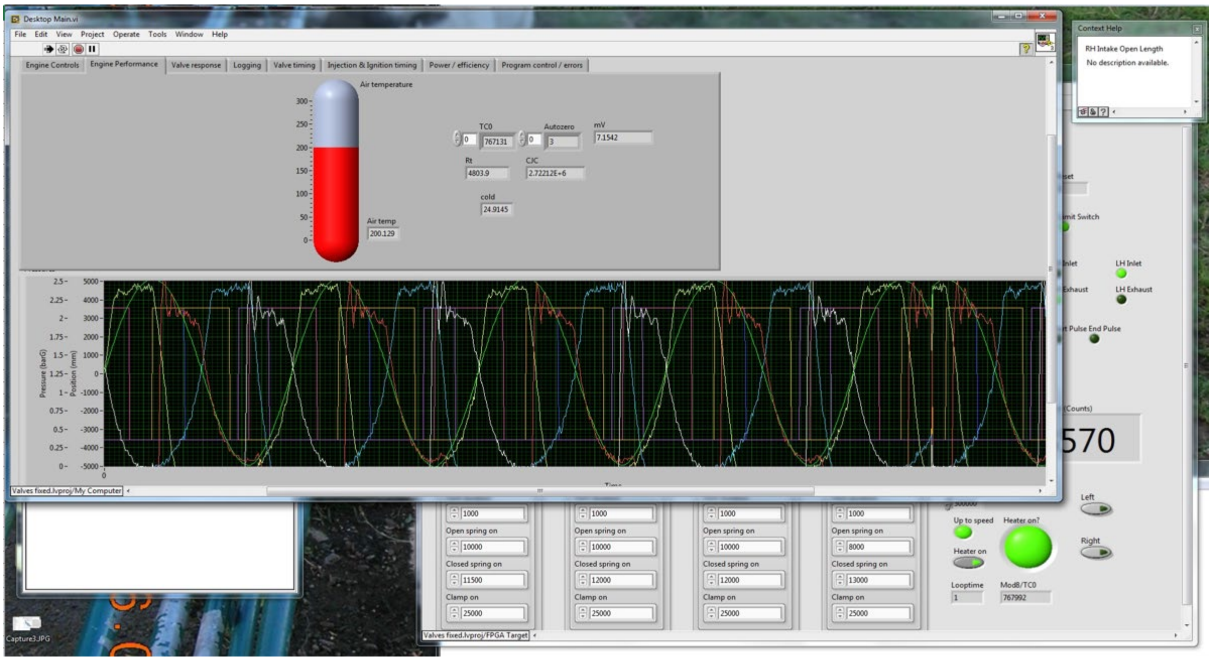

Air temp 200.129

TC0 0 767131
Autozero 0 3
mV 7.1542
Rt 4803.9
CJC 2.72212E+6
cold 24.9145

Context Help: RH Intake Open Length. No description available.

Looptime 1
Mod8/TC0 767992

Figure 4-7. Data acquisition and control panel for the developed program in LabVIEW.

4.3 Conclusions

This chapter highlights the justification for conducting this research and presented the general description and working principles of the open cycle air-standard Linear Joule-cycle Engine Generator and the proposed semi-closed cycle Linear Joule-cycle Engine Generator with Argon-Hydrogen combustion. Detailed LJEG first-generation prototype (open cycle air-standard Linear Joule-cycle) testing and data acquisition were presented. The various data generated from testing were processed and are utilised in the subsequent Chapters in the thesis.

Chapter 5: Modelling of the LJEG

5.1 Model structure

The objectives of the numerical model were to describe the behaviour of the LJEG system; these included but were not limited to the combustion process, the frictional forces, the moving mass assembly dynamics, the changing trend in pressure evolution in the expander and the compressor, the system energy input, power output and the system efficiency. The models were developed on the principles and assumptions of a single zone zero-dimensional thermo-fluid dynamics sub-models, routinely applied in thermodynamic systems, including free piston and traditional internal combustion engine research community [127] [128].

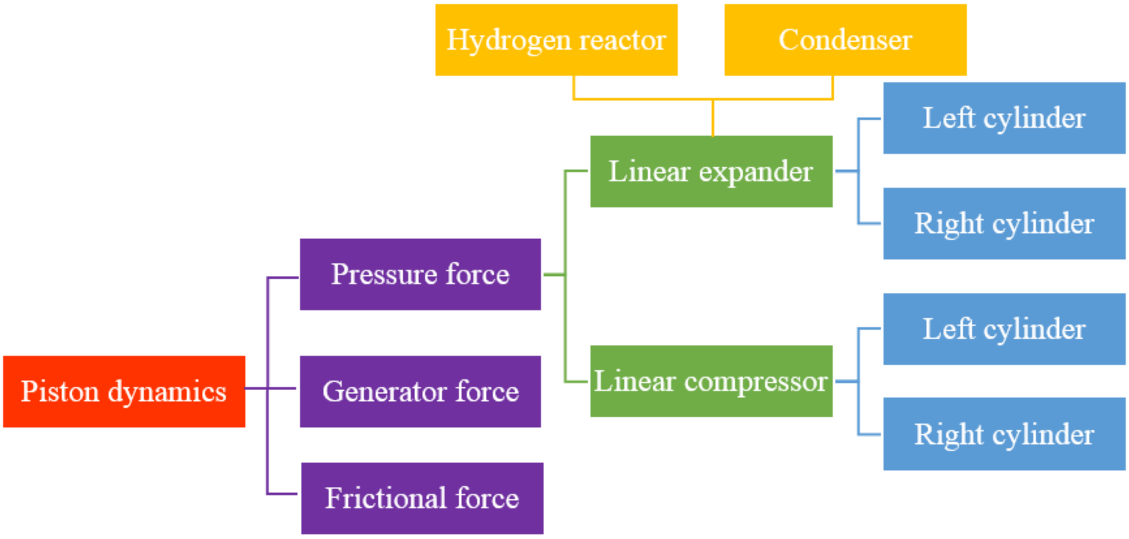

Figure 5-1. Structure of the numerical model use difference representation.

One of the main differences between the LJEG system and the traditional internal combustion engine was the mode of interaction of the pistons with the pressure forces from the cylinder. In the proposed system, the piston was more like a crosshead piston with no side forces on its skirt, and no mechanical system restricted its movement. The forces acting on the pistons, which are the gas pressure forces from the linear expander and the compressor, the resistance force from the linear generator, the frictional forces, and the inertia of the moving mass, determined the moving mass dynamics. The structure of the numerical model is illustrated in Figure 5-1. The generator and the frictional forces were resistive and acted against the moving mass assembly motion direction. The hydrogen reactor was the energy input source, while the generator and the condenser could be described as the primary energy output sources. During the gas exchange process, the outputs of the expander were the working fluid temperature, working fluid pressure, and mass flow rate and they were all used as the input parameters for the condenser. While the hydrogen reactor outputs were: the working fluid temperature, working fluid pressure, and mass flow rate and were all used as input parameters to the expander during the gas intake process.

5.2 Moving mass assembly dynamic model

As the forces acting on the moving mass (piston) assembly include the gas pressure forces from the linear compressor and expander, the frictional force, the resistance force from the linear generator, and the moving mass assembly inertia [129], [130], [131] and [132], these forces determined the piston assembly dynamics. These forces could be expressed according to Newton's Second Law as follows:

$$\overrightarrow{F_e} + \overrightarrow{F_c} + \overrightarrow{F_g} + \overrightarrow{F_f} = m\ddot{x} \tag{5-1}$$

$$\overrightarrow{F_e} = \overrightarrow{F_{el}} + \overrightarrow{F_{er}} \tag{5-2}$$

$$\overrightarrow{F_c} = \overrightarrow{F_{cl}} + \overrightarrow{F_{cr}} \tag{5-3}$$

Where $\overrightarrow{F_e}$ (N) represents the resultant gas pressure force from the linear expander; $\overrightarrow{F_{er}}$ (N) represents the pressure force from the right chamber of the linear expander; $\overrightarrow{F_{el}}$ (N) represents the gas pressure force from the left chamber of the linear expander. $\overrightarrow{F_c}$ (N) represents the resultant gas pressure force from the linear compressor; $\overrightarrow{F_{cr}}$ (N) represents the gas pressure force from the right chamber of the compressor; $\overrightarrow{F_{cl}}$ (N) represents the gas pressure force from the left chamber of the linear compressor. $\overrightarrow{F_f}$ (N) denotes the friction force, $\overrightarrow{F_g}$ (N) denotes the generator force, $\ddot{x}$ (m/s^2) represents piston assembly acceleration, m (kg) is the piston assembly mass. The gas pressure forces from both chambers of the linear compressor and expander were calculated using the in-cylinder pressure and cross-section areas of the piston, as shown in Equations 5-4 to 5-7.

$$\overrightarrow{F_{el}} = p_{\mathrm{el}} \cdot A_e \qquad 5\text{-}4$$

$$\overrightarrow{F_{er}} = p_{\mathrm{er}} \cdot A_e \qquad 5\text{-}5$$

$$\overrightarrow{F_{cl}} = p_{\mathrm{cl}} \cdot A_c \qquad 5\text{-}6$$

$$\overrightarrow{F_{cr}} = p_{\mathrm{cr}} \cdot A_c \qquad 5\text{-}7$$

Where p_{er} (Pa) and p_{el} (Pa) represent the in-cylinder pressure in the right and the left chamber of the expander, respectively. p_{cr} (Pa) and p_{cl} (Pa) represent the in-cylinder pressure in the right and the left chamber of the compressor, respectively. A_c (m^2) and A_e (m^2) represent the piston cross-section area of the compressor and the expander, respectively.

5.3 Combustion model

The compressed argon and oxygen mixture were fed into the combustion reactor, where hydrogen is injected into the reactor to react with the oxygen to produce heat and steam. The hydrogen combustion sub-model computed the outgoing flow after one reaction, and the heat exchange with the surrounding environment was determined. The general combustion equation for hydrogen and oxygen is represented in Equation 5-8 as:

$$2\mathrm{H_2} + \mathrm{O_2} \rightarrow 2\mathrm{H_2O} \qquad 5\text{-}9$$

The first law of thermodynamics for a chemical reaction is expressed as [133]:

$$\sum_{Re} \dot{m}_{in} h_{in} = \sum_{Pd} \dot{m}_{out} h_{out} + \dot{Q}_{add} \quad 5\text{-}10$$

$$\dot{Q}_{add} = \dot{Q}_{rx} - \dot{Q}_{ht} \quad 5\text{-}11$$

$$h_{in} = c_{pin} \cdot T_{in} \quad 5\text{-}12$$

$$h_{out} = c_{pout} \cdot T_{out} \quad 5\text{-}13$$

$$\dot{Q}_{ht} = \alpha A_{re}(T_{re} - T_0) \quad 5\text{-}14$$

Where $\dot{m}_{in}$ (kg/s) is the mass flow into the reactor; h_{in} (J/kg) is the specific enthalpy of the intake gases to the reactor; $\dot{m}_{out}$ (kg/s) is the mass flow rate out of the reactor; h_{out} (J/kg) is the specific enthalpy of the exhaust gases from the reactor. c_{pin} (J/kg·K) is the specific heat capacity at constant pressure for the intake fluids; c_{pout} (J/kg·K) is the specific heat capacity at constant pressure for the exhaust gases from the reactor. T_{in} (K) is the temperature of the intake mass flow into the reactor; T_{out} (K) is the temperature of the exhaust mass flow out of the reactor. $\dot{Q}_{add}$ (J/s) is the heat addition; $\dot{Q}_{rx}$ (J/s) is the heat of reaction; $\dot{Q}_{ht}$ (J/s) is the heat transfer from the reactor to the environment; $\dot{m}_f$ (kg/s) is the mass flow rate of the hydrogen injected to the reactor. α (W/K·m^2) is the coefficient of the heat transfer model; A_{re} (m^2) is the surface area of the reactor; T_{re} (K) is the temperature in the reactor and T_0 (K) is the temperature of the environment.

5.4 Condenser

The two main factors considered in the mathematical model of the condenser were the heat transfer performance and the pressure drop across the condenser. The heat transfer rate for steam/water and argon flowing through a condenser was given by [134]:

$$\dot{Q} = \dot{m}_s(h_s - h_{cw}) + \dot{m}_a(h_a - h_{ac}) \quad 5\text{-}15$$

where, $\dot{Q}$ is the condenser heat duty [kJ/s], $\dot{m}_s$ is the content of steam flowing into the condenser (kg/s). h_s is the enthalpy of saturated steam flowing into the condenser (J/kg), h_{cw} is the enthalpy of water flowing out of the condenser (J/kg), $\dot{m}_a$ is the argon content flowing into the condenser (kg/s), h is the enthalpy of argon flowing into the condenser (J/kg), h_{ac} is the enthalpy of argon flowing out of the condenser (J/kg). However, the heat transfer rate is approximated by [135]:

$$\dot{Q} = UA\Delta T_{lm} \qquad 5\text{-}16$$

where U is the overall heat transfer coefficient $(W/(m^2K))$, A is the total heat transfer area (m^2) and ΔT_{lm} is the logarithmic mean temperature difference (K) [135].

$$\Delta T_{lm} = \frac{T_{cfo} - T_{cfi}}{ln\left(\frac{T_c - T_{cfi}}{T_c - T_{cfo}}\right)} \qquad 5\text{-}17$$

Where T_{cfo} is the outlet temperature of the cooling fluid (K), T_{cfi} is the inlet temperature of the cooling fluid (K) and T_c is the average outlet temperature of the fluid flowing out of the condenser (K).

The energy balance of the cooling fluid yielded [135]:

$$\dot{Q} - \dot{Q}_{cf} = UA\Delta T_{lm} - \dot{m}_{cf}C_p\left(T_{cfo} - T_{cfi}\right) = 0 \qquad 5\text{-}18$$

where C_p is the cooling fluid heat capacity (J/(kg K)), $\dot{Q}$ is the condenser heat duty (J/s), $\dot{Q}_{cf}$ is the cooling fluid heat absorption quantity (J/s) and $\dot{m}_{cf}$ is the cooling fluid flow rate (kg/s).

Fluids flow when a pressure gradient exists. However, fluid transfers in pipes always incur friction in opposition to the flow, resulting in a fluid pressure loss [136]. In order to provide the pressure gradient and overcome any resistance to the flow caused by friction, additional power was required. This additional power required to achieve a given flow rate is expressed as [136]:

$$P = \dot{V}\Delta P \quad \text{5-19}$$

where P is the power (W), $\dot{V}$ is the flow rate (m^3/s) and ΔP is the pressure drop (N/m^2).

For most applications, the volumetric flow rate is known, but the pressure loss is a variable, and its value would be a function of the heat exchanger design. For a fully developed flow in a pipe of length, *L* the pressure loss is given by [136]:

$$\Delta P = 4C_f \frac{L}{D_H}\frac{\rho u_m^2}{2} \quad \text{5-20}$$

$$D_H = \frac{4A}{P} \quad \text{5-21}$$

where, C_f is the Fanning friction factor, *L* is the length of the passageway (m), u_m is the mean flow velocity (m/s), D_H is the hydraulic diameter of the cross-section, *A* is the cross-sectional area (m^2), *P* is the wetted perimeter (m) and ρ is the density of the fluid (kg/m^3).

5.5 Linear expander

The thermodynamic processes in the linear expander chamber include gas expansion and compression processes due to the piston assembly movement, heat transfer between the in-cylinder gas and the cylinder wall, and the exhaust and inlet gas exchange processes. It was assumed that the in-cylinder charge intensive properties were homogenous; these include the pressure, temperature, concentration, density, specific heat capacities, specific internal energy, specific volume etc. The in-cylinder charge potential energy and kinetic and are neglected and follow the ideal gas principle. By implementing the first law of thermodynamics on the in-cylinder charge in the chamber, applying ideal gas laws, specific heats derivatives and internal energy equations, the pressure calculation equation for one of the expander chambers was expressed as [137] [22]:

$$\frac{dp_e}{dt} = \frac{\gamma - 1}{V_e}\left(-\frac{dQ_{htw}}{dt}\right) - \frac{p_e \gamma}{V_e}\frac{dV_e}{dt} + \frac{\gamma - 1}{V_e}\sum_i \dot{m}_e \, h_e \tag{5-22}$$

The heat transfer between the in-cylinder gas and the chamber walls of the expander is modelled according to [138].

$$\dot{Q}_{htw} = hA_e(T - T_w) \tag{5-23}$$

Where $\dot{Q}_{ht}w$ (J/s) is the heat transfer rate; h (W/m^2·K) is the coefficient of heat transfer; A_e (m^2) is the area of the surface in contact with the gas in the expander; T_w (K) is the average surface temperature of the cylinder wall. The heat transfer coefficient is given by [138]:

$$h = 130V^{-0.06}\left(\frac{p(t)}{10^5}\right)^{0.8} T^{-0.4}(\dot{x}_m + 1.4)^{0.8} \tag{5-24}$$

Where V(m3) represents the instantaneous cylinder volume, $\dot{x}_m$ (m/s) is the average piston speed. The mass flow rate through the valves, $\dot{m}_e$ (kg/s) was assumed to be represented by compressible flow through a flow restriction [139].

$$\dot{m}_e = \begin{cases} \dfrac{C_d A_d p_u}{(RT_u)^{\frac{1}{2}}}\left(\dfrac{p_d}{p_u}\right)^{\frac{1}{\gamma}}\sqrt{\dfrac{2\gamma}{\gamma - 1}\left[1 - \left(\dfrac{p_d}{p_u}\right)^{\frac{(\gamma-1)}{\gamma}}\right]}, & p_d/p_u > [2/(\gamma + 1)]^{\gamma/(\gamma-1)} \\ \dfrac{C_d A_d p_u}{(RT_u)^{1/2}}\gamma^{1/2}\left(\dfrac{2}{\gamma + 1}\right)^{(\gamma+1)/2(\gamma-1)}, & p_d/p_u \leq [2/(\gamma + 1)]^{\gamma/(\gamma-1)} \end{cases} \tag{5-25}$$

Where $\dot{m}_e$ (kg/s) is the mass flow rate through a valve; C_d is the discharge coefficient; A_d (m^2) is the reference area of the flow; T_u (K) is the temperature of the inlet gas; p_u (Pa) is the pressure of the upstream of the flow restriction; p_d (Pa) represents the downstream air pressure; R (J/kgK) is the gas constant.

The valve curtain area was used to calculate the reference area of the valve [139]:

$$A_d = \pi D_v L_v \tag{5-26}$$

Where D_v is the diameter of the valve (m); L_v is the valve lift (m).

5.6 Linear compressor

The thermodynamic processes occurring in the compressor chamber include gas expansion and compression processes due to the piston assembly movement and the exhaust and inlet gas exchange processes. The compression and expansion processes were regarded: as adiabatic, the gas is homogenous, and the kinetic and potential energy of the gas were neglected. Implementing the conservation of energy principle and ideal gas laws, specific heats derivatives, and internal energy equations inside a controlled volume produced the pressure calculation equation for the compressor [15], as represented in Equation 5-27. The same gas mass flowrate model (see Equation 5-26) used in the expander was equally applied to the compressor.

$$\frac{dp_c}{dt} = \gamma\left(\frac{p_{i/o}}{V_c\,\rho_{i/o}}\dot{m}_c - \frac{p_c}{V_c}\frac{dV_c}{dt}\right) = \gamma\left(\frac{p_{i/o}}{V_c\,\rho_{i/o}}\dot{m}_c - \frac{\dot{x}p_c}{x}\right) \tag{5-27}$$

Where γ; the specific heat ratio, p_c (Pa) represents the pressure in the compressor cylinder, $p_{i/o}$ (Pa) represents the suction or discharge compressor gas pressure, $\rho_{i/o}$ $(\mathrm{kg/m^3})$ represents the suction or discharge compressor gas density, $\dot{m}_c$ $(\mathrm{kg/s})$ suction or discharge compressor gas mass flow rate. V_c (m^3) compressor working volume. x (m) is the piston displacement and $\dot{x}$ $(\mathrm{m/s})$ represents the piston sliding velocity.

Equation (5-27) was used, as it were to determine the compressor in-cylinder pressure at the suction phase. However, at the discharge phase, Equation (5-27) was adapted to Equation (5-28). The density of the working fluid inside the cylinder during the discharge phase was calculated with Equation (5-29).

$$\frac{dp_c}{dt} = -\gamma\left(\frac{p_o}{V_c\,\rho_o}\dot{m}_c + \frac{p_c}{V_c}\frac{dV_c}{dt}\right) \qquad 5\text{-}28$$

$$\rho_o = \frac{m_c}{V_c} = \frac{m_c}{A_c x} \qquad 5\text{-}29$$

Where m_c (kg) represents the mass of in-cylinder working fluid, ρ_o $(\mathrm{kg/m^3})$ represents the discharge working fluid density, V_c (m^3) represents the compressor working volume, A_c (m^2) represents the compressor cross section area and x (m) is the piston assembly displacement.

In the suction and discharge phase, the mass transfer influenced the thermodynamic state of the in-cylinder working fluid. However, both the discharge and suction valves would have been closed in the compression and expansion phases, and there would be zero mass transfer. Therefore, during the compression and expansion phases:

$$\dot{m}_c = 0 \qquad 5\text{-}30$$

Substituting Equation (5-30) in Equation (5-27) or Equation (5-27) resulted in Equation (5-31):

$$\frac{dp_c}{dt} = -\gamma\left(\frac{p_c}{V_c}\frac{dV_c}{dt}\right) \qquad 5\text{-}31$$

The suction, compression, discharge and expansion phase’s sub-models were enabled or disabled based on the piston assembly displacement and nominal compressor pressure ratio using threshold switches and truth table. The piston assembly displacement, pressure and velocity were selected as feedbacks to determine the valve timing.

5.7 Frictional force

A novel mathematical model describing the dry frictional forces of the LJEG was developed and presented in [15]. The detailed mathematical expressions of the friction model are presented in Chapter 7, but the compressed form is reproduced here for reading ease.

$$F_f = F_{fd} + F_{fp} = \text{Dry contact friction} + \text{Pressure friction loading} \qquad 5\text{-}32$$

$$F_{fd} = \begin{cases} F_{fu,}\ sgn(\ddot{x}) > 0 & F_{fu} = Nf_d\left[1 + \dfrac{f_s - f_d}{f_d}\mathrm{g}(\ddot{x})\right] \\ F_{fl,}\ sgn(\ddot{x}) < 0 & F_{fl} = Nf_d\left[1 - \dfrac{f_s - f_d}{f_d}\mathrm{g}(\ddot{x})\right] \end{cases} \qquad 5\text{-}33$$

$$g(\ddot{x}) = exp\left(-\frac{a_1|\dot{x}|}{|\ddot{x}| + a_2}\right) \qquad 5\text{-}34$$

where a_1, a_2 (> 0) are constant parameters, f_s, f_d; static and dynamic friction coefficient respectively, $F_{fu,}$ and F_{fl} represent the friction force relative to the acceleration and retardation phases, respectively. The frictional force due to system pressure loading is represented [15]:

$$F_{fp} = \frac{bP_c}{P_a}e^{\left(\frac{b\dot{x}_m}{1+|\dot{x}|}+\frac{bP_c}{P_a}\right)} \qquad 5\text{-}35$$

$$b = \left(\frac{z_1}{|\ddot{x}_m| + z_2}\right) \qquad 5\text{-}36$$

where P_c is the in-cylinder compressor pressure (bar), P_a atmospheric pressure (bar), $|\dot{x}|$ the absolute piston sliding velocity (m/s), $\dot{x}_m$ the mean piston velocity (m/s), $\ddot{x}_m$ the mean piston acceleration (${}^{m}/_{s^2}$), z_1 and z_2 are friction parameters.

5.8 Linear generator

A linear generator could be an electromagnetic, electrostatic or piezoelectric force device that transformed mechanical energy into electrical energy. However, the linear generator adopted for this study is the electromagnetic type device. The linear electric generator is, in essence, a linear motor. Because the electromechanical energy conversion process was reversible in electromechanical devices, linear motors could be operated as linear electric generators [140] [141]. There have been some investigations on linear generator topologies, such as tubular [142] [143], planer [144], and transverse flux [145]. The tubular machine was shown in [146] [144] to be attractive when considering resistive loading due to its low inductance, and because of the latter, a tubular generator type was proposed for the study.

The linear generator selected for this study is from the available commercial generators, and the manufacturers protected some of its design parameters. Nonetheless, it would have been challenging to calculate the electromagnetic force from known mathematical equations. Therefore, a simplified model available in literature was adopted in Figure 5-2. Figure 5-2 demonstrates an equivalent circuit of the linear generator.

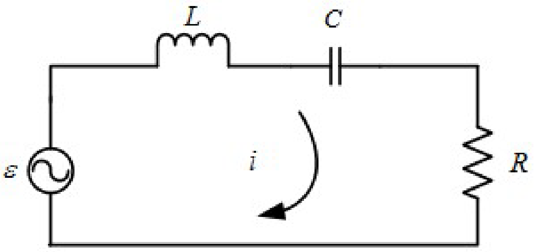

Figure 5-2. Equivalent circuit of the linear electric machine

From Faraday's electromagnetic induction laws, the electromotive voltage ε across the circuit is given as [16], [147]:

$$\varepsilon(t) = -\frac{d\emptyset}{dt} = -K_v\frac{dx}{dt} = -K_v \cdot v \tag{5-37}$$

Where $\emptyset$ is the magnetic flux, v is the synchronous speed assumed to be the same as the mechanical speed, K_v is the electromotive force constant: a generator property and determined by the design parameters of the generator.

The induced current of the equivalent circuit is determined from the voltage across it thus:

$$\varepsilon(t) = (r + R)i(t) + \mathrm{L}\frac{di(t)}{dt} + C\int idt \tag{5-38}$$

Where r is the internal resistance of the coil, and R is the resistance of the external load, i is the current, L is the inductance and C is the capacitance of the circuit. Baker et al. [146] described the inductance of a tubular generator to be low compared to the resistance. It could be considered safe to assume the load circuit is purely resistive, and the capacitance and inductance of the circuit neglected [148]. Then Equation (5-38) can be written as:

$$\varepsilon(t) = (r + R)i(t) \tag{5-39}$$

The current in the circuit is expressed thus:

$$i(t) = -\frac{K_v}{r + R} \cdot v \tag{5-40}$$

The load force of an electric machine was assumed to be proportional to the current of the circuit according to electromagnetic theory and its direction was always opposite of the velocity [149] and [150], the resistance force from the generator was then written as:

$$F_e = -C_e i(t) \tag{5-41}$$

Where C_e $(N/(ms^{-1}))$ was the load constant of the generator and could be determined from the physical parameters of the generator design specifications [16].

The system efficiency calculation is as shown in Equation 5-42 and it with the assumption that hydrogen is the only energy carrier gas among all other gases in the system.

$$\eta = \frac{P}{Q_{fuel}} \times 100\% \tag{5-43}$$

Where η (%) is the system efficiency, P (W) is the generator power output and Q_{fuel} (W) is the input energy provided by fuel.

5.9 Simulation model development

5.9.1 Combustion and fluid model simulation development

The combustor model comprised a reactor, mixers, and pure and mixed substance flow sources using Thermolib [151]. Thermolib is a thermodynamic property library toolbox that calculates fluids' thermodynamic properties based on their composition in MATLAB/Simulink environment. The chemical composition of the fuel and oxidizer mixture was defined in the Thermolib library. Though argon chemical media was not among the generic species in the Thermolib library database; therefore, the thermo-physical properties of argon and the NASA coefficients for calculating thermodynamic and transport properties of argon were added to the Thermolib library database. The NASA polynomials coefficients and the thermo-physical properties for calculating thermodynamic and transport properties of argon are listed in Table 5-1 and Table 5-2, respectively. All the participating species were selected from the Thermolib library database and added to Thermolib Model Setup. In the air-standard cycle simulation, the following species were selected; water (H_2O), carbon monoxide (CO), carbon dioxide (CO_2), Nitrogen (N_2), oxygen (O_2) and hydrogen (H_2), and all the species were allowed in both liquid and gas phases. In the argon cycle simulation, the selected species were as follows; H_2O, O_2, H_2 and Ar, and all the selected species were allowed in both liquid and gas phases. The balancing functionality time from start to stop was 60 seconds and 100 seconds, respectively. Peng Robinson model of gas-phase was used in computing the gas behaviour [152]. The reactor sub-model computed the outgoing flow after one/each reaction by employing the first law of thermodynamics for a chemical reaction. The sub-model also considered the heat exchange with the surrounding environment. The engine control unit (ECU) calculated the quantity of oxygen supplied to the compressor based on the temperature and mass of argon available in the compressor and the target operating temperature in the expander. Similarly, the ECU calculates the quantity of hydrogen injected into the combustor based on the mass of oxygen available in the oxygen-argon mixture from the compressor. Therefore, the content of the working fluid after combustion is argon gas and steam.

5.9.2 Coupled model simulation

The simulation model was developed in Matlab/Simulink coupled with Matlab/Thermolib. While Matlab/Thermolib was used to develop the sub-models of combustion, condenser, and fluid flow, the rest of the sub-models were developed in Matlab/Simulink. The sub-models were controlled using the Stateflow Chart function in Simulink, and the model closed-loop status was achieved by using both initial-conditions blocks and a buffer. All the participating species were selected from the Thermolib library database and added to Thermolib Model Setup. A fixed-step automatic solver was utilised, with a fixed step size of 1 ×10e-6s and the design parameters for the simulation and initial-boundary parameters were set before the simulation. The piston displacement, piston velocity, and combustor fluid outlet temperature were selected as the target outputs to determine the valve timings. The valve timings for opening and closing were adjusted to optimise the scavenging process. The base case for the expander intake valve opening (EIVO) event and the expander exhaust valve opening (EEVO) event was triggered when the piston reaches its TDC and BDC, respectively. The expansion process of the expander was initiated after the EIVO event was triggered.

NASA polynomials used in the combustion model are expressed in Equations (5-44) to (5-46) [153] thus:

$$\frac{C_p}{R} = A + BT + CT^2 + DT^3 + ET^4 \tag{5-44}$$

$$\frac{H}{RT} = A + \frac{BT}{2} + \frac{CT^2}{3} + \frac{DT^3}{4} + \frac{ET^4}{5} + \frac{F}{T} \tag{5-45}$$

$$\frac{S}{R} = AlnT + BT + \frac{CT^2}{2} + \frac{DT^3}{3} + \frac{ET^4}{4} + G \tag{5-46}$$

Where C_p represents the specific heat capacity at constant pressure, R is the gas constant, H is the enthalpy, S is the entropy and T is the temperature. A, B, C, D, E, F and G are the numerical coefficient. In Table 5-1, A, B, C, D, E, F and G represent the component coefficients at high temperature range and A1, B1, C1, D1, E1, F1 and G1 represent the component coefficients at low temperature range. The Antoine equation is expressed [154] as:

$$Log_{10}P = A_a - \frac{B_a}{T + C_a} \tag{5-47}$$

Where P is the vapour pressure, T is temperature and A_a, B_a and C_a are component-specific constants.

Table 5-1. Argon NASA Polynomials Coefficients

NASA coefficient [153]	***Unit*** [153]	**Value** [153]
A-element (high temp. range)	*[-]*	2.5E+00
B-element (high temp. range)	*[K^{-1}]*	0.00E+00
C-element (high temp. range)	*[K^{-2}]*	0.00E+00
D-element (high temp. range)	*[K^{-3}]*	0.00E+00
E-element (high temp. range)	*[K^{-4}]*	0.00E+00
F-element (high temp. range)	*[K]*	-7.45E+02
G-element (high temp. range)	*[-]*	4.37967491E+00
A1-element (low temp range)	*[-]*	2.5E+00
B1-element (low temp range)	*[K^{-1}]*	0.00E+00
C1-element (low temp range)	*[K^{-2}]*	0.00E+00
D1-element (low temp range)	*[K^{-3}]*	0.00E+00
E1-element (low temp range)	*[K^{-4}]*	0.00E+00
F1-element (low temp range)	*[K]*	-745.375E+00
G1-element (low temp range)	*[-]*	4.37967491E+00
Minimum temperature for low temperature NASA polynomials.	*[K]*	200E+00
Limit temperature between NASA high and low ranges.	*[K]*	1000E+00
Maximum temperature for high temperature range.	*[K]*	6000E+00

Table 5-2. Argon Property Media Data

Property	***Unit***	**Value**
Molar Mass	*[kg/kmol]*	39.948E+00
Antoine equation_ A	*[-]*	3.295E+00 [155]
Antoine equation_ B	*[-]*	215.24E+00 [155]
Antoine equation_ C	*[-]*	-22.23E+00 [155]
Reference temperature for density offset calculation	*[K]*	87.3E+00 [156]
Reference temperature for evap. properties	*[K]*	87.3E+00 [156]
Evaporation enthalpy	*[Joule/mole]*	6.44E+03 [133][157]
Evaporation entropy	*[Joule/mole-K]*	154.8E+00 [133]
Critical Temperature	*[K]*	151.15E+00 [155]
Critical Pressure	*[Pa]*	4.88E+06 [155]
Critical Volume	*[m^3/mol]*	7.46E-05 [155]
Acentric Factor	*[-]*	-2.0E-03 [157]
De-Broglie-Wavelength.	*[-]*	9.99E+02 [155]
Critical Real-Factor	*[-]*	2.91E-01 [157]
Linear Molecule	*[-]*	0.00E+00 [155]
Dipole Moment	*[Debye]*	0.00E+00 [157]
Boiling Temperature	*[K]*	8.73E+01 [133]
Inner Rotation	*[-]*	9.99E+02 [156]
Number of C atoms	*[-]*	0.00E+00
Number of H atoms	*[-]*	0.00E+00
Number of O atoms	*[-]*	0.00E+00
Number of N atoms	*[-]*	0.00E+00
Number of F atoms	*[-]*	0.00E+00
Number of Cl atoms	*[-]*	0.00E+00
Number of S atoms	*[-]*	0.00E+00
Number of Ar atoms	*[-]*	1.00E+00
Triple-point temperature	*[K]*	8.38E+01 [157]

5.10 Conclusions

This chapter presented the numerical model development of an open-cycle air-standard LJEG and semi-closed cycle argon-oxy-hydrogen combustion LJEG. The mathematical representations of the expander, compressor, generator, combustor, condenser and frictional force were presented with the necessary assumptions. Model execution was performed in Matlab/Simulink coupled with Matlab/Thermolib. The sub-models' validation and simulation results of the coupled model are presented in the next chapter.

Chapter 6: Numerical model validation and simulation results

6.1 Model validation

The LJEG first-generation prototype test results are presented in this chapter. The results were used for the dynamic and thermodynamic validation of the simulation model developed in Chapter 5 because the second-generation prototype was not ready for testing. The first-generation test rig of the LJEG was an open-cycle system, and therefore air was adopted as the working fluid medium during testing. The prototype configuration was identical with the input parameters used in the simulation, as presented in Table 6-1. The same valve timing settings of the test rig during testing were adopted in the numerical simulation. The heat input operation of the test rig was not simulated in Simulink, but rather its input was a workspace variable in MATLAB. The valve settings operation control in STATEFLOW function was modified to depend on time and piston displacement rather than piston velocity and displacement. The summary of the piston assembly dynamics from the test result is indicated in Table 6-2.

The piston assembly acceleration, velocity and displacement profiles, and the displacement vs velocity profile of the simulation and test are presented in Figure 6-1, Figure 6-2, Figure 6-3 and Figure 6-4, respectively, at the same operating conditions. The right expander and left compressor's in-cylinder pressure are presented Figure 6-5 and Figure 6-6, respectively. The piston assembly dynamics and the developed pressure trend predicted from the numerical simulation showed similar trends to those of the test data, e.g. similar frequency and the observed amplitudes were almost identical. The observed differences could be considered acceptable due to the simplifications and assumptions made when linearising the model. The model is considered robust to evaluate the system performance of the prototype.

Table 6-1. Prototype specifications and simulation input parameters.

	Parameters [Unit]	Value
System	Piston moving mass [kg]	8.0
Linear expander	Maximum stroke [mm]	120.0
	Effective bore [mm]	80.0
	Inlet pressure [bar]	2.7
	Inlet temperature [K]	473.0
	Valve diameter [mm]	32.5
	Valve lift [mm]	8.13
Linear compressor	Maximum stroke [mm]	120.0
	Effective bore [mm]	70.0
	Inlet pressure [bar]	1.0
	Inlet temperature [K]	300.0
	Outlet pressure [bar]	2.75
Reactor (heater)	Inlet pressure [bar]	2.7
	Inlet temperature [K]	300
	Outlet temperature [K]	473.0
Linear generator	Load constant of the generator [$N/m\cdot s^{-1}$]	0.0
Simulated generator load	Additional moving mass [kg]	20

Table 6-2. Piston assembly dynamics.

Performance [Unit]	Value
Operation frequency [Hz]	5.26
Piston amplitude from central stroke [mm]	51
Peak piston velocity [m/s]	1.7
Peak piston acceleration [m/s^2]	100

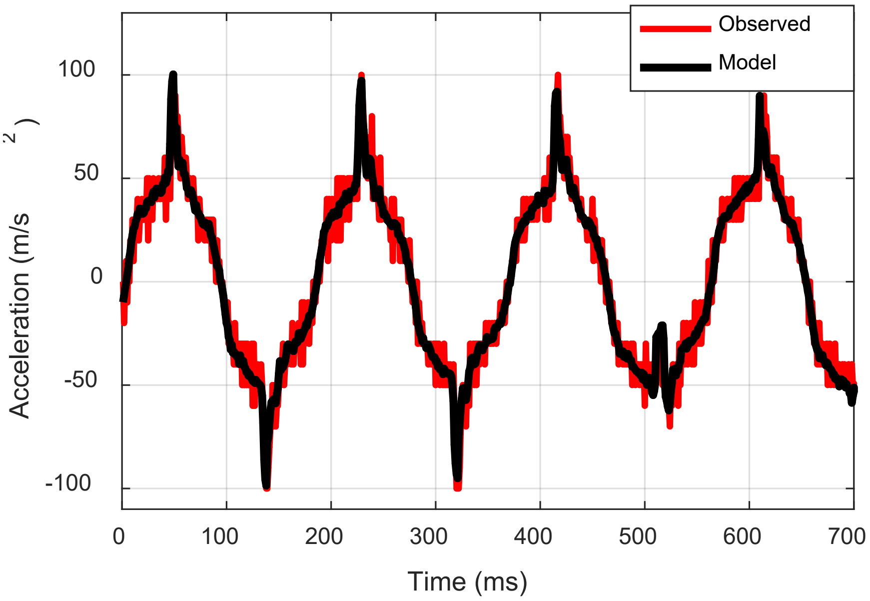

Figure 6-1. Piston assembly acceleration.

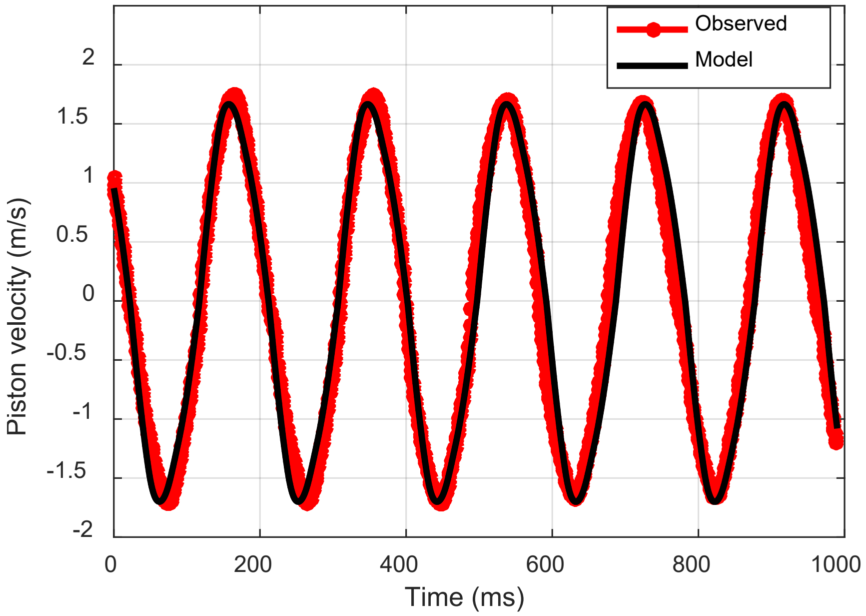

Figure 6-2. Piston assembly velocity.

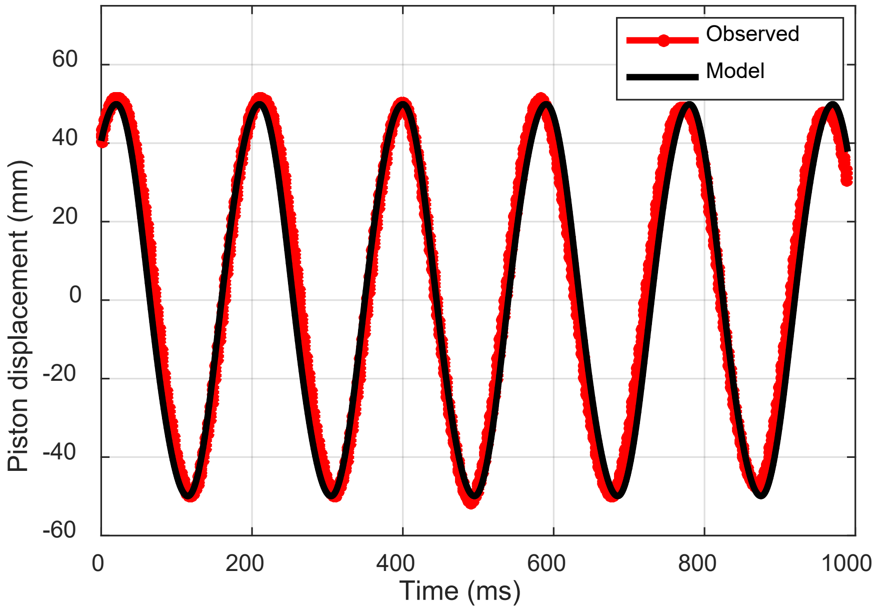

Figure 6-3. Piston displacement profile.

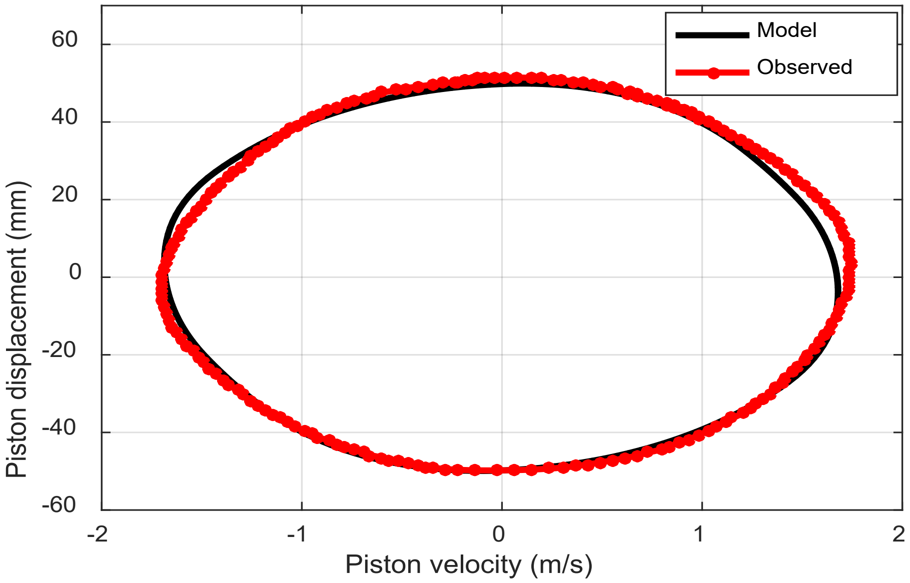

Figure 6-4. Piston displacement vs velocity.

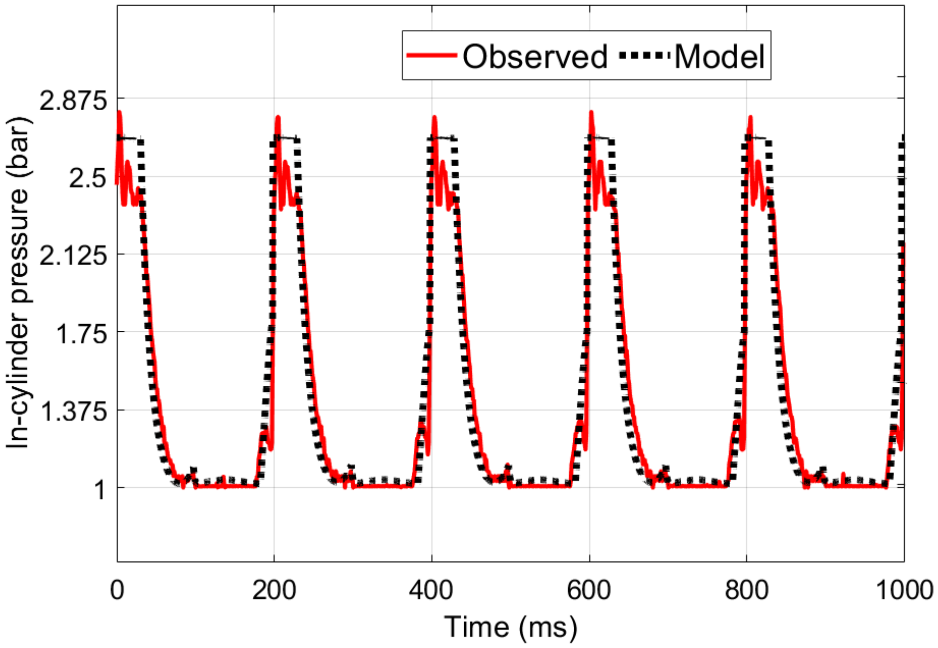

Figure 6-5. Right expander in-cylinder pressure profile.

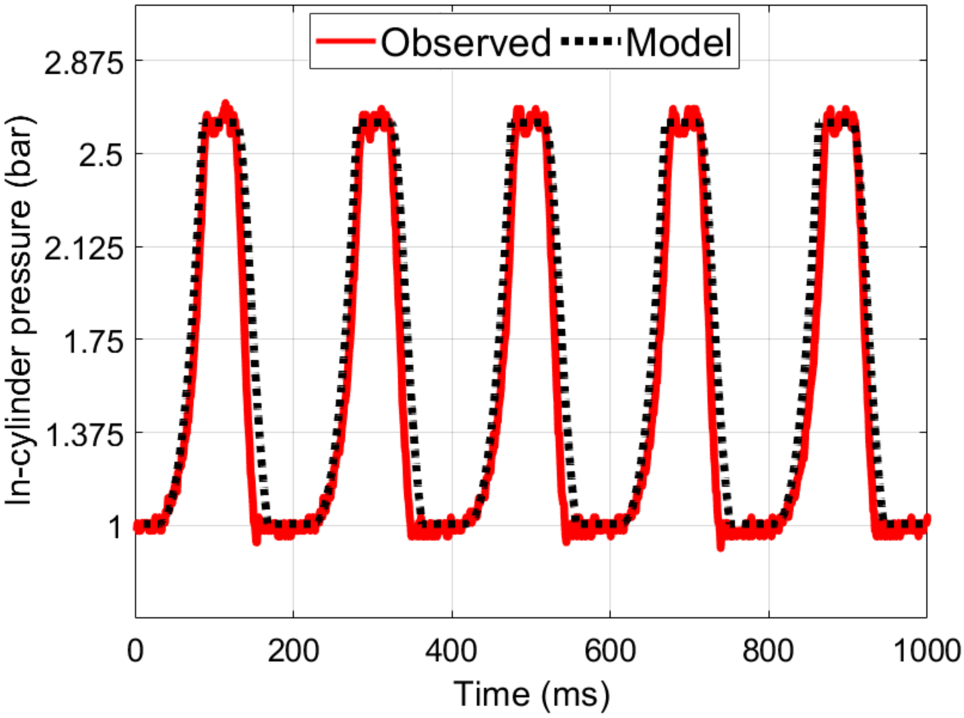

Figure 6-6. Left compressor in-cylinder pressure profile.

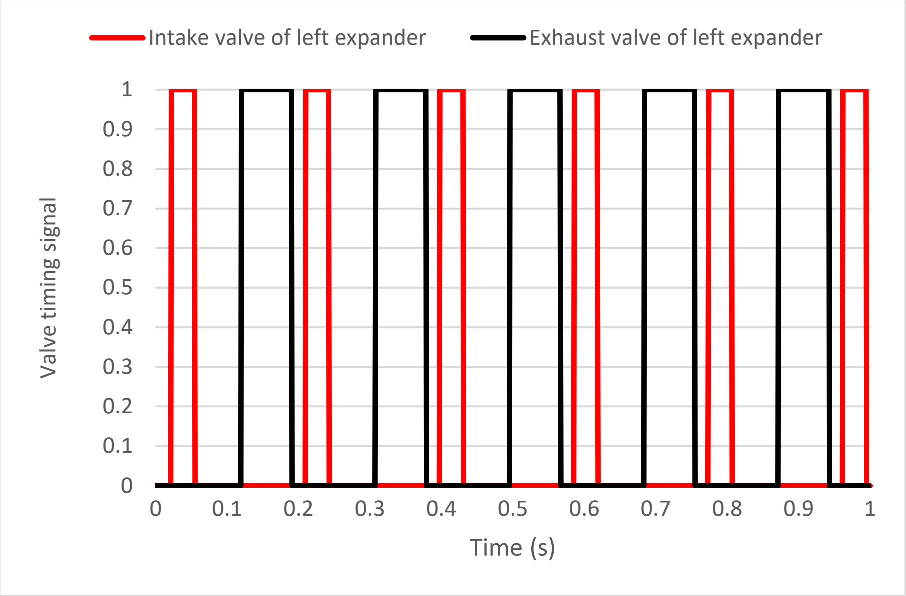

Figure 6-7. Valve inlet and outlet profile for left expander.

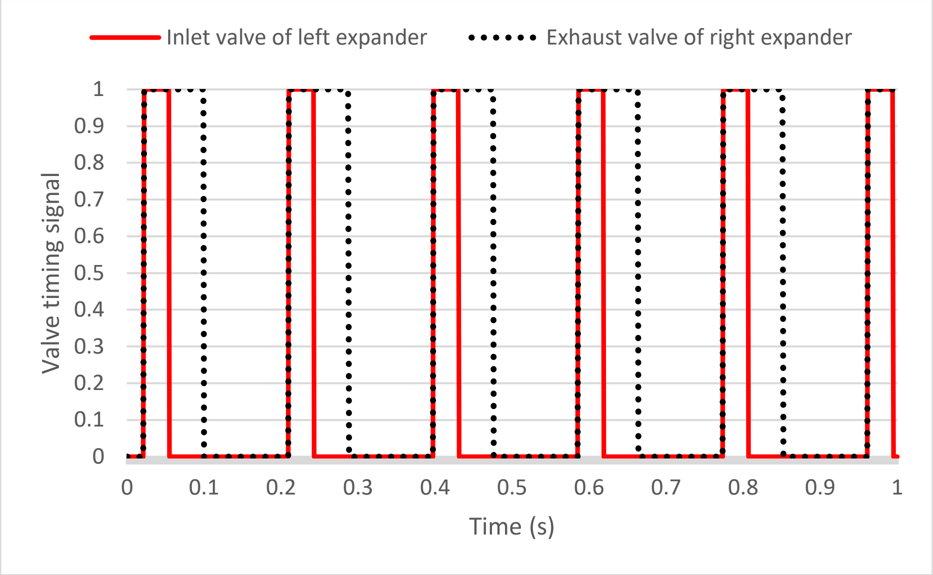

Figure 6-8. Left expander inlet valve and right exhaust valve profile.

It could be observed from Figure 6-4 that the piston assembly peak velocity occurs near the mid-stroke since the velocity is at minima at operating top and bottom dead centres. Figure 6-7 shows the inlet and exhaust valve timing for the left expander and Figure 6-8 shows the left expander inlet valve and the right expander exhaust timings; both the inlet and exhaust valves open at the OTDC. The prolonged opening of the exhaust valve was expected since the system made no use of a scavenging pump and the expander exhaust gas was at atmospheric pressure.

6.2 Combustion model validation

Combustion flame temperature is one of the unique and vital factors that characterised the combustion behaviour of a particular composition of fuel and oxidant. A comparison between the simulated data from the combustion model and measured data from Drell and Belles [158] for hydrogen-air mixtures combustion was carried out. The results are represented in Figure 6-9. The results presented in Figure 6-9 are for constant pressure combustion, with a pressure of 1.01325 bar and an initial mixture temperature of 298° K. The simulated temperature data generally corresponded to the measured data within the operating range of temperature expected of the LJEG [20]. Some regional discrepancies existed between the measured and the simulated data for temperatures above 2350° K. The discrepancies existed because the conversion rate for hydrogen was fixed in the combustion model and did not vary with temperature. However, the expected operating temperature for an LJEG combustor was entirely below 2350° K; therefore, the model is considered robust to predict the flame temperature for hydrogen-argon/oxygen mixture combustion.

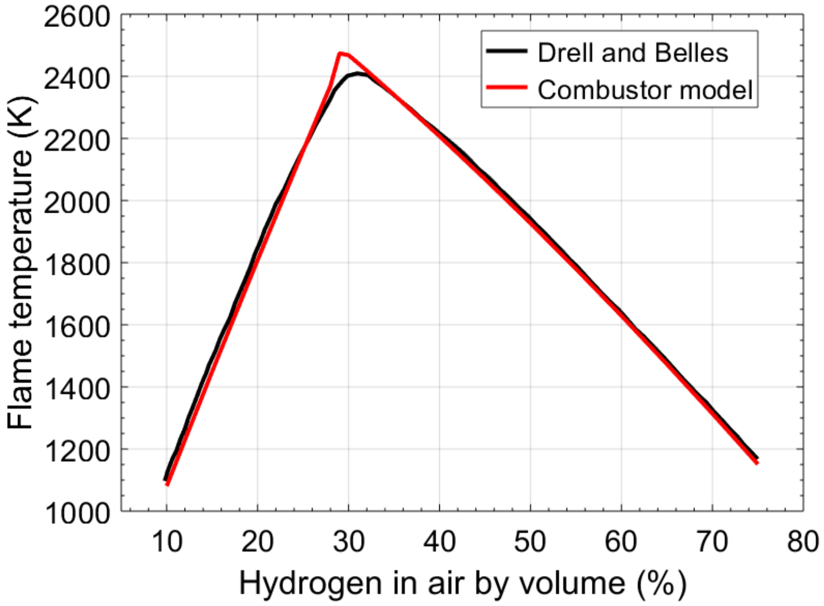

Figure 6-9. Flame temperatures for hydrogen-air mixtures.

6.3 Moving mass dynamics

This section describes the fundamental dynamics and thermodynamics characteristics of the semi-closed cycle LJEG. Table 6-3 shows the second-generation prototype main specifications and simulation input parameters. The simulated piston dynamic results of the system are demonstrated in Table 6-4.

Table 6-3. Main prototype specifications and input parameters

	Parameters [Unit]	Value
Linear expander	Moving mass [kg]	8.0
	Maximum stroke [mm]	120.0
	Effective bore [mm]	80.0
	Inlet pressure [bar]	7
	Inlet temperature [K]	1100.0
	Valve diameter [mm]	32.5
	Valve lift [mm]	8.13
Linear compressor	Maximum stroke [mm]	120.0
	Effective bore [mm]	70.0
	Inlet pressure [bar]	1.0
	Outlet pressure [bar]	7.0
Reactor	Inlet pressure [bar]	7.0
	Inlet temperature [K]	550
Linear generator	load constant of the generator [$N/m \cdot s^{-1}$]	736.0

Table 6-4. Piston dynamics

Performance [Unit]	Value
Operation frequency [Hz]	15.6
Piston amplitude from central stroke [mm]	37
Peak piston velocity [m/s]	3.5
Peak piston acceleration [m/s^2]	681

The piston displacement with time is demonstrated in Figure 6-10; the piston moved between its OTDC and OBDC from approximately −37.0 mm to +37.0 mm. The operating stroke was around 74.0 mm, and the clearance at each piston end was 23.0 mm. The operation stroke depended on the valve timings, the expander inlet pressure, and the generator's load. Details of the influence of valve timing, pressure and generator load are presented in the next chapter. The piston assembly velocity profile is shown in Figure 6-11, and a peak velocity of approximately 3.5 m/s is achieved.

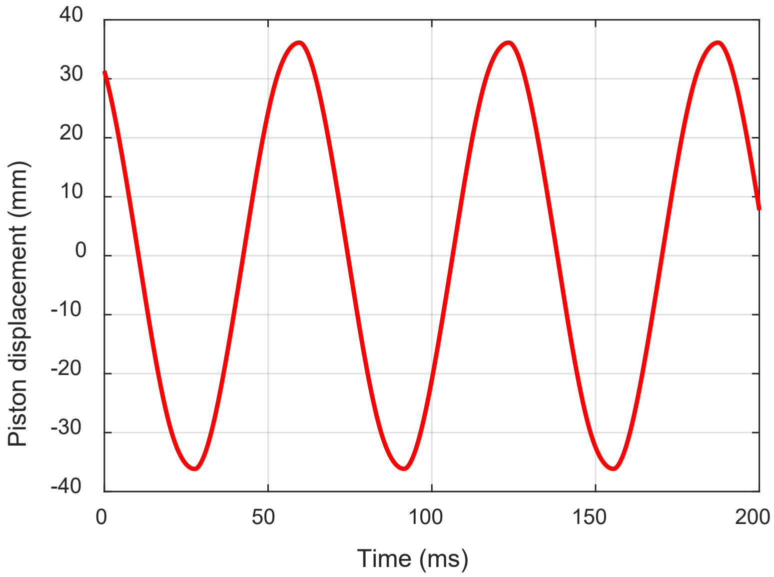

Figure 6-10. Piston displacement vs time.

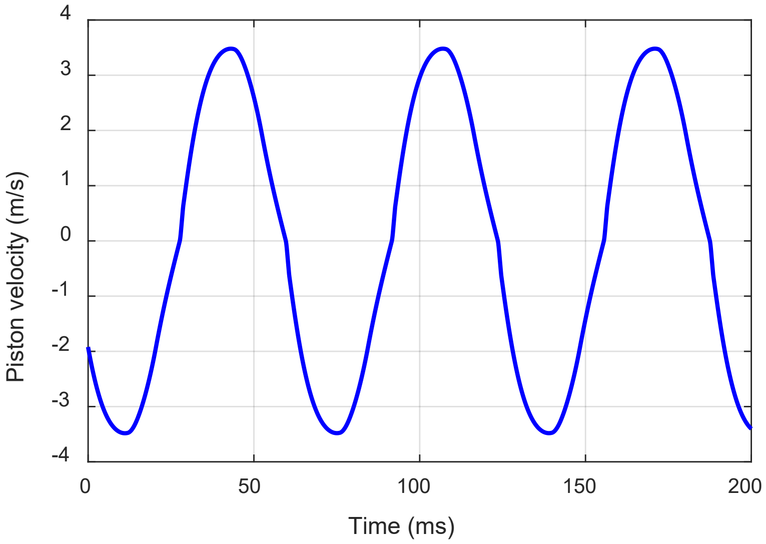

Figure 6-11. Piston velocity vs time.

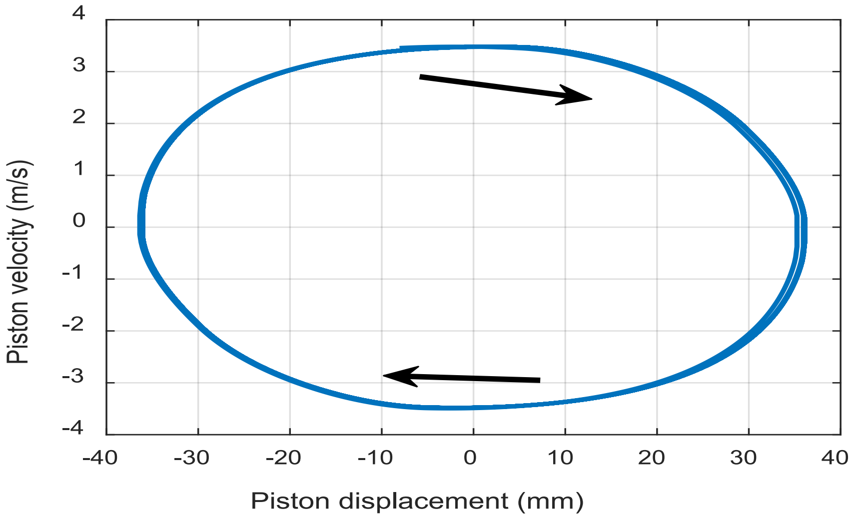

Figure 6-12. Piston velocity vs piston displacement.

The piston assembly velocity and displacement are demonstrated in Figure 6-12, and the forces acting on the piston assembly that contribute to the piston assembly inertia force are compared in Figure 6-13. It was found that the forces from the expander were highest among all the forces acting on the piston assembly. This force could reach up to 2943 N, and the peak force from the generator was about 2550 N. The peak force from the compressor was 2265 N, which was achieved at the end of the compression process; it stayed at the peak value during the outlet process. The resultant force from the expander, the compressor, the generator, and the frictional force, acts as an exciting force to drive the pistons to reciprocate.

The in-cylinder gas pressure in both chambers of the compressor is plotted in *Figure 6-14*. The pressure in the left chamber of the compressor, together with piston displacement, is shown in *Figure 6-15*, with the valves timing indicated on it. The compressor inlet pressure is set to ambient/atmospheric pressure, and the pressure in the compressor was assumed to be maintained at the ambient pressure when the intake valve of the compressor opened. The exhaust valve opened when the gas pressure in the compressor reached the target cycle pressure, which is 7.0 bar in this simulation.

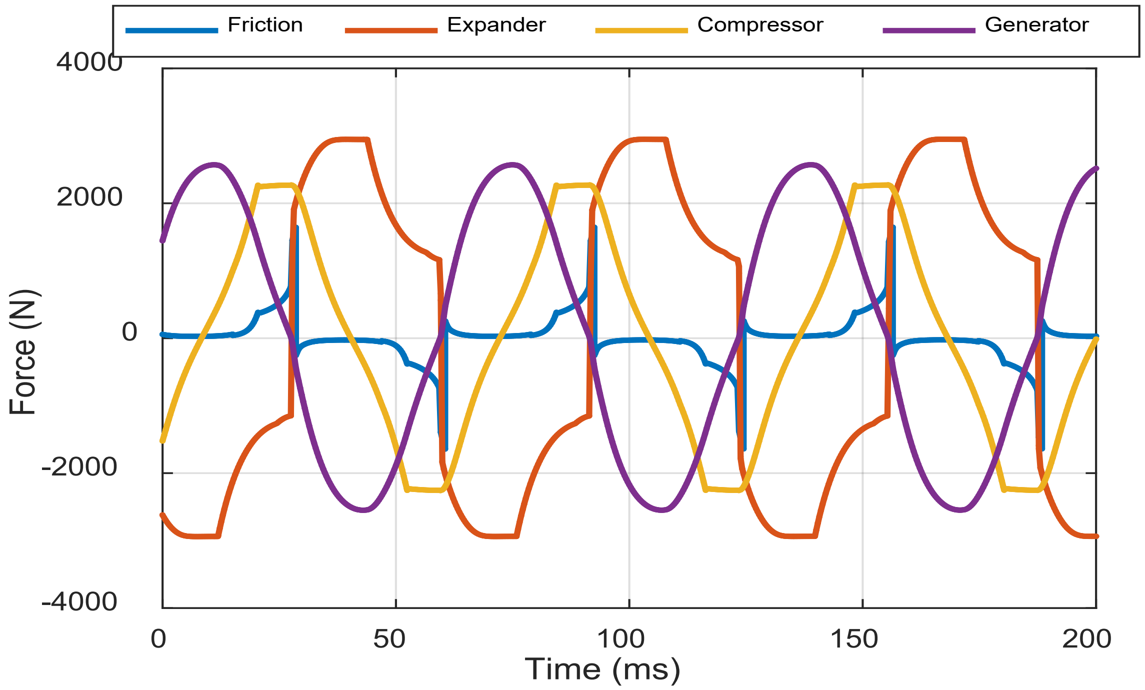

Figure 6-13. LJEG Forces vs time.

The pressure in the left chamber of the expander with piston displacement is shown in Figure 6-16, with all the valves timing marked on it. The outlet pressure to the expander is set at 7 bar, and the pressure in the expander is expected to be maintained at or below the ambient pressure before the exhaust valve closed (EVC) at the current valve timing operation. The exhaust valve timing of the expander depended on the type of operation adopted. At a high electrical load, like the case shown in Figure 6-16, the exhaust valve opened at 3.5 bar, but the exhaust valve would open at 1.2 bar at a low electrical load. This concept is discussed in detail in the later sections of the thesis.

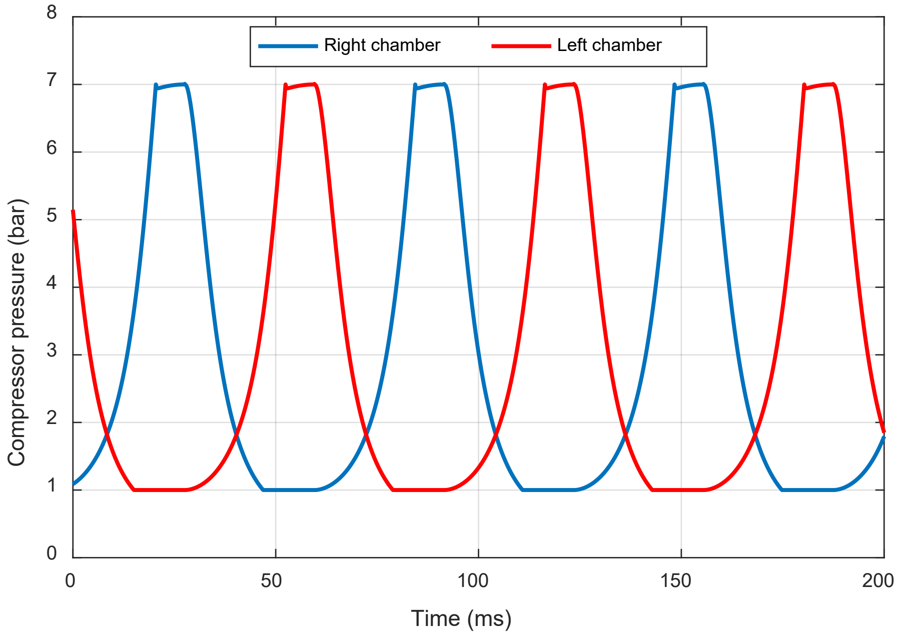

Figure 6-14. Pressure in both chambers of the compressor vs time.

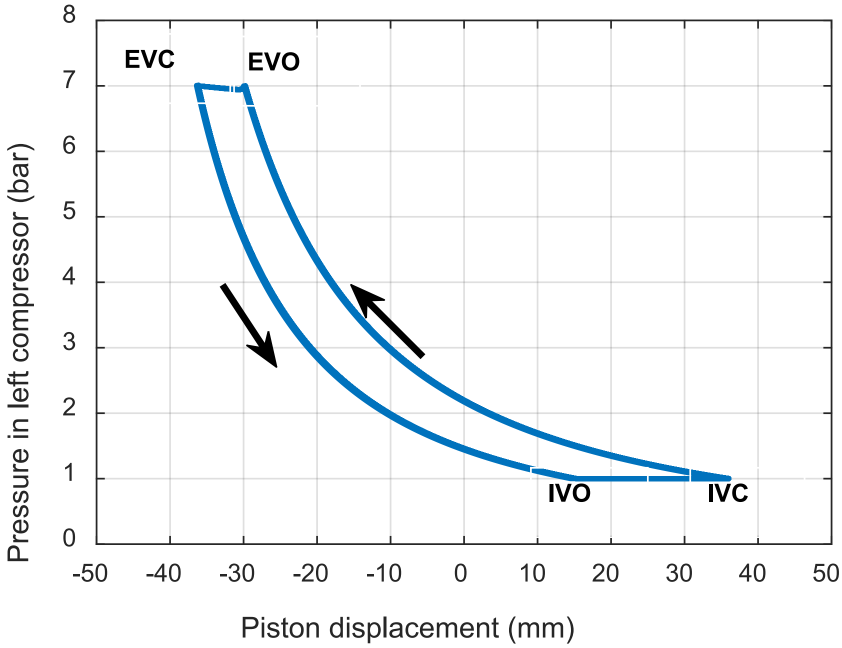

Figure 6-15. Pressure in the left chamber of compressor vs piston displacement.

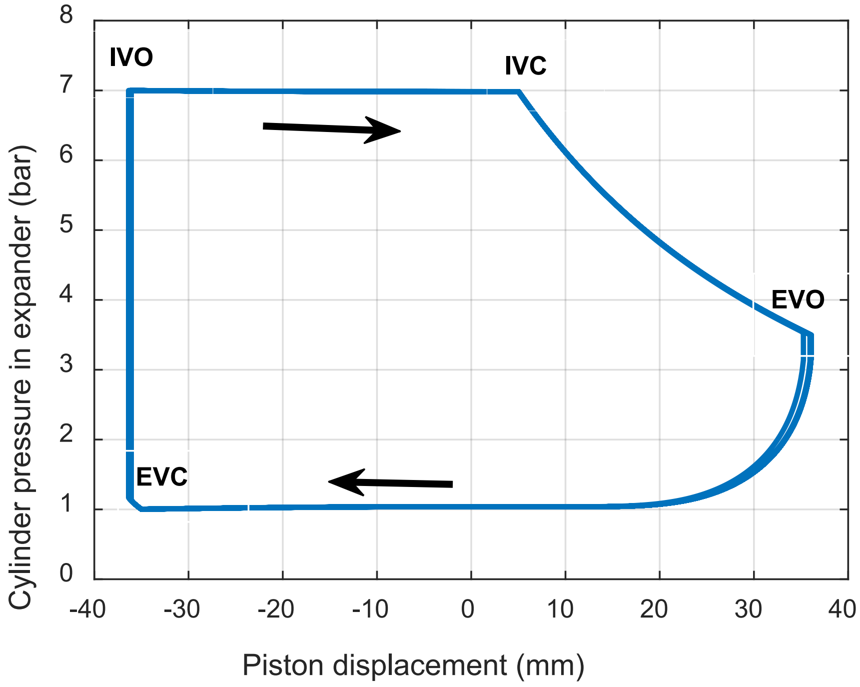

Figure 6-16. Pressure in the expander vs the piston displacement.

The simulation results discussed above were for an air-standard open cycle LJEG; therefore, it was not argon-oxy-hydrogen powered LJEG. The next section discusses the general influential operating characteristics of the LJEG.

6.4 Operating conditions

The system performance of the LJEG depends on the operational parameters, while design/geometric parameters were fixed during operation. The identified operational parameters in LJEG include the system pressure, the working fluid, the valve timing, and the linear generator's electric load. The working fluid, valve timing and system pressure could be used to alter the energy input, while the electric load could be used to adjust the energy output. The influence of the variable operating parameters on the system performance is discussed individually in the next section.

6.4.1 System pressure

The system power output with varying system pressure is shown in Figure 6-17, and all the other input parameters remained unchanged during the simulation. The range of the system pressure was set from 6.8 bar to 9.0 bar. If the system pressure was below 6.8 bar, while the generator load was at 736 Ns/m, the system was no longer stable and stopped after a few oscillations. This behaviour occurred because the pressure force from the expander would not be sufficient to drive the electric generator and as well overcome the compression forces of the compressor and friction force. The pressure of 9.0 bar represented the maximum the compressor configuration could reasonably achieve in a single-stage compression. It would be observed from Figure 6-17 that the electric power of the linear alternator and indicated power of the expander are nearly in a linear relationship with the system pressure. While the system pressure increased from 6.8 bar to 9.0 bar, the electric power improved from 4.1 kW to 7.1 kW, and the expander indicated power changed from roughly 5.0 kW to 9.2 kW.

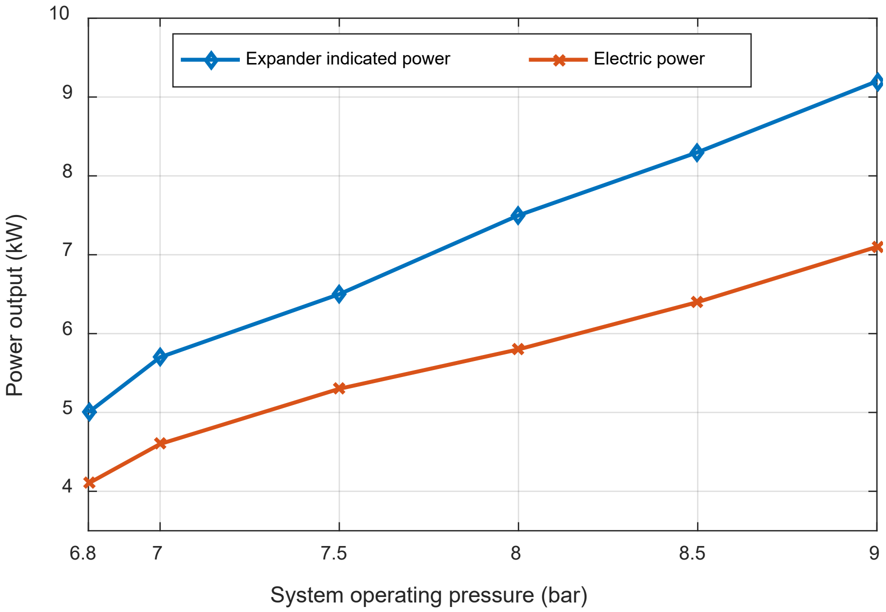

Figure 6-17. Power output with different system pressures.

The relationship between system pressure and the piston stroke is shown in Figure 6-18, and it could be observed that piston stroke increased with higher system pressure. The enclosed area in the pressure and displacement curve increased with higher system pressure, demonstrating that a higher expander indicated work per cycle was achieved at higher system pressure while other variables were kept constant. The thermal efficiency, the expander indicated efficiency and the frequency with varying system pressures are demonstrated in Figure 6-19. The system frequency increased with the system pressure and showed a linear relationship with the system pressure. The thermal efficiency increased with system pressure while the indicated efficiency dropped gradually despite higher system pressure. The value of the generator load used in this simulation was the maximum load that a 7 bar system pressure could sustain. Therefore, the indicated efficiency could increase with system pressure if the value of the generator load was slightly increased with increased system pressure.

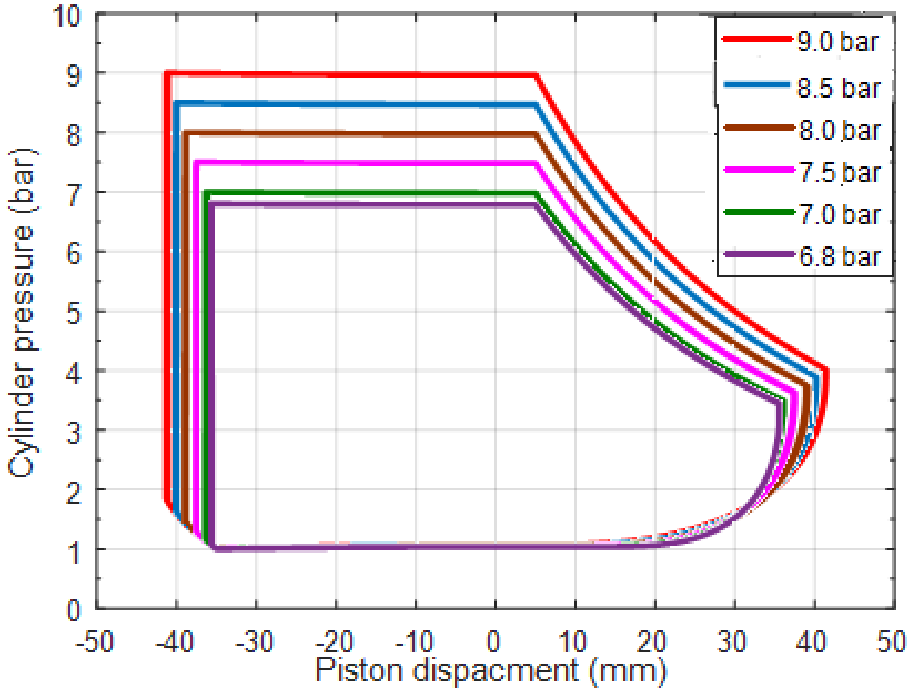

Figure 6-18. Expander cylinder pressure with different system pressures.

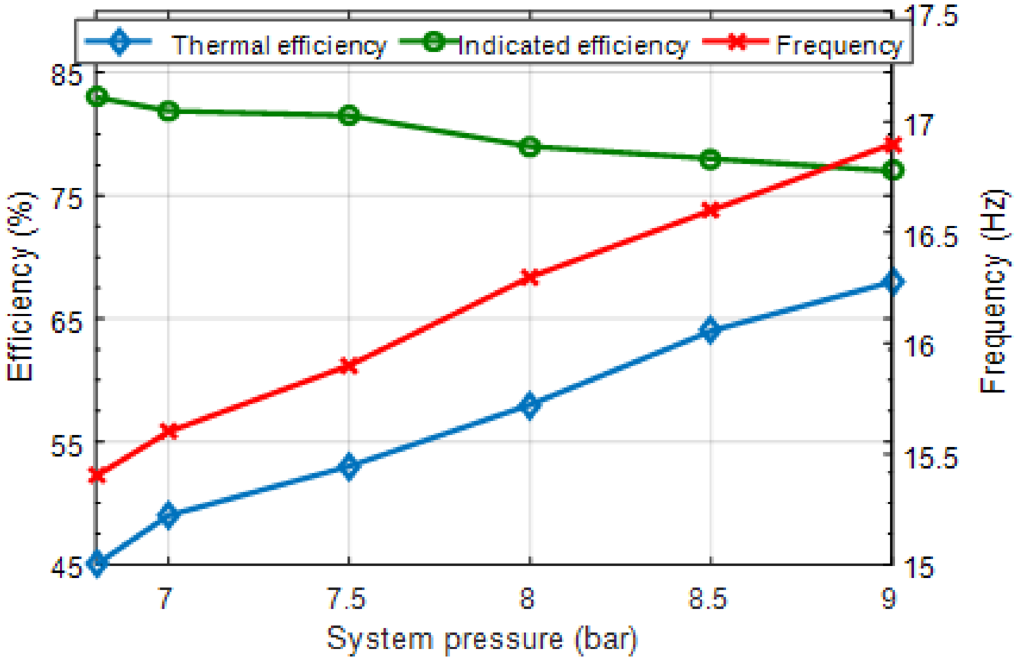

Figure 6-19. System efficiencies and frequency with different system pressures.

6.4.2 Valve timing

The expander's intake and exhaust valve timing played an essential role in the system performance. The intake timing operation and exhaust valve operation are illustrated in Figure 6-20 and Figure 6-21, respectively. In implementing the inlet and exhaust valve timing control, the instantaneous piston position and velocity were used as feedback inputs. The intake valve opened when the piston reached its operating top/bottom dead centre as the case may be, and the piston velocity approached zero. However, only the instantaneous piston position controlled the valves opening duration. Various instances of expander intake duration were considered, and the expander exhaust duration was fixed at 40 mm after the mid-stroke in all cases. Table 6-5 summarised the condition for every case.

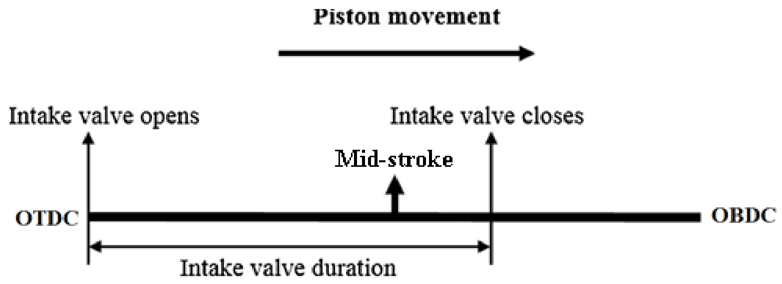

Figure 6-20. Illustration of expander intake valve timing.

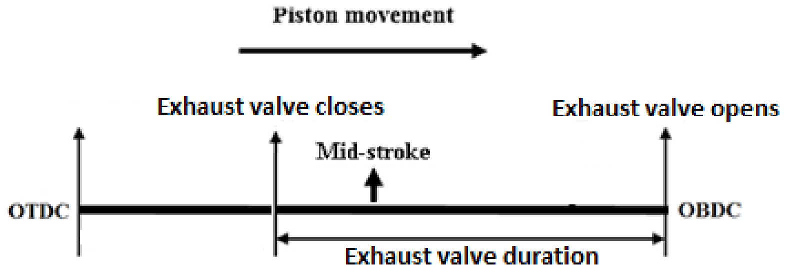

Figure 6-21. Illustration of expander exhaust valve timing.

Table 6-5 Intake valve closing timings.

Case number	Valve close position from the mid-stroke position (mm)
Case 1	-15
Case 2	-10
Case 3	-5
Case 4	0
Case 5	5
Case 6	10
Case 7	15
Exhaust valve	40 (all cases)

The intake valve timing in Table 6-5 illustrates its relative distance from the mid-stroke, as demonstrated in Figure 6-21. The nominal cycle system pressure was set to 7.0 bar, and the electric load constant of the generator was maintained at 400 (N/m·s^{-1}), while the other parameters remain unchanged during the simulation. Figure 6-22 shows the in-cylinder pressure of the expander and piston displacement with various intake valve-closing positions. Case 1 was not sustainable because the intake duration was too short. When the intake valve duration is too short, the resultant excitation force was insufficient to maintain stable operation; therefore, the system became unstable and stopped.

It could be observed from Figure 6-22 that with a shorter intake duration, the piston displacement/stroke was less, and the expander indicated work smaller (from case 2 up to case 7) and vice versa (from case 7 down to case 2) for a more extended intake duration. The in-cylinder pressure at the OTDC before the intake valve opened (point 1 on Figure 6-22), as well as the in-cylinder pressure at the OBDC before the exhaust valve opened (point 3 Figure 6-22), would be higher with an extended intake duration (from case 7 down to case 2).

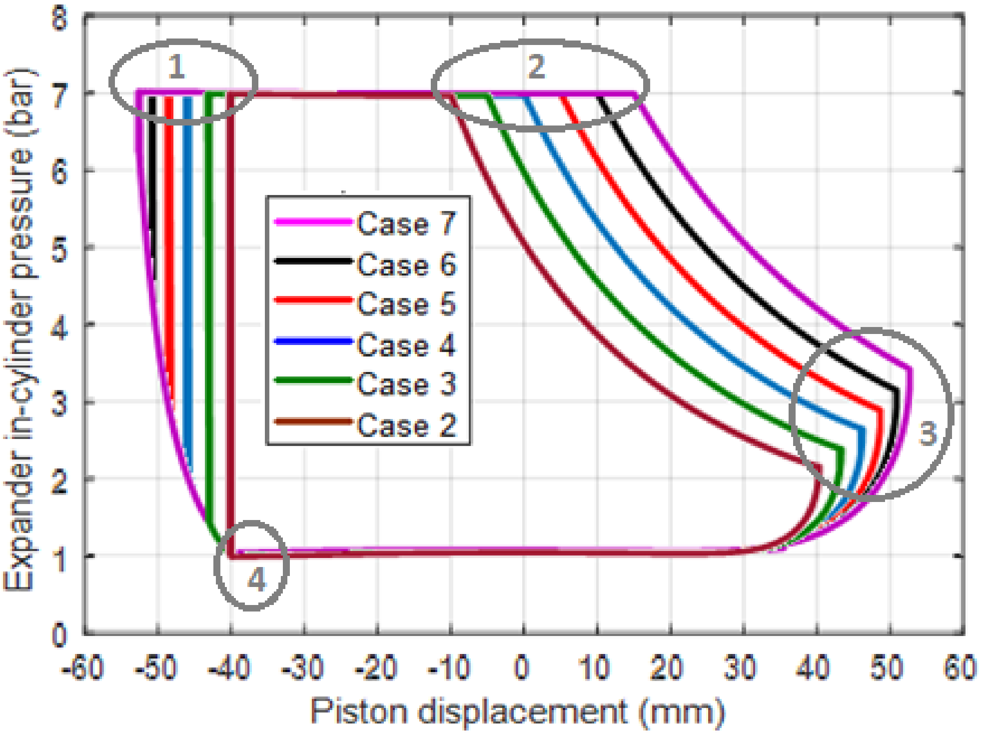

Figure 6-22. Expander cylinder pressure with different valve timings.

A high in-cylinder pressure before the exhaust valve opened would lead to energy loss in the whole system because the energy in the working fluid was not fully utilised in the expansion process. The relationship between the system electric power outputs, expander indicated power, thermal efficiency and indicated efficiency with different valve timing operations are shown in Figure 6-23. It was found that the thermal efficiency, electric power output and expander indicated power increased with extended intake duration while the indicated efficiency decreased with extended intake duration. Therefore, to have a positive gradient of the system's indicated efficiency, a higher electric load would be required when operating the LJEG at an extended intake duration, such as to extract the most energy from the expander.

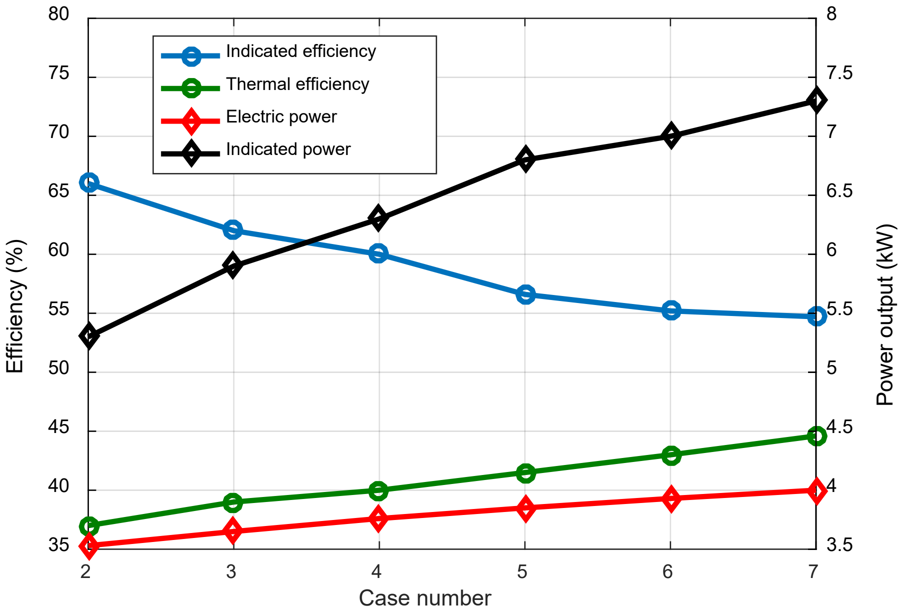

Figure 6-23. Power output and efficiency with different valve timing.

6.4.3 Generator electric load

The system performance with various generator loads was simulated to evaluate the effect of generator load on the characteristics of the LJEG. At the same time, the rest of the other input parameters were unchanged during the simulation. The nominal system pressure was set to 7.0 bar, and the valve timing Case 4 in Table 6-5 was adopted.

The relationship between the expander work, piston amplitude and electric load are shown in Figure 6-24. At lower electric loads, the expansion work and the piston amplitude were higher, and the possibility of complete expansion increased with a decreased electric load. The piston dynamics with various electric loads are shown in Figure 6-25. It was found that both the piston amplitude and the peak piston velocity increased with a lower electrical load. However, the peak piston velocity was obtained after the mid-stroke, and this was because the intake duration ended at mid-stroke, and the effect of the resultant force must be felt after mid-stroke. The piston velocity had a more rapid deceleration than acceleration, and this is because of the LJEG friction features, which typically increased during deceleration. **Figure 7-13** and **Figure 7-14** shown in Chapter 7 could help in understanding the slow acceleration and quick deceleration pattern observed in Figure 6-25.

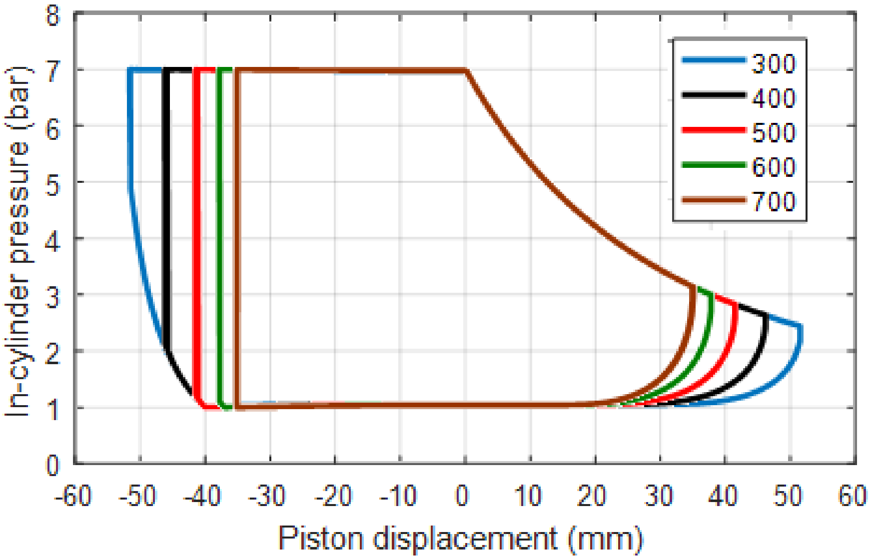

Figure 6-24. Expander in-cylinder pressure [bar] with different generator load [N/m·s^{-1}].

The system power output with various electric loads is shown in Figure 6-26. The expander indicated power decreased with increased electric load, but the electric power generation and indicated efficiency increased with the electric load. The indicated efficiency exhibited a somewhat linear relationship with the electric load. Under the specific simulation conditions (valve timing and system pressure), any value of electric load outside the chosen range would result in unstable operation. Therefore, there would always be a range of operable electric loads for any set of operating parameters to avoid unstable operation.

The system must be operated more at the upper side of the electrical load range to maximise the electric power output within any operable range.

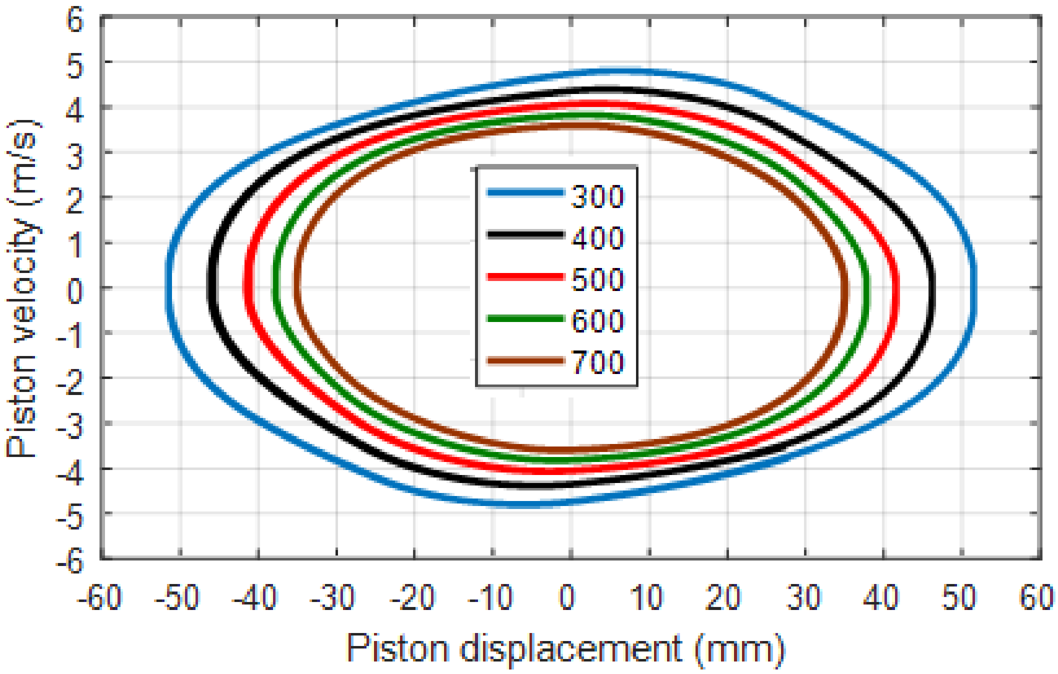

Figure 6-25. Piston velocity [m/s] and displacement [mm] with different generator load [N/m·s^{-1}].

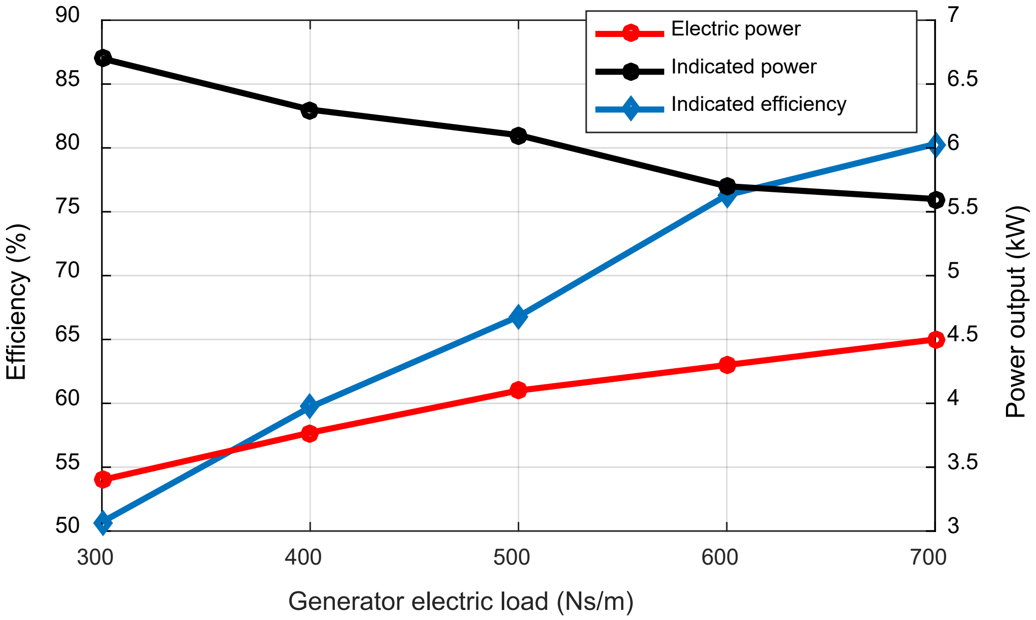

Figure 6-26. Power output and efficiency with different electric load.

6.4.4 Working fluid

The compressor volumetric discharge per stroke on its own did not affect the system performance, but it had an overwhelming influence on the expander valve timing. The LJEG system had a specific minimum compressor volumetric discharge for stable operation for specified thermodynamic variables and electric load. The compressor volumetric discharge is directly related to the expander intake timing operation. The quantity of available working fluid from the compressor would determine the mass of fluid from the reactor, and the mass of fluid from the reactor could determine the expander intake duration. In a piston-type compressor, as with the LJEG system, the volumetric discharge depended on the selected operating parameters as long as other thermodynamic variables remained the same. However, while all the other operating parameters and thermodynamic variables remained the same, and the working fluid was changed, the thermos-physical properties of the working fluid affected the compressor discharge. Table 6-6 shows the compressor volumetric discharge per stroke and corresponding piston displacement with argon and air used as the working fluid while all the other variables remained the same. The piston displacement was 4.4% more with air as the working fluid, but the volumetric discharge per stroke was 27.3% greater with argon. More prolonged expander intake could be achieved with argon because of its higher heat capacity ratio compared with air; though, this advantage is without considering the effect of specific heat capacity at constant pressure on the two working fluids when they undergo external heat addition in the combustor.

Table 6-6. Effect of working fluid on volumetric discharge

Working fluid	Volume (m^3)	Piston displacement (mm)
Air	5.5×10^{-5}	94
Argon	7×10^{-5}	90

6.5 Argon use justification

The simulation results for a semi-closed cycle argon-oxy-hydrogen LJEG model were compared to test data from the first generation open-cycle air-standard LJEG prototype developed at Newcastle University and presented in [22]. The LJEG simulation specifications were set to be identical to the prototype. The model and prototype input parameters are listed in Table 6-1. This comparative study was undertaken to verify the performance improvement of argon as a working fluid, compared to air, in a semi-closed cycle operation of LJEG. The results of the test data and our model are presented in Table 6-7. The simulation results of the open-cycle air-standard operation were similar to the test data, and it further showed that the model had produced realistic results. When argon was employed as the working fluid, and all other parameters were kept the same, the results indicated the following: an increased argon flow rate and increased system speed, a slightly decreased indicated power, and over 60% improvement in indicated efficiency. The major efficiency improvement was attributed to the thermo-physical properties of argon; the density and specific heat ratio of argon gas are higher when compared to air, and the specific heat ratio of argon does not decrease at high temperatures, unlike air [109].

Additionally, the constant pressure specific heat capacity of air increased with temperature, but the same property (constant pressure specific heat capacity) remained constant in argon at higher temperatures [133]. It implied that more energy would be needed in the combustor per Kelvin temperature rise with air being used as the working fluid, but such increased energy demand would not occur if argon were used. The target design pressure ratio for the LJEG operation is about 7.0. It is expected that when argon is the working fluid, the system will replicate a similar improved efficiency at such a pressure ratio. A recent study on hydrogen-powered air-standard free-piston engine generator indicated that oxides of nitrogen (NOx) emissions could be above 80ppm [159]. NOx emissions would be eliminated in argon-oxy-hydrogen combustion. Therefore, adopting a closed-cycle argon-oxy-hydrogen LJEG would lead to improved system efficiency and reduce emissions.

Table 6-7. Comparison between the prototype test results and model simulation results.

	Test data	Simulation	Simulation
Working fluid	air	air	argon
Cycle	open	open	closed
Speed (Hz)	5.26	5.27	5.59
Flow rate (Kg/s)	0.00945	0.00973	0.01131
Indicated power (W)	762	765	734
Indicated efficiency (%)	40	39	62.5

6.6 Conclusions

In this chapter, the numeric validations of the dynamic, thermodynamic and combustion models of the LJEG were carried out, and the performance characteristics of the system with different operating conditions were presented. Results indicated that the system performance depended on some operational parameters, and the essential parameter in LJEG analysis would be the working fluid and pressure. However, they were not in isolation from other vital parameters such as valve timing and electric load. The adjustable operational parameters were identified as valve timing and generator electric load. The valve timing and electric load are meant to be optimised depending on the preference between engine efficiency and power output. The influence of valve timing and electric load on the system performance was different. It was found that the valve timing was the most effective parameter to achieve a higher electric power from the generator.

In contrast, the electric load was found to be the most influential parameter for the indicated efficiency improvement. When air was replaced with argon as the working fluid, the results indicated an increased argon flow rate, a slightly decreased indicated power output, and above 60% indicated efficiency improvement. Detailed system optimisation of operational and geometric variables is presented in Chapter 7.

Chapter 7: Friction force model description and validation

7.1 Frictional force background and analysis

Friction losses are considered among the significant factors that limit the system performance of most mechanical systems. It affected the energy footprint of a system through wear and decrease in energy conversion efficiency. In a traditional internal combustion engine, piston assembly could be responsible for 45% of total frictional losses, and most piston assembly losses were directly attributed to piston ring cylinder-liner interface [160]. In internal combustion free-piston engines, friction loss at the piston ring cylinder-liner interface accounted for more than 55% of total frictional loss [161]. Friction losses in Free Piston Engine (FPE) were expected to be lower than that of the traditional internal combustion engines due to the elimination of the piston skirt and crank mechanism [47].

There are a few research publications in the open literature on friction behaviour in FPE configuration. Among the very few, most of the published research articles investigated internal combustion FPEs, where hydrodynamic lubrication was predominant. Tian et al. [162] and Zhang et al. [163] considered the frictional force in FPE to be a damping force, which was directly proportional to sliding piston velocity, while the direction of friction force was opposite to piston velocity. Similarly, a study on Free-Piston Expander Linear Generator for small-scale Organic Rankine Cycle [164] suggested that the frictional force behaved like a viscous force that was directly proportional to sliding piston velocity. Goldsborough and Van Blarigan [165] analysed frictional force in internal combustion FPE as the sum of Coulomb and viscous frictions, and the viscous friction was proportional to piston velocity, where the direction of the sum of frictional forces was opposite to piston velocity. Lee [166] adopted the same approach and used Coulomb and viscous frictions to simulate friction force in an internal combustion free-piston linear generator, while the direction of friction was opposite to piston velocity. A study on free-piston expander linear generator without lubrication identified that Coulomb and viscous frictions were the main types of friction acting on the system. The authors applied the Coulomb and viscous friction parameters as 98.3 and 178.6, respectively, for the calculation [167].

The friction force of FPE with opposed piston configuration [168] was reported for a two-stroke spark ignition system and regarded as a constant numerical value over the whole stroke. Similarly, a study on a single-cylinder, two-stroke spark ignition FPE [169] proposed that the friction force was considered a constant numerical value over the full stroke. Meanwhile, Mikalsen and Roskilly [45] proposed that the friction force for two-stroke compression ignition FPE could be regarded as a numerical constant throughout the piston stroke. Yuan, Xu, and He [170] demonstrated that the friction force of FPE was affected by the in-cylinder gas conditions and piston dynamics and therefore stated that the friction force of the FPE could not be regarded as a numerical constant. Consequently, the authors presented a friction model that consisted of three friction components; viscous friction, the Coulomb friction force, and friction generated because of the in-cylinder gas pressures. Wu et al. [93] presented a friction force model for the FPE representing three friction components; the viscous friction, the Coulomb friction and the windage friction. Jia et al. [161] used the fundamental theory of lubrication, applicable to conventional crankshaft engines, to simulate the dynamic friction behaviour of FPEs. The results showed that the piston ring cylinder-liner friction force was higher in the FPE than the crankshaft engines. Nevertheless, the elimination of the crankshaft mechanism in the conventional crankshaft engines comparatively reduced the frictional loss in the FPE, thereby reducing the total friction losses of the FPE to nearly half of that of a crankshaft engine.

Various engine developers and researchers have pointed out that a reduction of friction loss in engine components was a positive mode of improving the mechanical efficiency of an engine [171]. Very few detailed researches have been carried out on the friction force behaviour in FPEs; however, most of the published investigations on friction force for different FPEs adopted the conventional lubrication principles. While the dry friction phenomenon is well established, analysing a dynamic system with dry friction components remained challenging, mostly when the excitation source was chaotic. In order to reduce the power loss due to friction, an understanding is required of how engine parameters affected friction development. Consequently, there is a need to develop a bespoke model to represent the friction processes of an LJEG. This bespoke model would help to develop the analytical tools needed for the design of low friction engine components [172], as well as understand the optimal range of engine operating parameters to minimise friction loss and to develop a robust friction model that could be used in dynamic LJEG analysis to estimate actual engine generator output. This chapter presents a novel friction model of an LJEG, which could be adapted and applied to other different types of FPE operating with a dry friction mechanism. The model is validated with the observed prototype test data. The need for developing a novel friction model was inspired by a lack of any detailed dry friction model that could describe the friction behaviour of the LJEG and the resolve to have a complete, robust and accurate system model that could predict the specifics and the general operational performance of the LJEG.

7.2 LJEG dynamic structure

The forces acting on the piston assembly were the gas pressure forces from the linear expander and the compressor, the resistance force from the linear generator, the in-cylinder frictional force, and the inertia of the moving mass, which determined the piston dynamics. The forces acting on the piston of LJEG, as shown in Figure 7-1, could be expressed as follows according to Newton's Second Law [20]:

$$\overrightarrow{F_e} + \overrightarrow{F_c} + \overrightarrow{F_g} + \overrightarrow{F_f} = m\ddot{x} \tag{7-1}$$

$$\overrightarrow{F_e} = \overrightarrow{F_{el}} + \overrightarrow{F_{er}} \tag{7-2}$$

$$\overrightarrow{F_c} = \overrightarrow{F_{cl}} + \overrightarrow{F_{cr}} \tag{7-3}$$

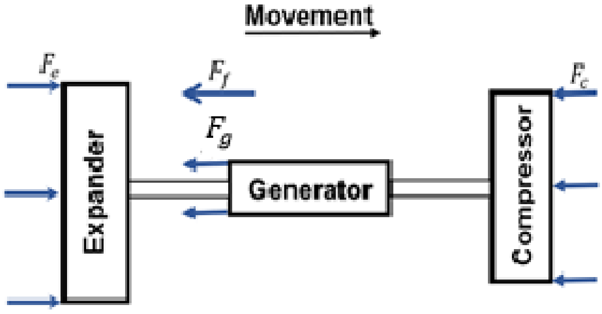

Figure 7-1 Schematic of the forces acting on the piston assembly of LJEG

Where $\overrightarrow{F_e}$ (N) is the pressure force from the linear expander; $\overrightarrow{F_{el}}$ (N) is the pressure force from the left chamber of the linear expander; $\overrightarrow{F_{er}}$ (N) is the pressure force from the right chamber of the linear expander; $\overrightarrow{F_c}$ (N) is the pressure force from the linear compressor; $\overrightarrow{F_{cl}}$ (N) is the pressure force from the left chamber of the linear compressor; $\overrightarrow{F_{cr}}$ (N) is the pressure force from the right chamber of the compressor. $\overrightarrow{F_f}$ (N) is the friction force, $\overrightarrow{F_g}$ (N); the generator force, $\ddot{x}$ (m/s^2); piston acceleration, m (kg); moving mass. The gas forces from both chambers of the linear expander and compressor was obtained using the gas pressure and piston effective area.

$$\overrightarrow{F_{el}} = p_{\mathrm{e}l} \cdot A_e \tag{7-4}$$

$$\overrightarrow{F_{er}} = p_{\mathrm{er}} \cdot A_e \tag{7-5}$$

$$\overrightarrow{F_{cl}} = p_{\mathrm{c}l} \cdot A_c \tag{7-6}$$

$$\overrightarrow{F_{cr}} = p_{\mathrm{cr}} \cdot A_c \tag{7-7}$$

Where $p_{\mathrm{e}l}$ (Pa) and $p_{\mathrm{e}r}$(Pa) are the cylinder pressure in the left and right chamber of the expander respectively. p_{cl} (Pa) and p_{cr} (Pa) are the cylinder pressure in the left chamber of the compressor respectively. A_e (m^2) and A_c (m^2) represent the piston areas for the expander and compressor respectively.

7.3 Friction model

A simple approach to modelling the frictional force of LJEG is proposed. The mathematical expressions of the friction model were developed based on experimental observation and other established friction principles. The friction model presented has two components; the first part was the static and dynamic dry contact friction force that occurred on the contact surface of the piston ring and cylinder liner, while the second part was friction due to pressure loading. The expression for the total friction is represented in Equation 7-8. The following assumptions were made to arrive at Equation (7-8):

- The cylinder liner and the piston ring were in direct contact because the piston has a crosshead piston arrangement without any side forces; therefore, the piston skirt friction was neglected.
- The piston ring did not twist.
- The thermal and elastic deformations of the ring and cylinder liner were neglected.
- The dynamic and static friction coefficients did not change with pressure and temperature.

$$F_f = \text{Dry contact friction} + \text{Pressure friction loading} = F_{fd} + F_{fp} \qquad 7\text{-}8$$

Where F_f; total friction force, F_{fd}; dry contact friction force, F_{fp}; pressure friction force.

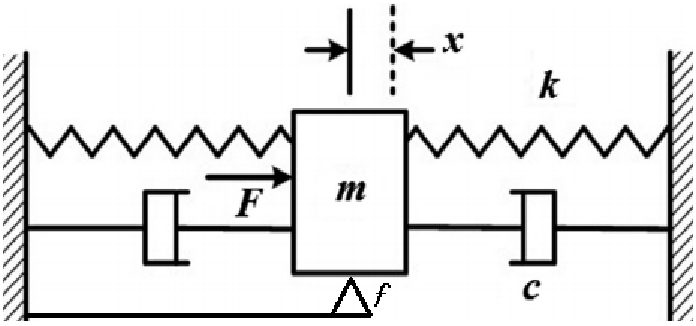

Figure 7-2. Analogous forced vibration system.

Equation (7-1) could be simplified to one degree of freedom forced vibration system [173] and represented as a forced vibration system with viscous damping and spring constant [174]' as illustrated in Figure 7-2. Figure 7-2 could also be described as a model of one degree of freedom mechanical oscillator, to which a dry friction damper is attached. The system dynamics could be defined by the second-order differential equation, as depicted in Equation (7-9) [15]:

$$m\ddot{x} + c\dot{x} + kx = F(t) \qquad 7\text{-}9$$

$$F(t) = F_e - Nf \qquad 7\text{-}10$$

Where c is the constant of the damping coefficient; k the constant of proportionality of the spring constant; and $F(t)$ is the continuing excitation force; F_e is the force provided by the expander, compressor and generator forces; N is the ring normal pressure force; f is a friction function. The analogy between a mass spring damper and an LJEG system is expressed in Table 7-1.

Table 7-1 Analogy between a mass-spring damper and a LJEG system

Mass-spring damper	**LJEG system**
Moving mass, *m*	Mass of the piston assembly
Damping coefficient, *c*	Linear generator load force
Spring constant, *k*	In-cylinder compressor force
Excitation force, $\boldsymbol{F_e}$	In-cylinder expander force
Normal force, *N*	Piston ring normal force
Friction function, *f*	Inter-surface friction coefficient

The first part of Equation 7-8, that is, the static and dynamic dry contact friction of the LJEG, was modelled as a dry friction oscillator represented in Figure 7-2, with the assumptions that the ring did not twist and there is no thermal and elastic deformation on the ring and cylinder liner. Therefore, only frictional force during macroscopic sliding motion with very short stops was considered rather than the stick-slip motion of the contact surface. The stick-slip effect was neglected since the piston was accelerated with a force much larger than the stiction force [167]. Dry friction problems have been investigated extensively [175], and considering a dynamic system where the relative velocity between contact surfaces was virtually constant; therefore, the simplest friction model described by the Coulomb law would serve [176]. In the LJEG and most practical cases, the relative velocity between the contact surfaces varied hugely and changed its sign. In such conditions, the preferred model must account for the transition from static to dynamic friction and must provide the means of guiding the system through zero relative velocity [176].

A dynamic model that could account for the hysteretic behaviour of dry friction force during macroscopic sliding at variable velocity was proposed by Powell and Wiercigroch [177], and it showed that non-reversible friction characteristics depended on both the relative acceleration and velocity of the contact surfaces. The dry friction model adopted for this analysis was presented by Stefański et al. [176] and represented in Equations (7-11) and (7-12). The materials for the contact surface (cylinder liner and the piston ring) were graphite on steel.

$$F_{fd} = \begin{cases} F_{fu,}\ sgn(\ddot{x}) > 0 \quad F_{fu} = Nf_d\left[1 + \dfrac{f_s - f_d}{f_d}\mathrm{g}(\ddot{x})\right] \\ F_{fl,}\ sgn(\ddot{x}) < 0 \quad F_{fl} = Nf_d\left[1 - \dfrac{f_s - f_d}{f_d}\mathrm{g}(\ddot{x})\right] \end{cases} \tag{7-11}$$

$$g(\ddot{x}) = exp\left(-\frac{a_1|\dot{x}|}{|\ddot{x}| + a_2}\right) \tag{7-12}$$

Where a_1, a_2 (> 0) are constant parameters, f_s, f_d; static and dynamic friction coefficient respectively, $F_{fu,}$ and F_{fl} represent the friction force relative to the acceleration and retardation phases, respectively. Equations (7-11) and (7-12) model the frictional memory during the slip phase by the function a_1 and a_2, while non-reversibility is modelled by + and - signs in quadratic brackets of Equation (7-11). The second part of Equation 7-8; frictional force due to system pressure loading is represented thus:

$$F_{fp} = \frac{bP_c}{P_a} e^{\left(\frac{b\dot{x}_m}{1+|\dot{x}|} + \frac{bP_c}{P_a}\right)} \tag{7-13}$$

$$b = \left(\frac{z_1}{|\ddot{x}_m| + z_2}\right) \tag{7-14}$$

Where P_c is the in-cylinder compressor pressure (bar), P_a atmospheric pressure (bar), $|\dot{x}|$ the absolute piston sliding velocity (m/s), $\dot{x}_m$ the mean piston velocity (m/s), $\ddot{x}_m$ the mean piston acceleration ($^{m}/_{s^2}$), z_1 and z_2 are friction parameters.

7.4 Results

The experimental procedure and data acquisition and control of the LJEG system were described in section 4.2. The recorded experimental data, compressor pressure P_c, expander pressure P_e and piston displacement x, were used to calculate the variables in equation (7-15).

$$F_e = P_e \times A_e, \qquad F_c = P_c \times A_c, \qquad A_e = \frac{\pi d_e^2}{4}, \qquad A_c = \frac{\pi d_{co}^2}{4},$$

Where F_f is the friction model in Equation (7-8). The values for other input parameters during the experiment are listed in Table 7-2. See Table 7-3 and Figure 7-3 for the details of the piston ring. The following values were used for the constants in Equations (7-12) and (7-14). $a_1 = 21$, $a_2 = 0.9$, $z_1 = 183$ and $z_2 = 80$, $f_s = 0.1$ and $f_d = 0.095$. Expander ring compression pressure = $0.02\ \mathrm{N/mm^2}$. Compressor ring compression pressure = $0.0256\ \mathrm{N/mm^2}$.

$$F_f = F_e + F_c + F_g - m\frac{d^2x}{dt^2} \qquad \text{7-15}$$

$$\frac{d^2x}{dt^2} = \frac{F_e + F_c + F_g + F_f}{m} \qquad \text{7-16}$$

The testing friction force is obtained from the test data indirectly using the measured piston motion and in-cylinder pressure as represented in Equation (7-15).

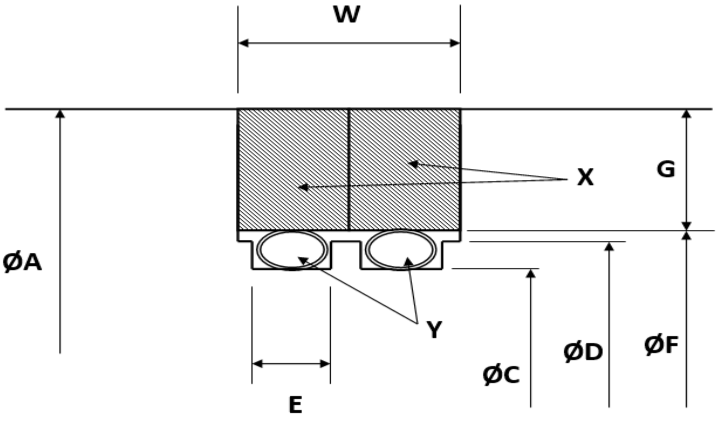

Figure 7-3. Schematic of piston seal.

Table 7-2. Prototype specifications and input parameters for model validation.

	Parameters [Unit]	Value
System	Moving mass [kg]	27.5
Expander	Maximum stroke [mm]	120.0
	Effective bore [mm]	80.0
	Inlet pressure [bar]	2.6
	Inlet temperature [K]	473.0
	Valve diameter [mm]	32.5
	Valve lift [mm]	8.13
Compressor	Maximum stroke [mm]	120.0
	Effective bore [mm]	70.0
	Inlet pressure [bar]	1.0
	Outlet pressure [bar]	2.7
Linear generator	Load constant of the generator [N/m·s^{-1}]	0

Table 7-3. Piston seal information.

X	2 Piston rings type	
Y	2 Canted springs	
	Expander(mm)	Compressor(mm)
Ring width W	10	8
Ring diameter A	80	70
C	64	54
D	68	60
E	3.2	3.2
F	70	61
G	6.0	4.5

Figure 7-4 shows the comparison between the observed data and the developed friction force model in Equation 7-8. The model results corresponded with the trends of the observed test data; the observed errors seen in the plot were propagated through the analysis from the noise on the in-cylinder pressure measurement.

The accuracy of the model was checked by comparing the measured and calculated piston dynamics properties. The acceleration profile of the LJEG is shown in Figure 7-5. The line shown as observed acceleration was calculated from the second derivative ($\frac{d^2x}{dt^2}$) of the measured piston displacement, while the line indicated as model acceleration was calculated from Equation (7-16). All other Equation (7-16) variables were measured directly from the experiment, but the frictional force was calculated from Equation (7-8). Comparisons were made between our model and other detailed reported models that could fit in LJEG friction analysis. The reported friction models were categorised into Cases 1 to 4, as presented in Table 7-4:

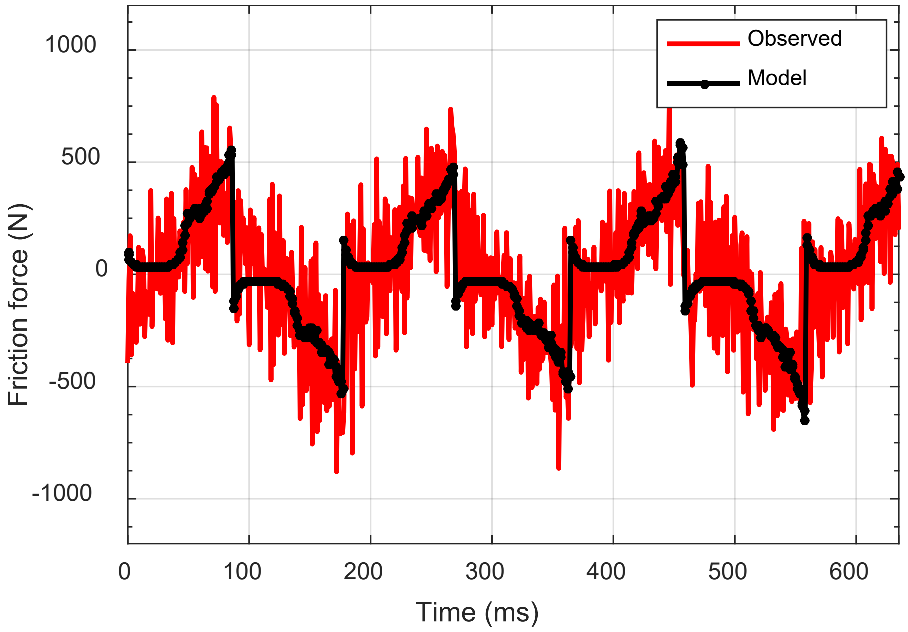

Figure 7-4. LJEG friction force profile (Test and model).

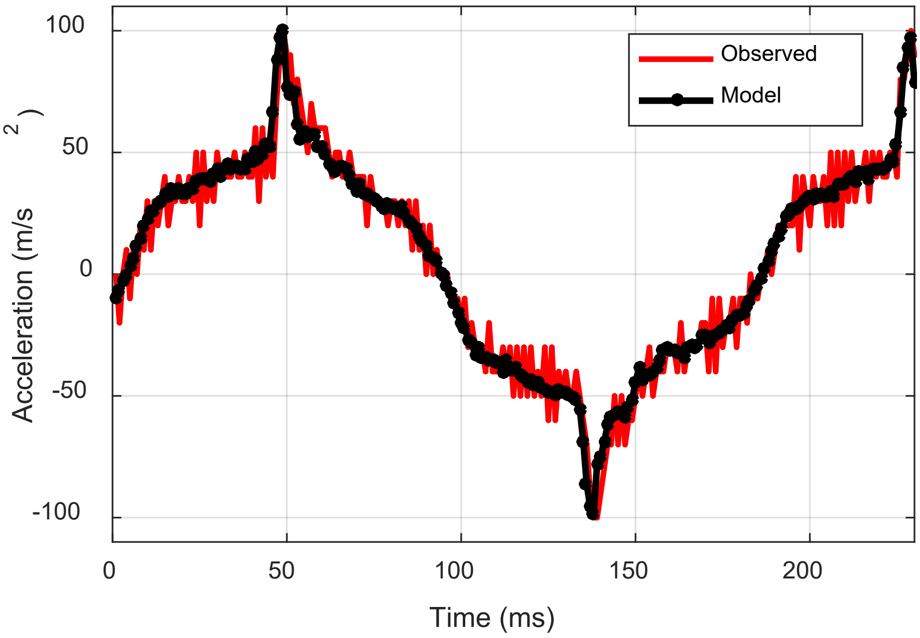

Figure 7-5. Piston acceleration profile.

The required experimental data for the comparison were imported to MATLAB, and all models (including models in Cases 1 to 4) were implemented in MATLAB/Simulink environment. The parameters for cases 1 to 4 were optimised. Figure 7-6 to Figure 7-8 show the acceleration, velocity and displacement for cases 1 to 4, the proposed model and the experiment data of the LJEG.

From the results comparison results shown so far, it is reasonable to conclude that the quest to develop a novel dry friction model is worth it, and the accuracy of the proposed model is sound. It would be an excellent addition to increase the accuracy of the whole (coupled) system model of the LJEG.

Table 7-4. Reported friction models applicable to LJEG operating on dry friction mechanism

S/N	Description	Value
Case 1 [168], [169] and [45]	This model considered the friction force to be a constant throughout the whole cycle.	Numerical constant (300**)
Case 2 [162], [163] and [164]	This friction model described friction force behaviour as a viscous force; it modelled the friction force as a force proportional to the sliding velocity while the direction of friction was opposite to the sign of piston velocity.	$F_{friction}(t) = -k\dot{x}(t)$ Where k represents a proportionality constant and $\dot{x}$; represented the instantaneous sliding velocity. (k = 250**)
Case 3 [165], [167] and [168]	This model described the frictional force of having both static and viscous friction force components.	$F_{friction}(t) = sign(\dot{x})[k_1 + k_2\lvert\dot{x}(t)\rvert]$ Where $\dot{x}$; the instantaneous sliding velocity k_2 is the kinetic friction coefficient related to the instantaneous velocity, and k_1; the static friction coefficient, which is considered as a constant part of frictional force. (k_1 = 230** and k_2 = 100**)
Case 4 [170]	The friction model consisted of three friction components; viscous friction, Coulomb friction and friction force because of in-cylinder pressure loading.	$F_{friction}(t) = C_f\dot{x} + f_d(T_r + \pi p D_p w_p)$ Where C_f represents damping coefficient, f_d dynamic friction coefficient, T_r is the diametral force, p is the in-cylinder pressure, w_p is the width of piston ring and D_p is the piston diameter. (C_f = 210** and f_d = 0.095**)

** Optimised parameters selected for simulation.

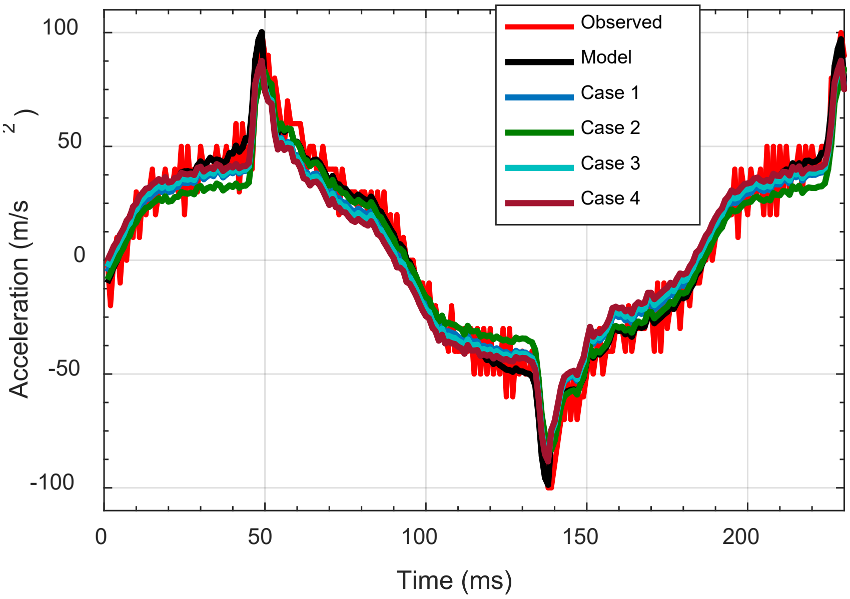

Figure 7-6. Piston acceleration profile for different cases

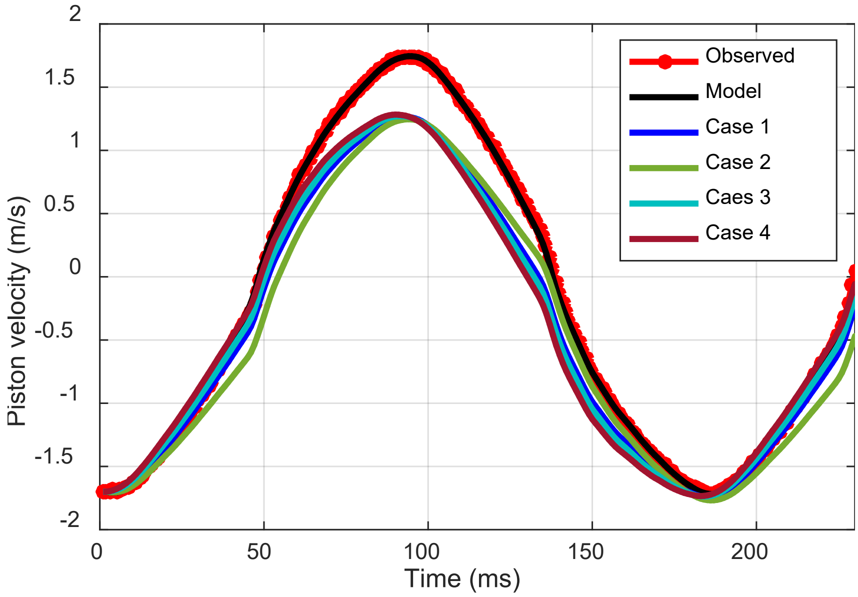

Figure 7-7. Piston velocity profile for different cases

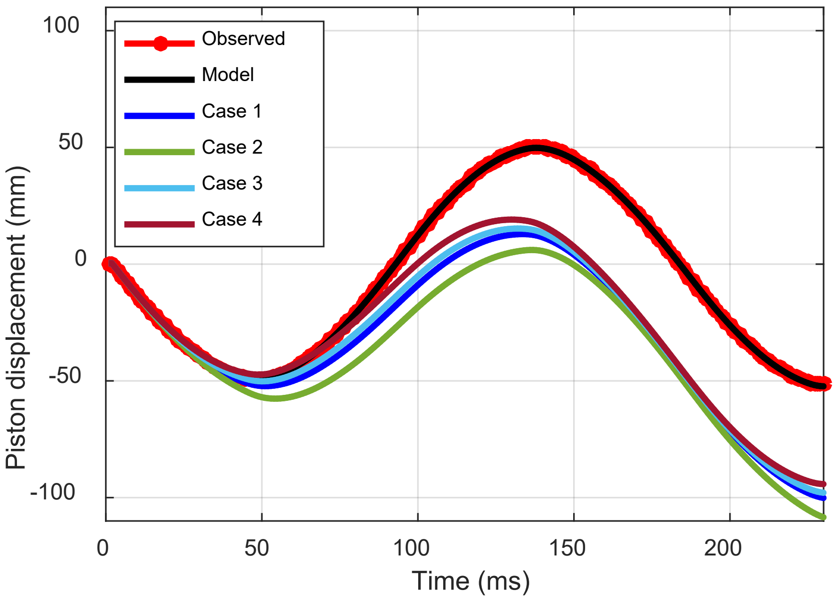

Figure 7-8. Piston displacement profile for different cases

Figure 7-9 and Table 7-5 explained a typical breakdown of the operation modes of the LJEG. Figure 7-10 demonstrates the piston velocity and trend of total friction force development across the LJEG. Point 1 indicates the start of expansion for the left expander, with the expander piston at OTDC position while the right compressor piston is at OBDC. Point 2 indicates inlet valve closure of the right compressor; therefore, technically, compression in the right compressor starts at “2”, while point 3 marks the close of the left expander inlet valve. At point 4, the right compressor exhaust valve opens; point 5 marks the end of compression and the OTDC for the right compressor and OBDC for the left compressor. However, compression from point “2” to point “5” although the compressor outlet valve opens at “4”. Processes between points 6 to 10 are the same as points 1 to 5 for the right expander and left compressor. Figure 7-11 shows the time history of piston velocity and friction force contribution due to dry contact friction of the piston ring and cylinder liner, while Figure 7-12 shows the time history of compressor pressure and friction force contribution due to pressure loading.

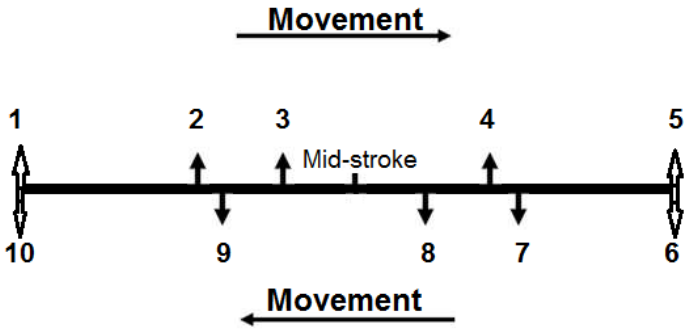

Figure 7-9. Illustration of expander and compressor operation in the LJEG

Table 7-5. Summary of expander and compressor operation in LJEG

Point 1	OTDC for the left expander: left expander intake valve opens. OBDC for the right compressor: right compressor intake valve opens.
Point 2	Right compressor intake valve closes; start of compression.
Point 3	Left expander intake valve closes.
Point 4	Right compressor exhaust valve opens.
Point 5	OBDC for the left expander. OTDC for the right compressor: right compressor exhaust valve closes.
Point 6	OTDC for the right expander: right expander intake valve opens. OBDC for the left compressor: left compressor intake valve opens.
Point 7	Left compressor intake valve closes; start of compression.
Point 8	Right expander intake valve closes.
Point 9	Left compressor exhaust valve opens.
Point 10	OBDC for the right expander. OTDC for the left compressor: left compressor exhaust valve closes.

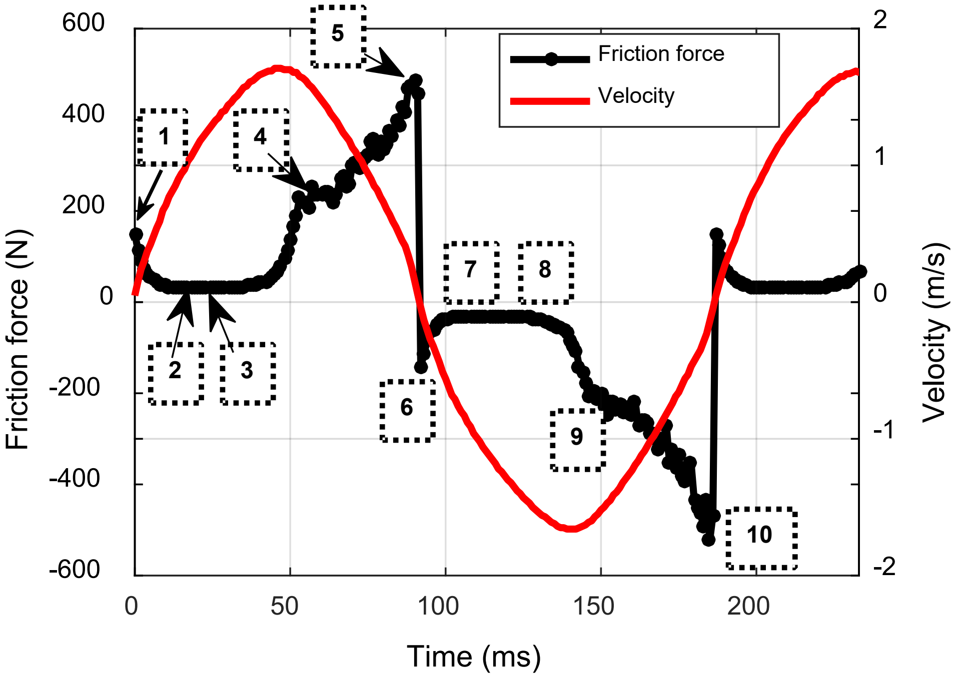

Figure 7-10. Total friction force and piston velocity profile

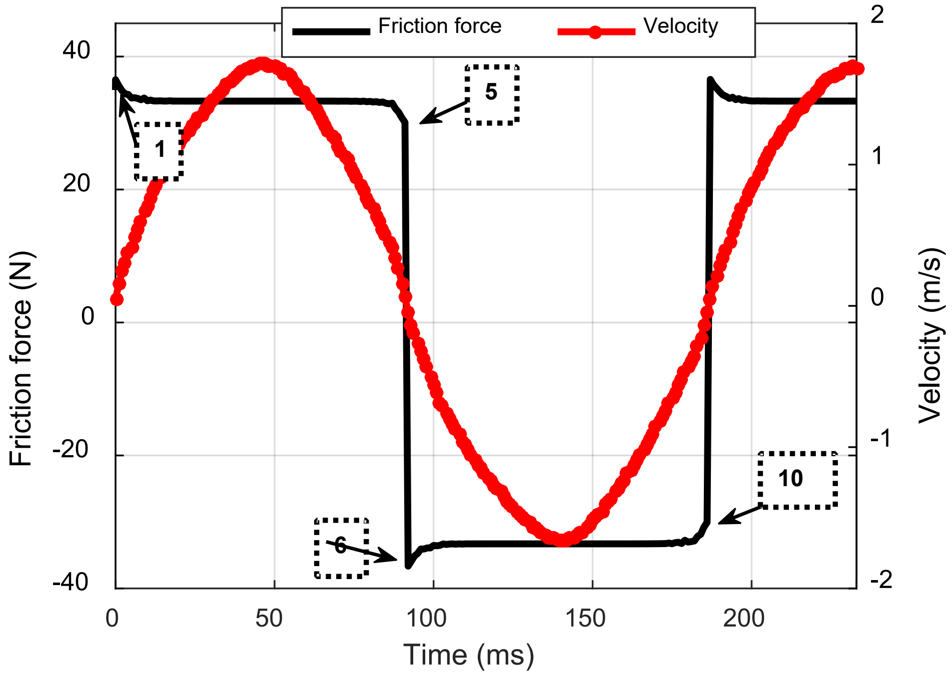

Figure 7-11. Dry contact friction force and velocity profile

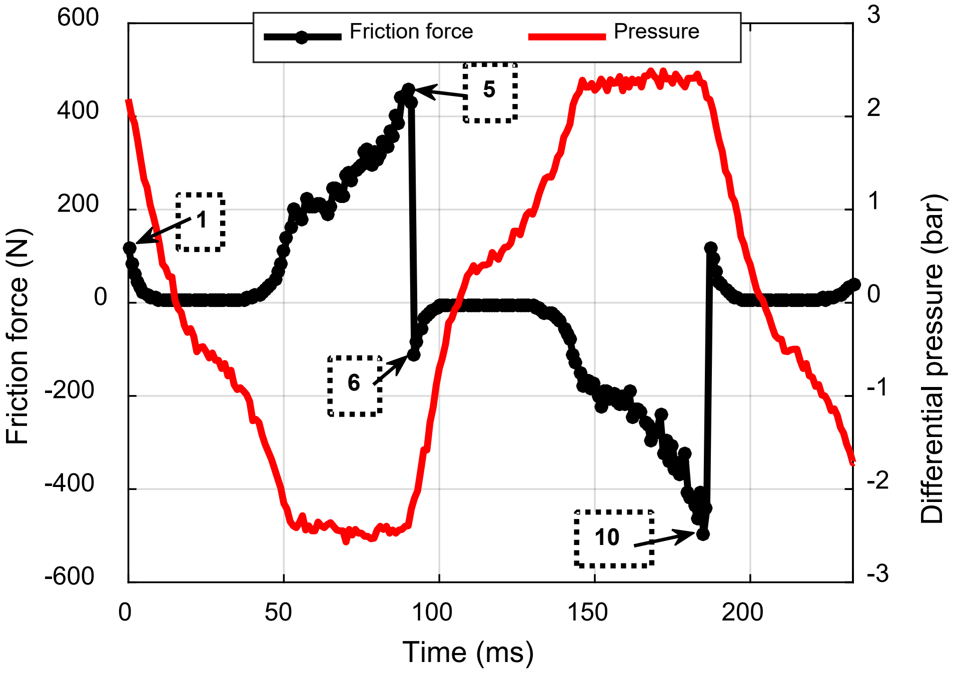

Figure 7-12. Pressure friction force and compressor pressure profile.

Figure 7-13 demonstrates the total friction force with the piston velocity, and Figure 7-14 shows the total friction force with the piston displacement. As it can be observed from Figure 7-10, Figure 7-13 and Figure 7-14 that the friction force is closely related to the compression process in the LJEG. The friction force topping range corresponded to the compression process in the LJEG (see Figure 7-10 and Figure 7-12). This observed behaviour implied that the friction during the compression process was more significant when compared with friction during the expansion process, and the friction tended to increase proportionally with the rise of the in-cylinder compression pressure. However, at the start of the expansion process (point 1), the friction force is higher than any other location (points 1 to 3) during an expansion (see Figure 7-10, Figure 7-13 and Figure 7-14); this observed effect was because of the higher stiction due to piston sticking at the OTDC/OBDC.

The friction force takes on a distinctly rising trend between “point 3” and point 4” (see Figure 7-10, Figure 7-13 and Figure 7-14), which corresponded to the region of higher piston velocity. It implied that within the region of higher piston velocity and the compressor outlet valve opening “4”, the increase in the friction force was due to the increase in compressor pressure rather than the effect of piston velocity (see Equation 7-13).

It could be observed that the compression process starts at point 2 and through points 4 to 5 (see Figure 7-10, Figure 7-13 and Figure 7-14). The compressor outlet valve opens at "point 4" and closes at "point 5"; therefore, technically, the pressure between "points 4" and "point 5" is the same, but the friction force is found to be increasing between the two points. The continuous increase in friction force at constant pressure (between "4" and "5") is attributed to a continuous decrease in piston velocity (see the exponential part of Equation 7-13) between the points and increase in pressure of air cushion at the expander, due to early closing of the expander exhaust valve.

Shortly after the start of expansion (after point 1, see Figure 7-14), the friction force is almost uniform until the start of compression (point 2). The dry friction component contributed more than 80% to the total friction before the start of compression. Between the start of compression (point 2) and the end of compression (point 5), friction due to the pressure loading contributed over 85% of the total friction force. Generally, the total friction of the LJEG increased continuously from the start of compression and attained the peak point at the end of compression. The total friction force changed its sign when the piston undertook its reverse stroke after OTDC and gradually reduced following the expansion process. Figure 7-15 shows the frictional power for a complete cycle of the LJEG.

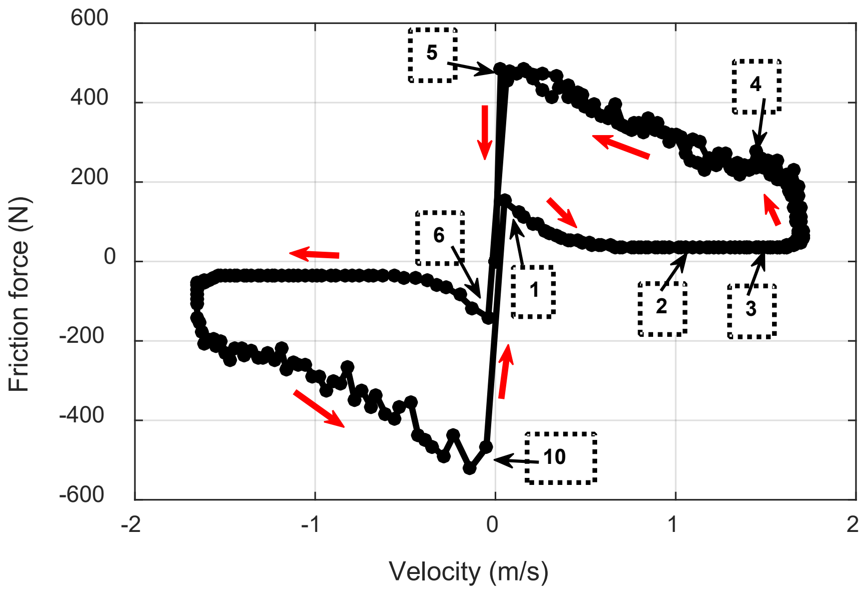

Figure 7-13. Total friction force and piston velocity

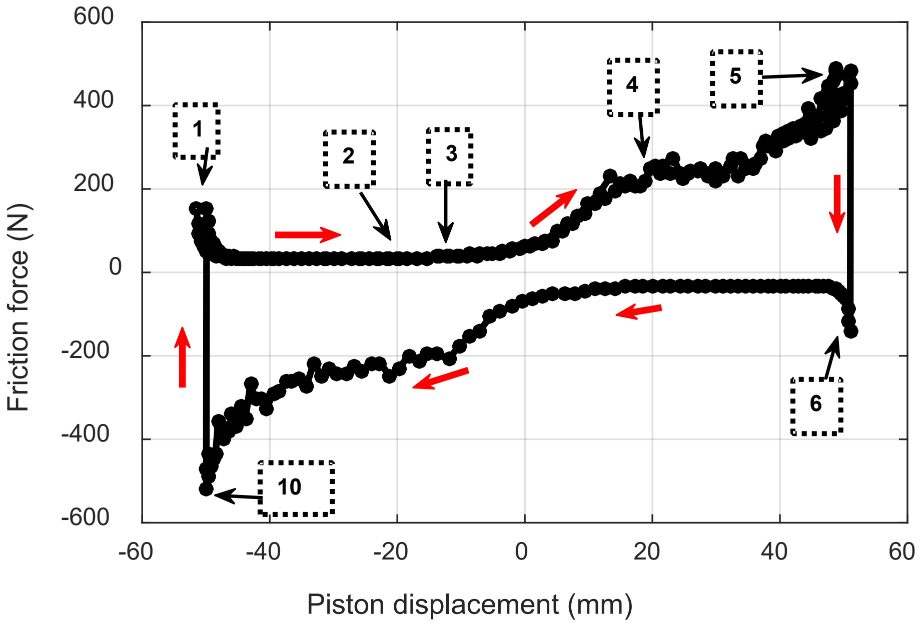

Figure 7-14. Total friction force and piston displacement

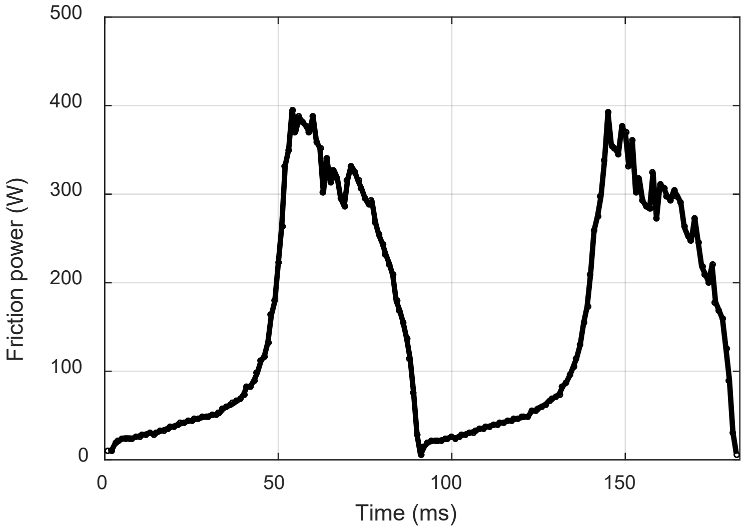

Figure 7-15. Total frictional power loss for complete cycle.

The coefficient of electric resistance force is among the influential parameters in the LJEG, and if it is optimised, it could increase the electricity generation efficiency. Figure 7-16 shows the mean friction power at different generator load conditions while keeping all other parameters constant. The operating condition is the same in Table 7-2 but with changes in operating pressure and temperature, as shown in Table 7-6. It could be seen from Figure 7-16 that the mean friction power varied inversely to the generator load when other parameters are kept constant. An increase in generator load means an increase in electromagnetic load resistance, resulting in decreased piston amplitude and mean velocity. The relationship between generator load and friction power implied that a higher electric resistance load would lower the friction force, improving overall system efficiency.

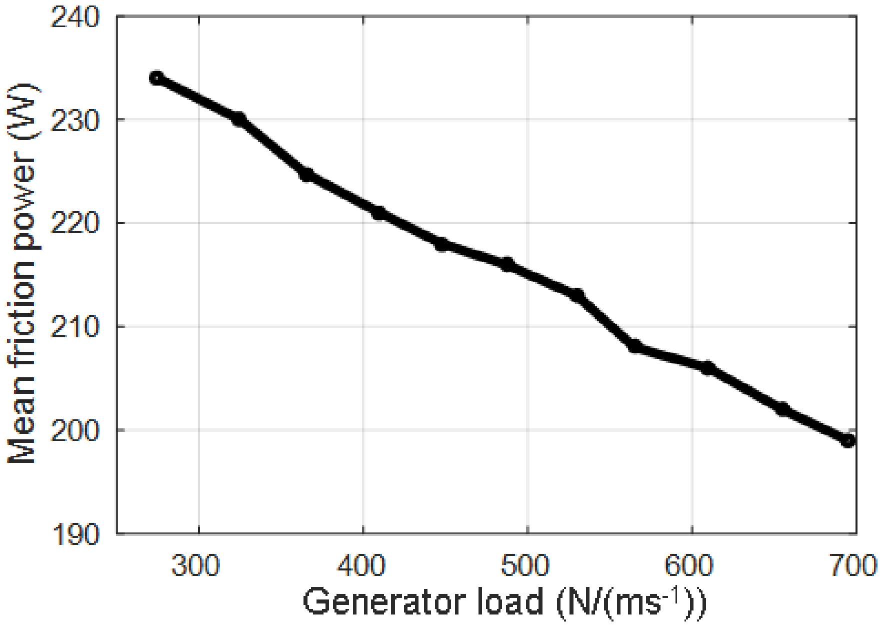

Figure 7-16. Mean friction power at different generator load.

Table 7-6. Additional input parameters for mean friction power simulation.

	Parameters [Unit]	Value
Linear expander	Inlet pressure [bar]	7
	Inlet temperature [K]	1100
Linear compressor	Outlet pressure [bar]	7
	Inlet temperature [K]	300
	Outlet temperature [K]	473.0
Linear generator	Load [Nm/s]	Variable

7.5 Conclusions

In this chapter, a novel friction model of an LJEG system is presented, and the proposed model is validated against experimentally observed test data. However, the model accounted for macroscopic sliding alone. The main advantage of the proposed model was its simplicity and accuracy for numerical simulations. The main conclusions from this chapter are listed below:

1. The frictional force of LJEG can is represented as a combination of a dry friction model of a mass-spring-damper mechanical system and friction force due to compression pressure. During the compression process, the mean friction force was about 500% of the mean friction during the expansion process; therefore, pressure build-up in the LJEG compressor contributed a significant part of the total friction force developed.

2. Aside from the surface characteristics of the piston ring and cylinder liner interface, the system pressure, piston velocity, and piston acceleration were the main parameters defining the friction characteristics of the Linear Joule Engine Generator.

3. Up to 15.3% of the expander indicated work could be dissipated through friction for low pressure (less than 3 bar) and low acceleration operation.

4. The relationship between generator load and friction power indicated that higher electric resistance force would lower friction force, which improved the overall system efficiency.

Chapter 8: Parametric analysis and system optimisation

8.1 Coupled system model simulation results

The simulation results for the semi-closed cycle argon-oxy-hydrogen LJEG at design conditions are presented in this chapter. The simulation input parameters are as presented in Table 8-1. Variations in compressor/expander diameter ratios, temperatures, generator loads, and expander inlet and exhaust valve timing are considered in the simulation to reveal the relationships with performance indicators. This parametric evaluation would lead to the optimisation of the proposed LJEG. Some of the contents of this chapter have been published by the author in [22].

8.2 Expander and compressor diameter ratio and valve timing

The influence of the ratio of the compressor and the expander diameter was investigated for different expander intake and exhaust valve timing. The valves were assumed to be wholly open/close according to the open/close command in the Stateflow function in the simulation model. The valve response time was the same for the valve open and close command in this study. The piston displacement and velocity were the controlled loop feedback signals for valve timing adjustment. The illustration of intake valve timing of the left expander is shown Figure 8-1, the intake valve open command of the left expander was triggered when the piston reached its operating top dead centre (OTDC), and the piston velocity was zero. The intake valve closed before or precisely at the mid-stroke. Six different intake valve timings were investigated, including Expander Intake Valve Closing (EIVC) at 25 mm, 20 mm, 15 mm, 10 mm, and 5 mm before the mid-stroke, and mid-stroke (0 mm before). The exhaust valve timing for the right expander is illustrated in Figure 8-2. The exhaust valve open command for the right expander was initiated when the piston reached its operating bottom dead centre (OBDC), which was the OTDC for the left expander. The confusion on the interchanging nature of OBDC and OTDC of the left and right expander in operation was eliminated by adopting the OTDC and OBDC of the left expander as the convention for this study. Three different expander exhaust timing operations were analysed and investigated: Expander Exhaust Valve Closing (EEVC) at 20 mm and 30 mm away from the mid-stroke and at exact OBDC.

Table 8-1. Base case input parameters

	Parameters [Unit]	Value
	Moving mass [kg]	8.0
Linear expander	Maximum stroke [mm]	118
	Effective bore [mm]	85
	Inlet pressure [bar]	7.0
	Inlet temperature [K]	1070
	EIVO [mm]	TDC
	EIVC [mm]	20
	EEVO [mm]	BDC
	EEVC [mm]	TDC
Linear compressor	Effective bore [mm]	70
	Inlet pressure [bar]	1.0
	Outlet pressure [bar]	7.0
	CIVO [mm]	BDC
	CIVC [mm]	TDC
Reactor	Inlet pressure [bar]	7.0
	Inlet temperature [K]	420

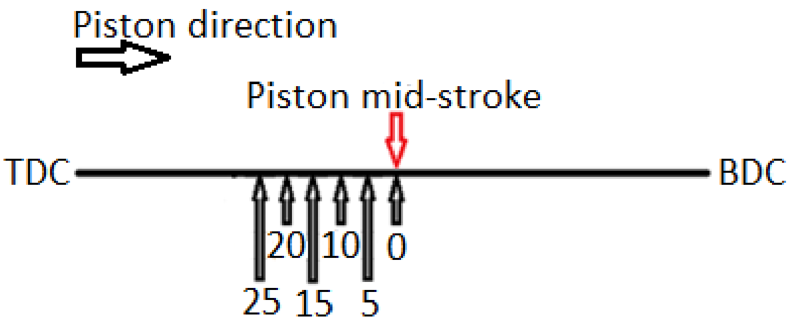

Figure 8-1. Illustration of the left expander intake valve timing.

.

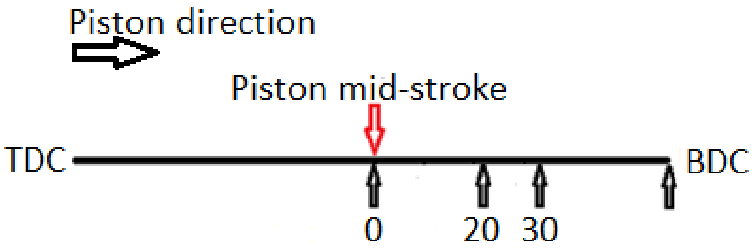

Figure 8-2. Illustration of the right expander exhaust valve timing.

The compressor/expander ratio (CER) was the ratio of the diameter of the compressor to the diameter of the expander. The electric power output and system efficiency versus compressor/expander ratio (CER) are shown in Figure 8-3, Figure 8-4 and Figure 8-5, with the exhaust valve closing at; 20 mm after the mid-stroke, 30 mm after the mid-stroke and at the mid-stroke, respectively. The Figures were generated using the input parameters stated in Table 8-1.

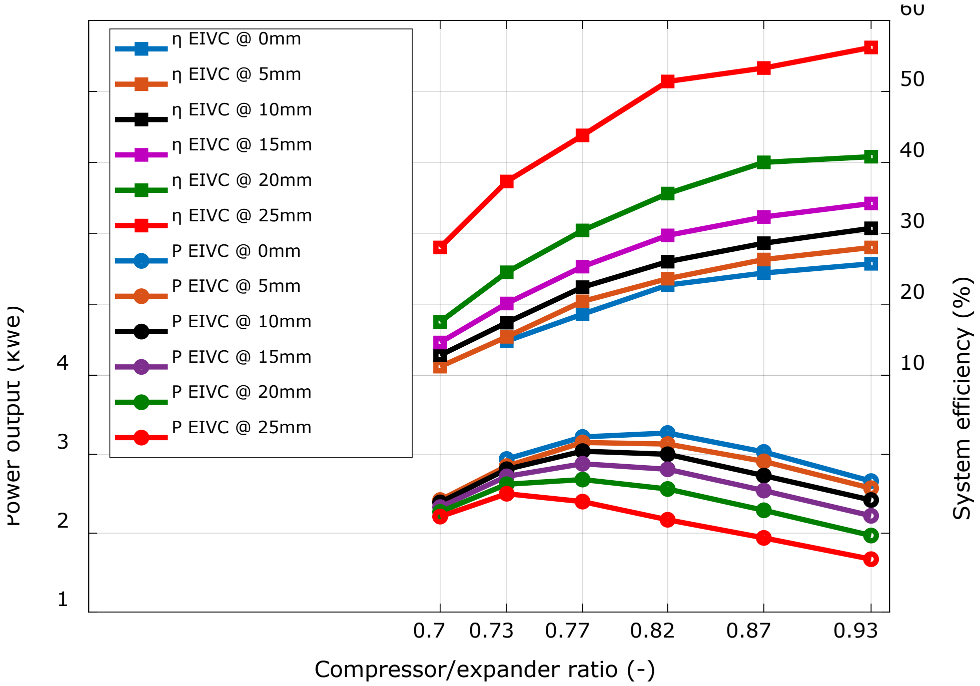

Figure 8-3. Power output and efficiency, when the exhaust valve closes at 20 mm after mid-stroke.

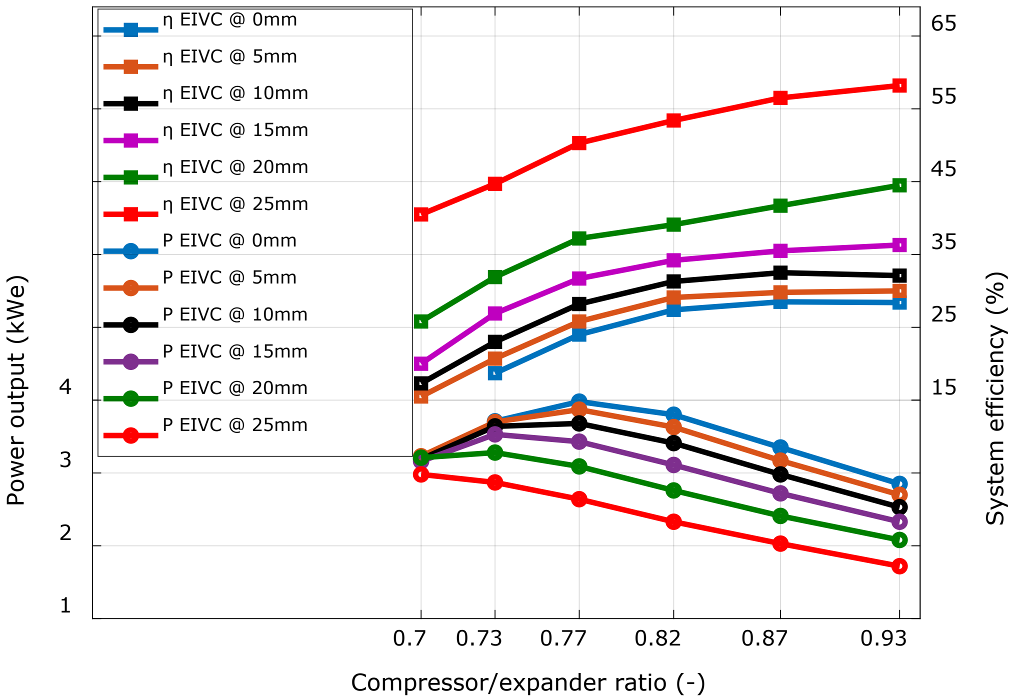

Figure 8-4. Power output and efficiency, when the exhaust valve closes at 30 mm after mid-stroke.

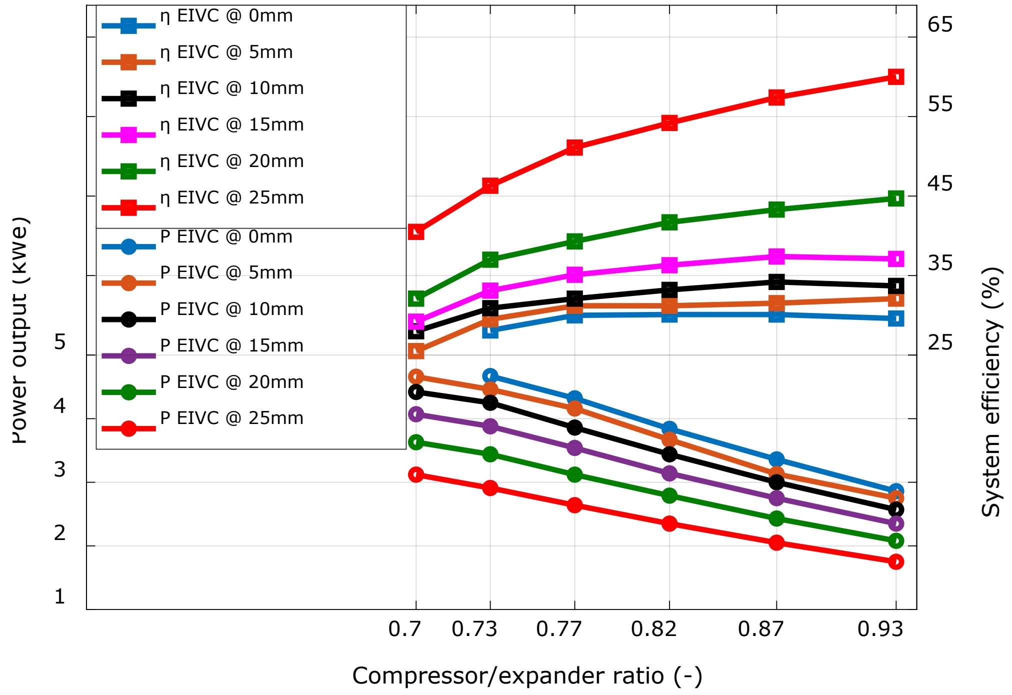

Figure 8-5. Power output and efficiency, when the exhaust valve closes at OBDC.

The relationship between the specific power and system efficiency at different engine conditions are shown in Figure 8-6, Figure 8-7, and Figure 8-8, with the exhaust valve closing at; 20 mm after mid-stroke, 30 mm after mid-stroke and at mid-stroke, respectively. It is evident from Figure 8-6 to Figure 8-8 that the specific power increased with system efficiency, and as well, the two parameters have a similar trend in all cases; therefore, more consideration is given to system efficiency and power output rather than specific power consequently in this study.

Figure 8-3 to Figure 8-8 show the operational CER range and the possible expander inlet valve-timing window of the LJEG. Beyond this geometric and expander inlet timing range, the LJEG system efficiency deteriorated abruptly, or the operational stability was highly undermined, or both the former and latter occur. Notwithstanding, the severity of operating the LJEG beyond these ranges depended on other operational parameters like exhaust valve timing and electric load.

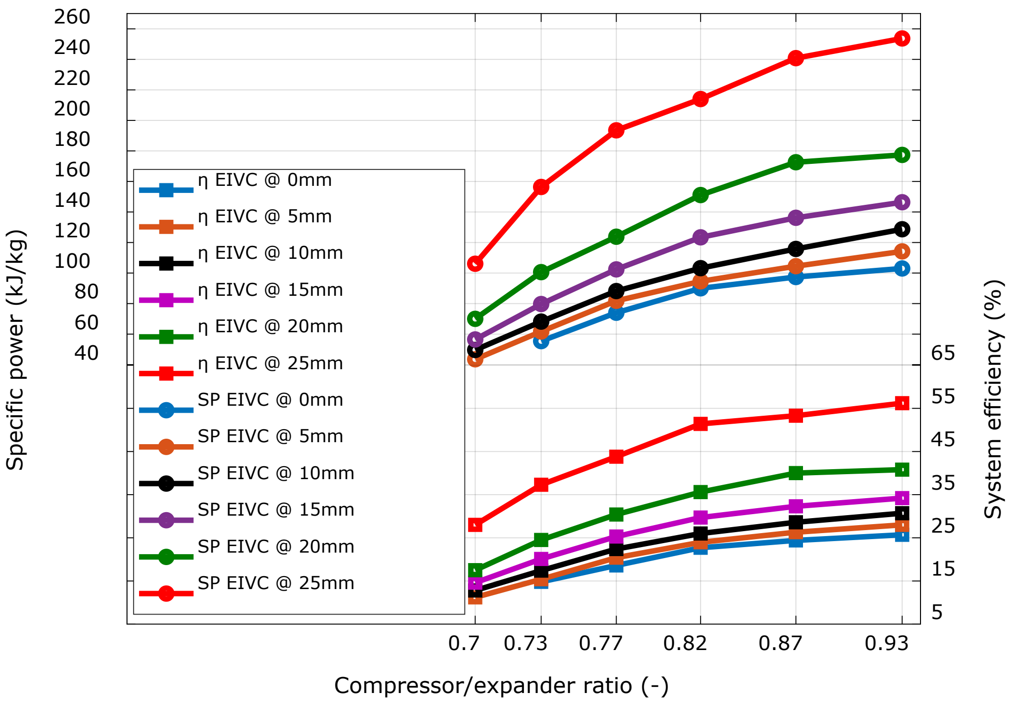

Figure 8-6. Specific power and efficiency, when the exhaust valve closes at 20 mm after mid-stroke.

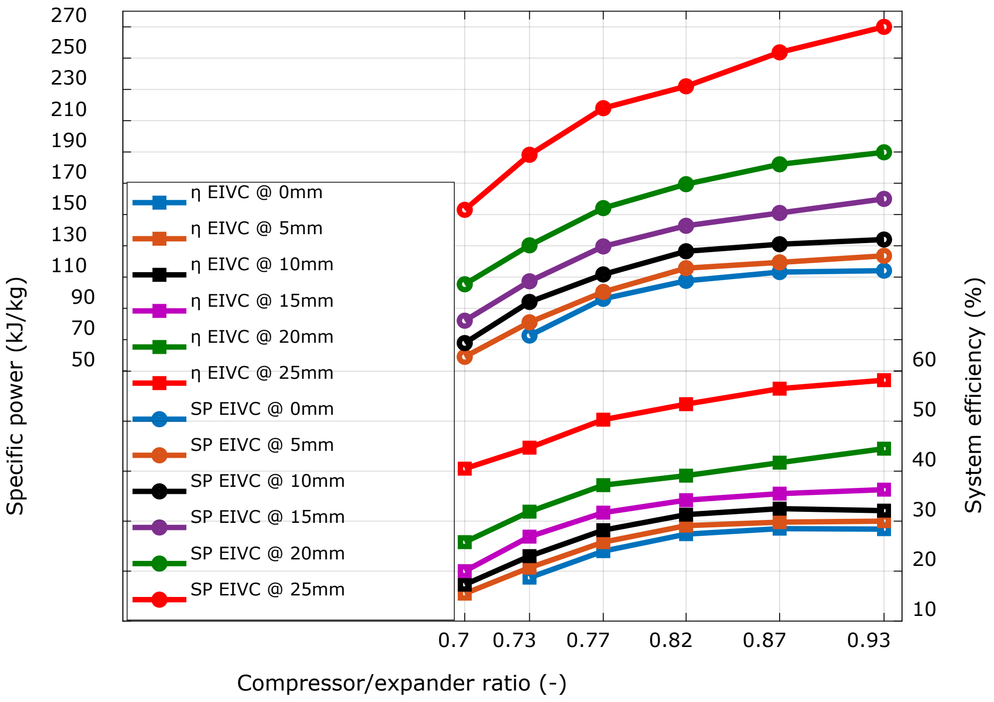

Figure 8-7. Specific power and efficiency, when the exhaust valve closes at 30 mm after mid-stroke.

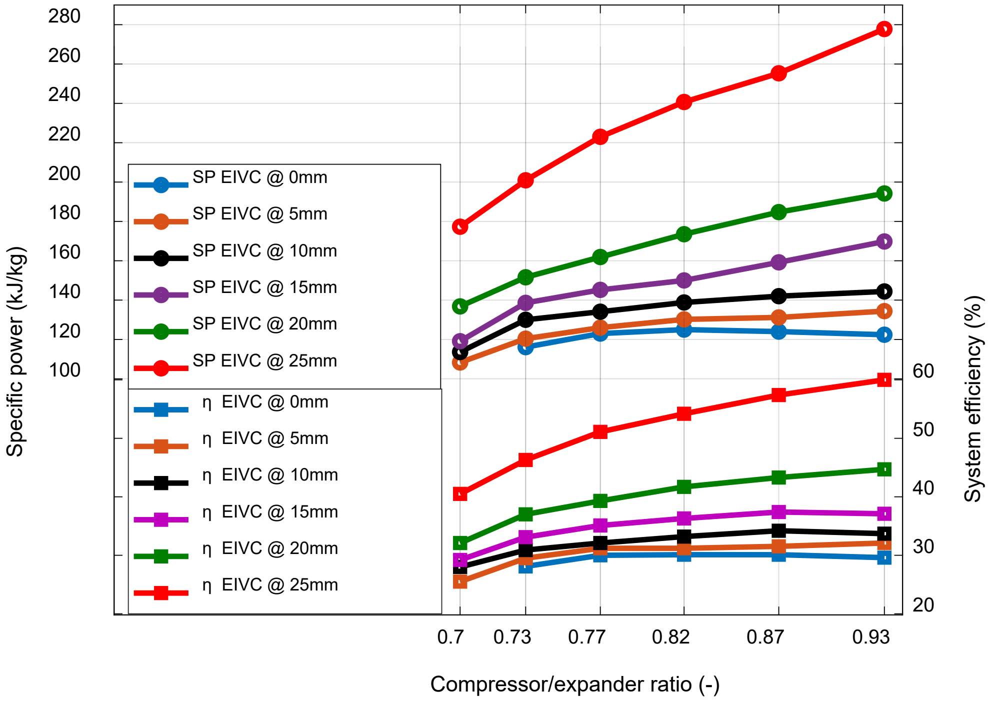

Figure 8-8. Specific power and efficiency, when the exhaust valve closes at mid-stroke.

8.2.1 Influence of EIVC

The expander valve timing was one of the essential operational parameters that influenced the performance indicators in an LJEG. The impact of expander inlet timing is shown in Figure 8-3 to Figure 8-5. It is observed that lower values of system efficiencies were prevailing at a longer intake duration (e.g. EIVC at 0 mm and 5 mm before the mid-stroke), and power output generally increased with extended expander intake duration. It is evident from Figure 8-3 to Figure 8-5 that the system efficiency increased with a shorter intake duration. Part of the reason for this was that the end pressure of the expansion process was still relatively high if a prolonged intake valve duration was applied. Perhaps, this indicated that the geometry constraint of the cylinder would not allow the expansion process to be fully conducted if the intake gas mass was too high. Figure 8-9 demonstrates that with a longer intake duration (e.g. EIVC 5 mm before the mid-stroke), the working fluid energy utilisation level at the end of expansion was relatively lower than that of shorter intake durations (e.g. EIVC 15 mm and 25 mm before the mid-stroke). Furthermore, with an extended intake duration, a longer piston stroke was achieved (Figure 8-10 to Figure 8-12), and energy dissipated through friction was higher. This friction loss contributed to declining system efficiency at extended EIVC.

The expander intake valve closing at 25 mm before the mid-stroke was the minimum valve opening duration that an LJEG could operate stably with the input parameters stated in Table 8-1. It also corresponded to the optimal system efficiency of an LJEG regardless of CER or expander exhaust duration adopted. The ability of the LJEG to recover from any disturbance was considerably lower at short intake duration and was more robust at extended or longer intake duration.

At the CER of 0.736 or less, the expander intake duration could not extend beyond 5 mm before the mid-stroke. This was because the compressor capacity at CER of 0.736 or less could not supply the fluid needed to sustain the expander intake duration beyond the 5 mm mark before the mid-stroke. Therefore, the limit of expander intake duration was dependent on the CER choice of the LJEG.

8.2.2 Influence of EEVC

There was an overall power output and system efficiency improvement made by extending the exhaust valve timing from 20 mm post-mid-stroke to BDC (as evident in Figure 8-3 to Figure 8-5). Earlier closure of the expander exhaust led to a decline in the LJEG performance. This drop in performance was because part of the working fluid energy in the active expander was used to compress the trapped exhaust gas in the opposite expander clearance after the expansion process. Consequently, adapting the expander exhaust to close at BDC supported both higher system efficiency and power output compared to the cases when the expander exhaust valve closed before the BDC. It was clear that the later the EEVC before the BDC, the better was the LJEG performance. However, in practice, there needed to be a trade-off between better system performance and control ability of late EEVC. Earlier EEVC might improve the controllability of the LJEG, and implementing later EEVC control might pose some challenges.

8.2.3 Influence of CER

The CER (geometric variable) influence on the performance indicators of LJEG is presented in Figure 8-3 to Figure 8-5. System efficiency improved with an increase in the CER; this was partly because the end pressure of the expansion process was relatively lower with elevated CER compared with the end pressure of the expansion process at lower CER. Similarly, less energy was spent on piston friction due to decreased expander piston perimeter with high CER values. Additionally, piston strokes were shorter with increased CER (see Figure 8-10 to Figure 8-12); typically, less energy was lost through friction per cycle for shorter piston strokes.

The power output and the CER relationship depended on the expander exhaust timing adopted (EEVC). When the expander exhaust valve closed at BDC, as seen in Figure 8-5, the power output and the CER had a linear relationship with a negative gradient for all expander intake timing. If the expander exhaust valve closed at 20mm after mid-stroke as presented in Figure 8-3, the power output and CER relationship was a curve with varying maxima, and the maxima existed between 0.736 and 0.823 CER. The location of the maxima was dependent on the expander intake duration. The location of the curve maxima on the independent axis tended to shift from 0.736 towards 0.823 CER with increased expander intake duration. The power output relationship with the CER in Figure 8-4 combined the two scenarios presented in Figure 8-3 and Figure 8-5. It suggested that if the expander exhaust valve closed before BDC, the power output trend was dependent on both the expander intake and exhaust timing adopted. Therefore, the location of peak power is dependent on the expander exhaust timing adopted. When the exhaust valve closes at BDC, the peak power was located at the least CER. The more advanced the expander exhaust valve closed before the BDC; the peak power location moved towards elevated CER. This implies that recompression in the expander adversely affected the power output further towards low CER. The adverse impact of recompression is proportional to recompression duration and as well as the expander intake duration; these could be seen in Figure 8-3 and Figure 8-4. That is the reason the location of the peak power moved towards elevated CER with extended intake duration.

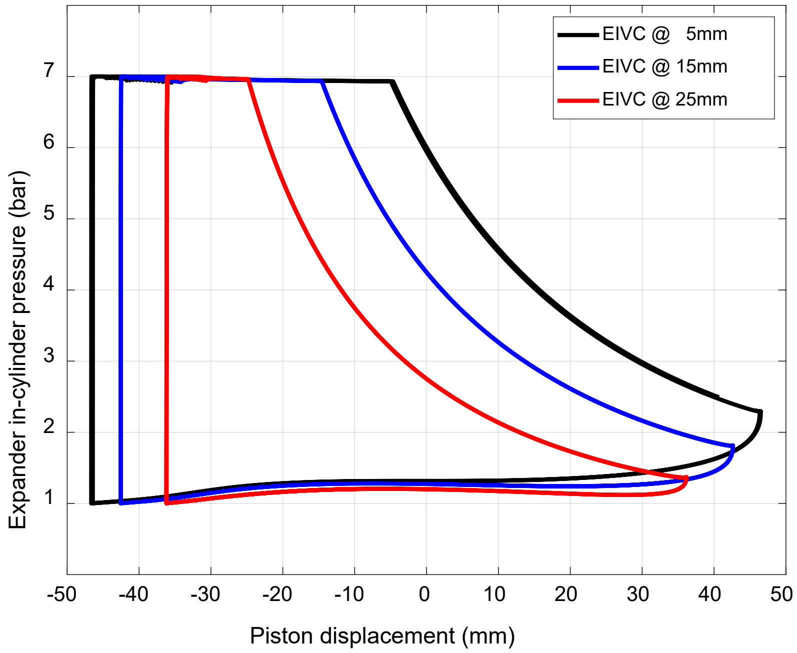

Figure 8-9. Expander in-cylinder pressure with EIVC at 5 mm, 15 mm and 25 mm, EEVC at BDC, and CER of 0.823.

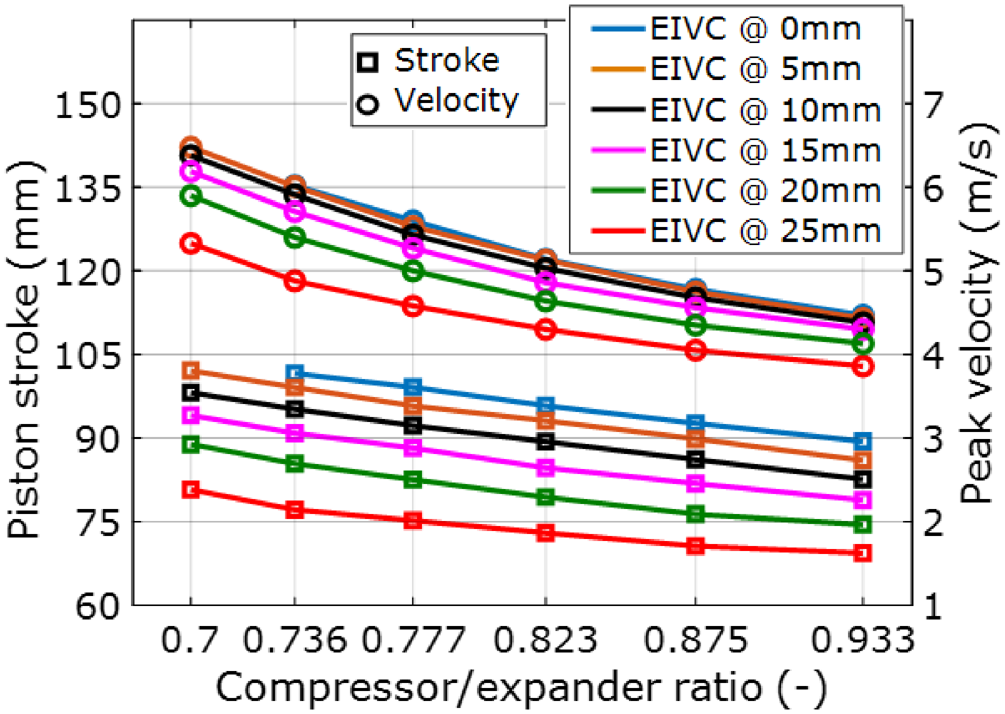

Figure 8-10. Piston stroke and peak velocity when the EEVC at 20 mm after mid-stroke.

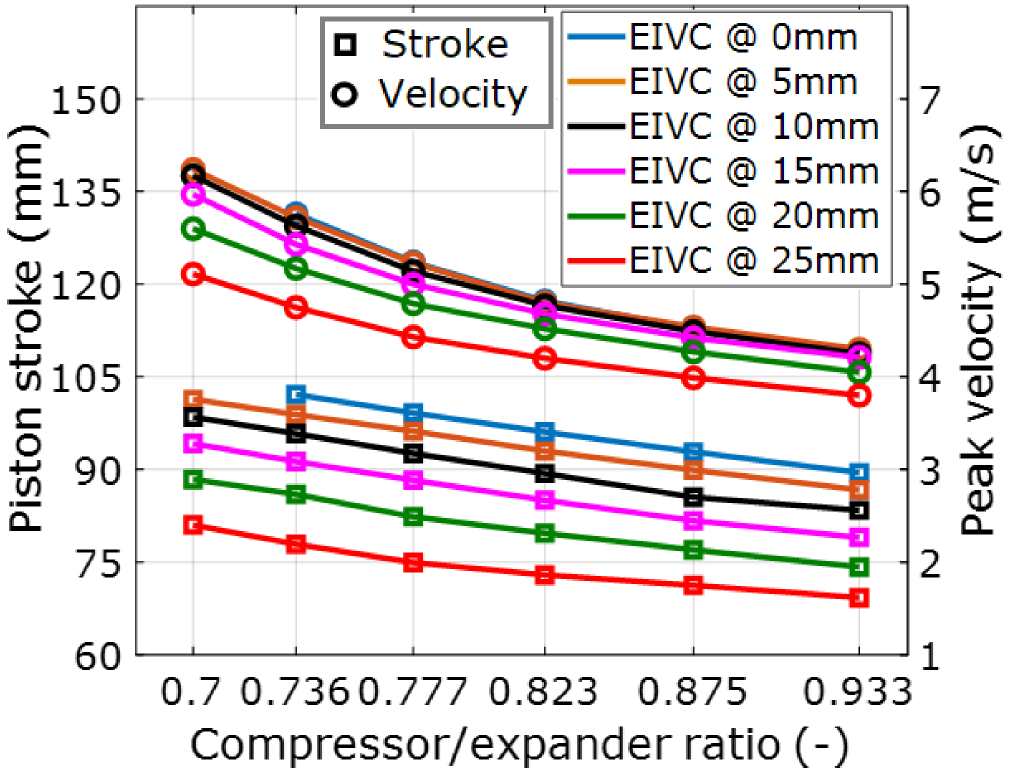

Figure 8-11. Piston stroke and peak velocity when the EEVC at 30 mm after mid-stroke.

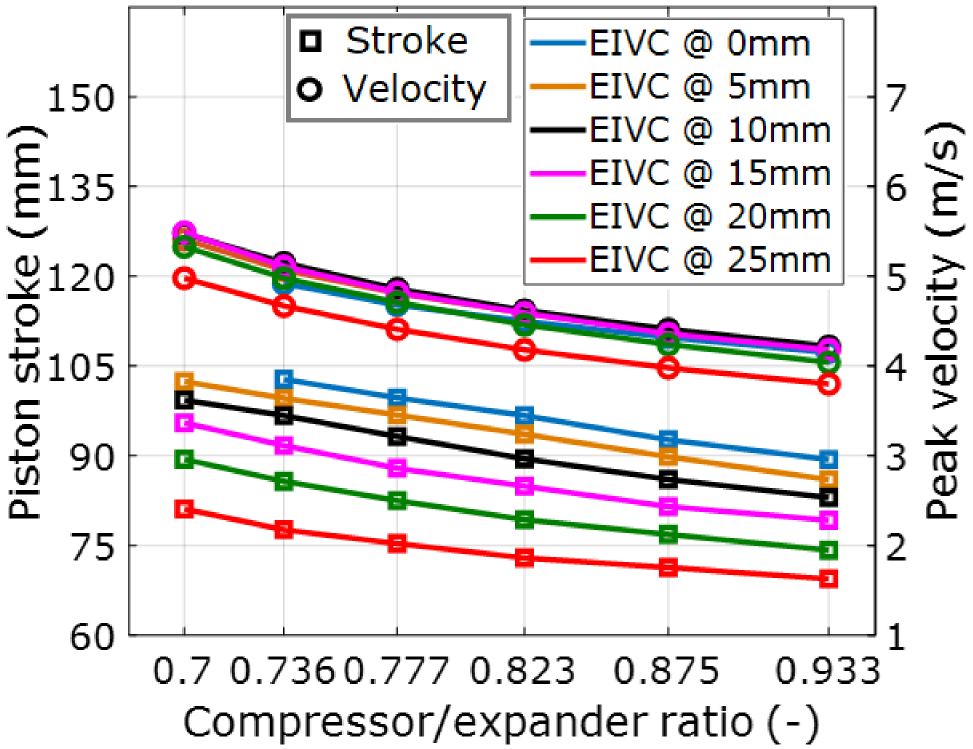

Figure 8-12. Piston stroke and peak velocity when the EEVC at BDC.

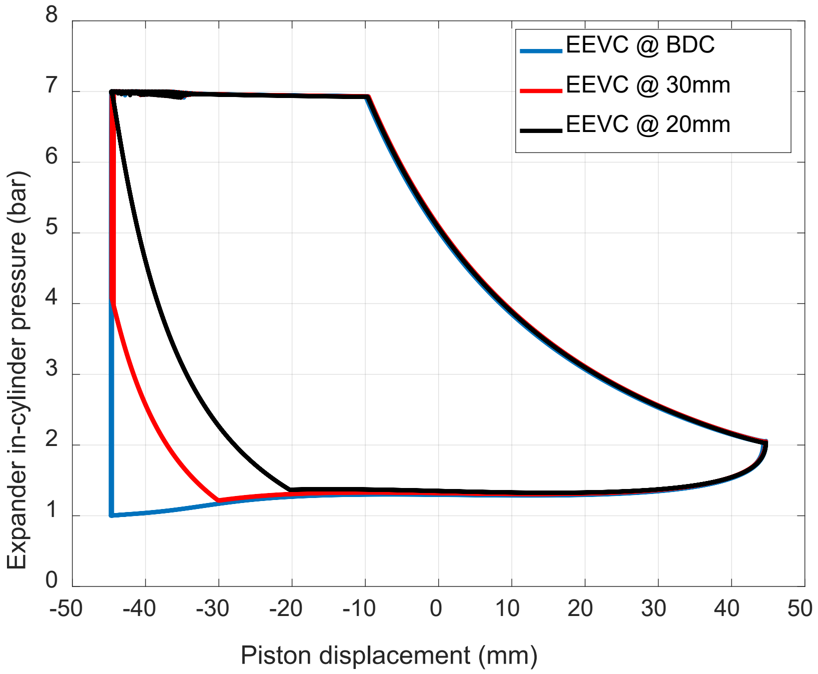

Figure 8-13. Expander in-cylinder pressure with EIVC at 10 mm, EEVC at BDC, 30 mm and 20 mm, CER 0.823.

8.3 Generator load

The system performance of an LJEG was dependent on the generator load constant, and the load constant was recommended to be limited to an acceptable range to avoid unstable operation. Within this range, it was suggested that the load constant of the generator could be maximised to improve electricity generation efficiency [20].

A generator load constant sweeping was conducted to achieve optimal system efficiency while other parameters remain unchanged. The maximum design value for the generator load constant was 207.3 ($N/m\cdot s^{-1}$), and the values of the load constant of the generator simulated were the coefficients of the maximum design value (see Equation 8-1).

$$\mathrm{G} = kG_{max} \tag{8-1}$$

Where k represents the generator load coefficient (GLC) and $1 \geq k > 0,\ G_{max}$ represents the maximum design value of the generator load constant.

The generator load coefficient (GLC) at the optimal system efficiency and the corresponding power output at various intake and exhaust valve timings and different CERs are presented in Figure 8-14 to Figure 8-19. The results showed that there was an optimal value of generator load constant for every valid combination of the input parameters for optimum system performance. There was a complicated relationship between generator load coefficient, power output, expander intake and exhaust duration, and CER. This was caused by different levels of recompression impact on power output due to varying CER and intake duration. At low CER (0.70 - 0.73) and EEVC before the OBDC (Figure 8-14 and Figure 8-15), (GLC) decreased slightly with a longer intake duration, while power output increased simultaneously. At CER of 0.77 and EEVC before the OBDC (Figure 8-16), the GLC appeared constant across different intake duration while the power output increased with a longer intake duration. With high CER above 0.823 and EEVC before the OBDC (Figure 8-17 to Figure 8-19), GLC increased linearly with extended intake duration while power output also increased with extended intake duration. Generator load coefficient and power output increased with longer intake duration irrespective of CER, provided the exhaust valve closed at OBDC.

The results in Figure 8-14 to Figure 8-19 indicate that if an EEVC at OBDC was adopted, the GLC appeared to stay high at lower CER, and GLC was found to decrease with increased CER. Conversely, it was evident in Figure 8-14 to Figure 8-19 that if the EEVC before OBDC valve timing was adopted, the generator load coefficient was low at lower CER but increased with rising CER. Perhaps an insight into the load influence on different operating conditions was imperative for the optimal performance evaluation of the LJEG. Therefore, the generator load coefficient searching for various combinations of geometric and operational parameters would estimate the capacity and power density of LJEG with a specific configuration and operational strategy. This, in turn, would guide the design of a linear alternator.

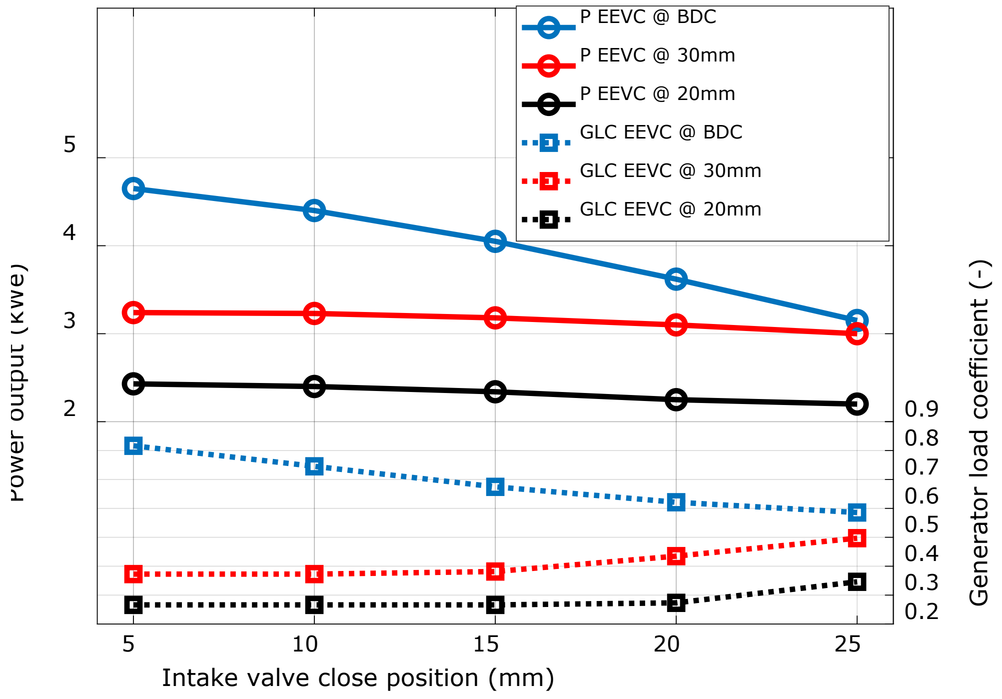

Figure 8-14. Coefficient of generator load constant and system power output at 0.7 CER.

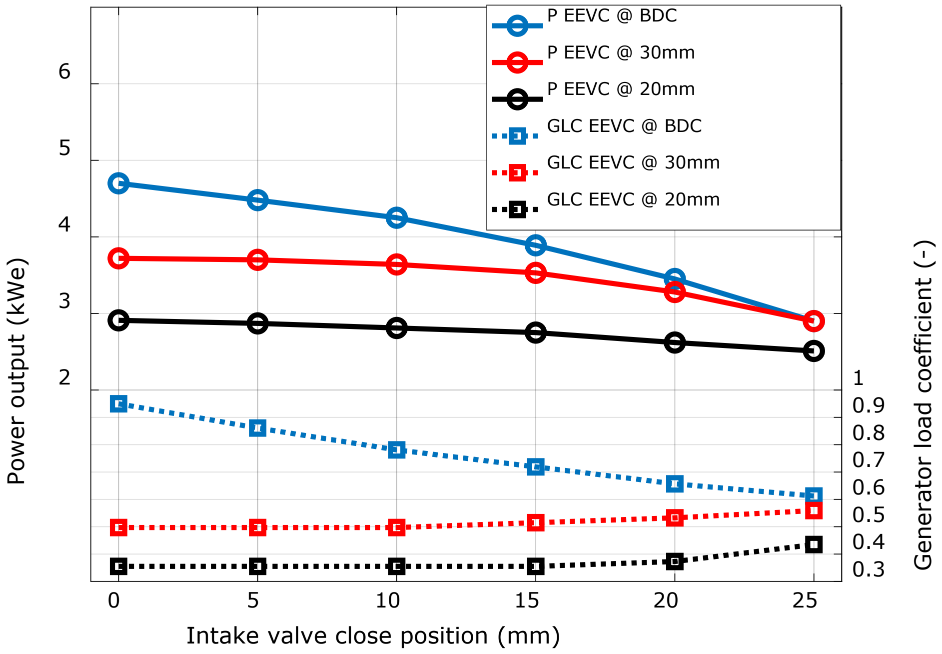

Figure 8-15. Coefficient of generator load constant and system power output at 0.736 CER.

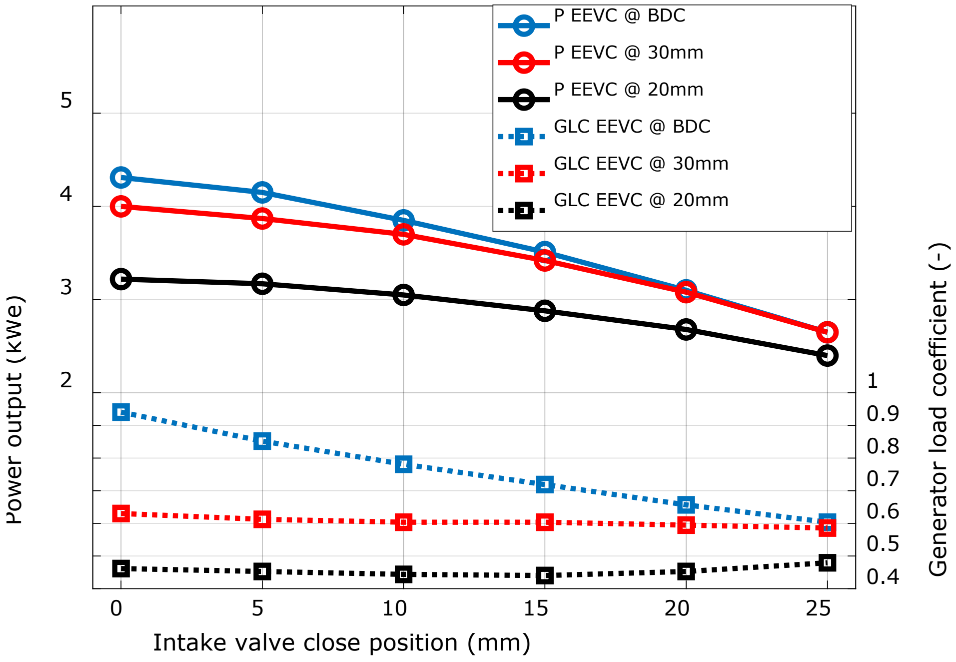

Figure 8-16. Coefficient of generator load constant and system power output at 0.77 CER.

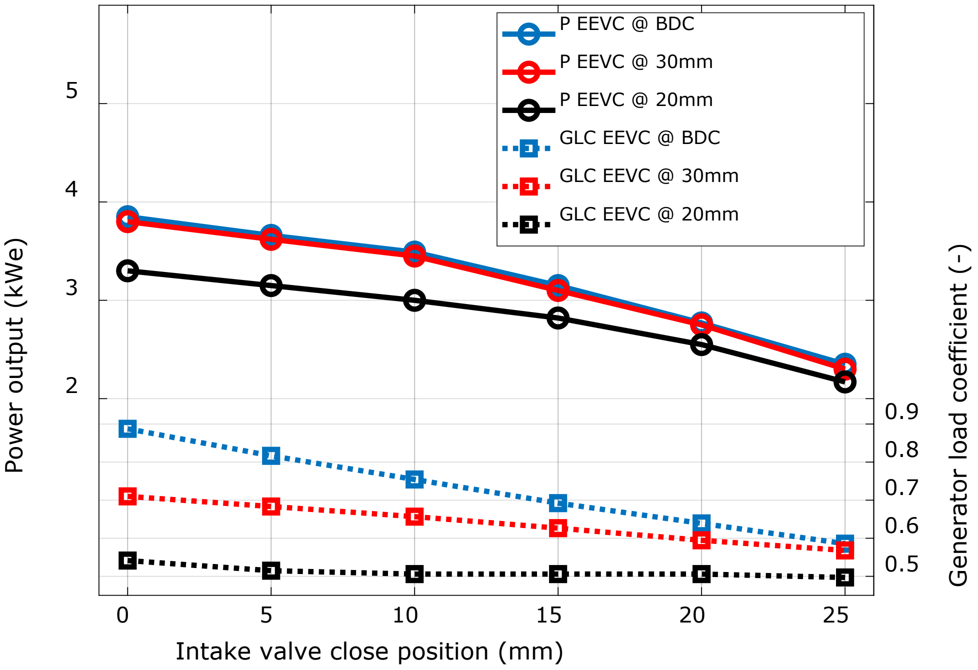

Figure 8-17. Coefficient of generator load constant and system power output at 0.823 CER.

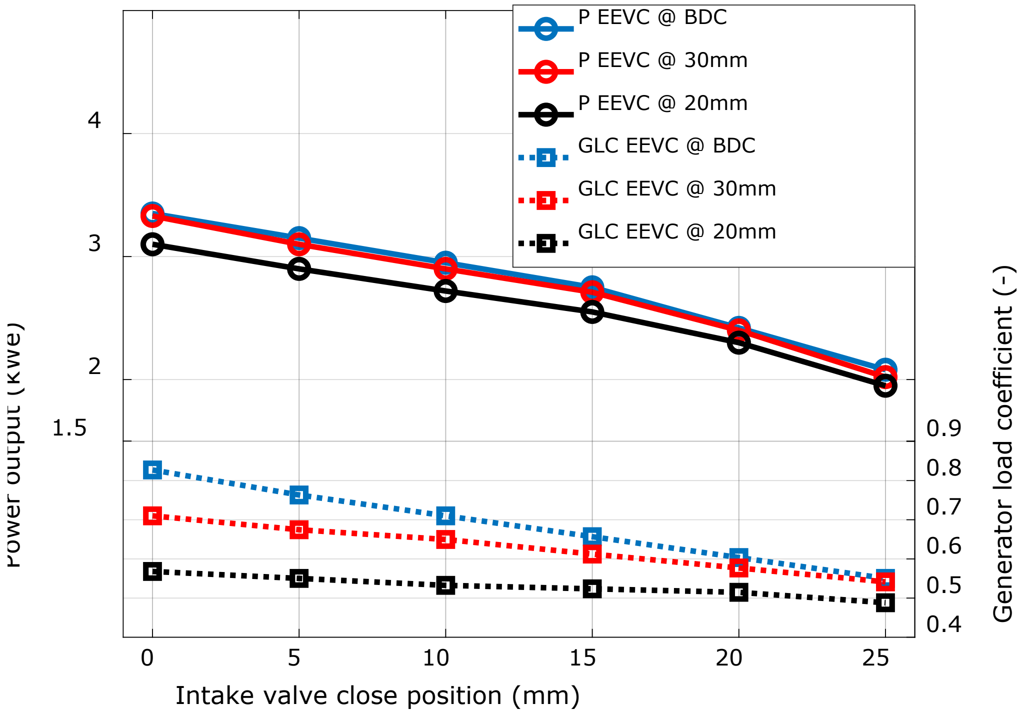

Figure 8-18. Coefficient of generator load constant and system power output at 0.875 CER.

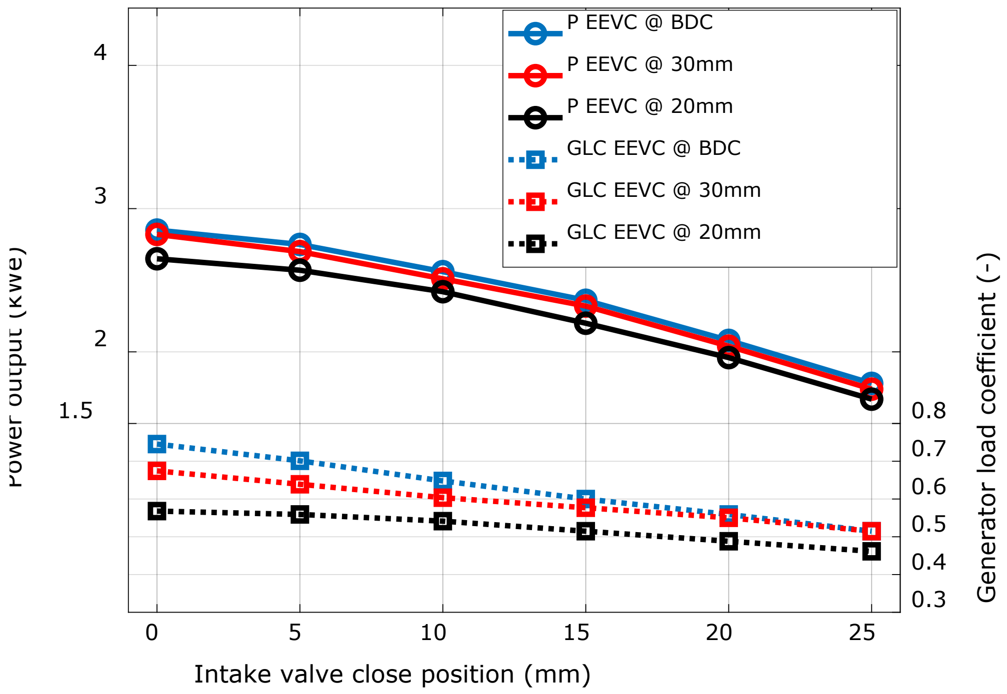

Figure 8-19. Coefficient of generator load constant and system power output at 0.933 CER.

8.4 Effect of operation temperature

The influence of expander intake temperature on system performance was investigated, and the results obtained are presented in Figure 8-20 to Figure 8-25. The expander intake temperature considered was between 950 K and 1250 K (considering any metallurgical constraints), while the other input parameters remained the same as in Table 8-1. Most of the results obtained show that system efficiency observed the same trend of increasing intake temperature, regardless of CER, provided that the same valve timings were adopted. There was an overall improvement in system efficiency and power output with increased expander intake temperature.

However, an exception to system efficiency improvement with increased temperature occurred when the EEVC at BDC and the intake duration extended to 5mm before the mid-stroke (see Figure 8-20, Figure 8-22 and Figure 8-24). The system efficiency decreased when the expander intake duration extended beyond 5 mm before the mid-stroke and the EEVC at BDC at increased expander intake temperature. Due to the operating parameter combination, the optimal system temperature at that combination was around 950 K, and the system efficiency would reduce beyond 950 K; this is because fuel consumption increased with temperature, and with increased temperature, the heat loss to the environment increased. The system power output is proportional to the operating frequency [3] and temperature (see Figure 8-29). At this operating parameter combination, the proportionality of frequency increase with temperature is not proportionate with the increase in fuel consumption due to higher temperatures.

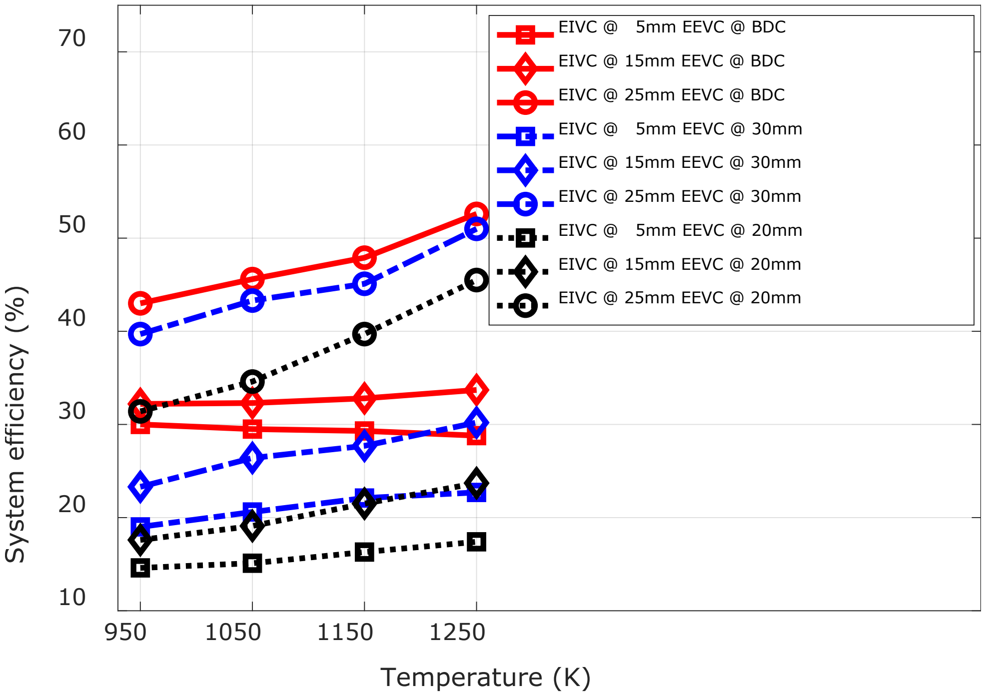

Figure 8-20. System efficiency and temperature at CER 0.736.

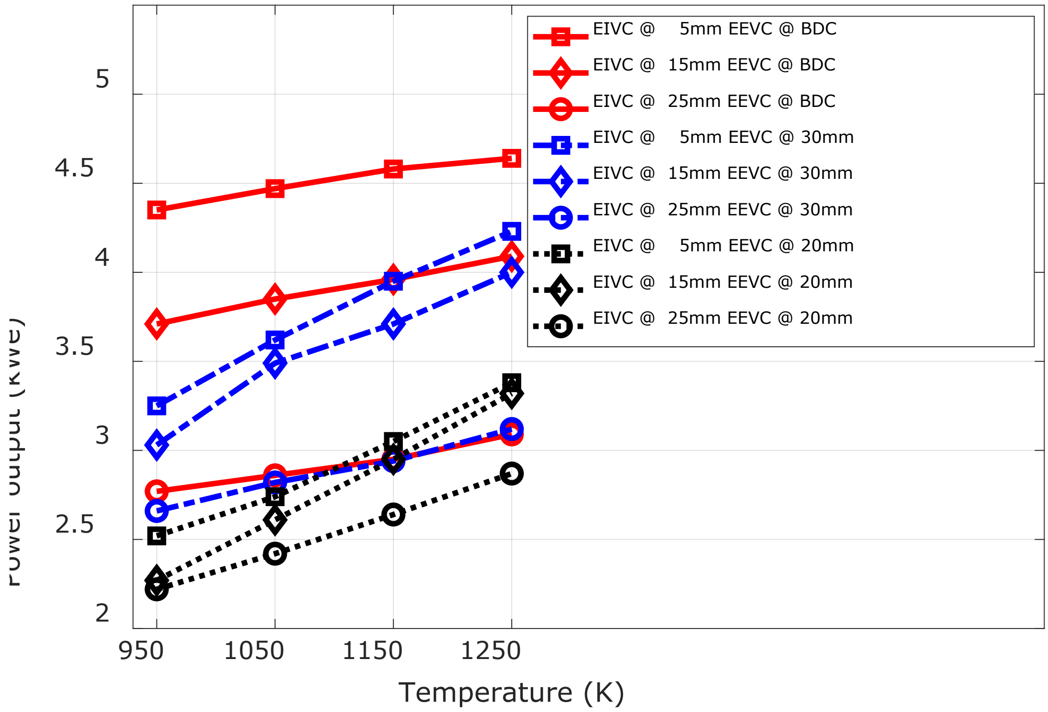

Figure 8-21. Power output and temperature at CER 0.736.

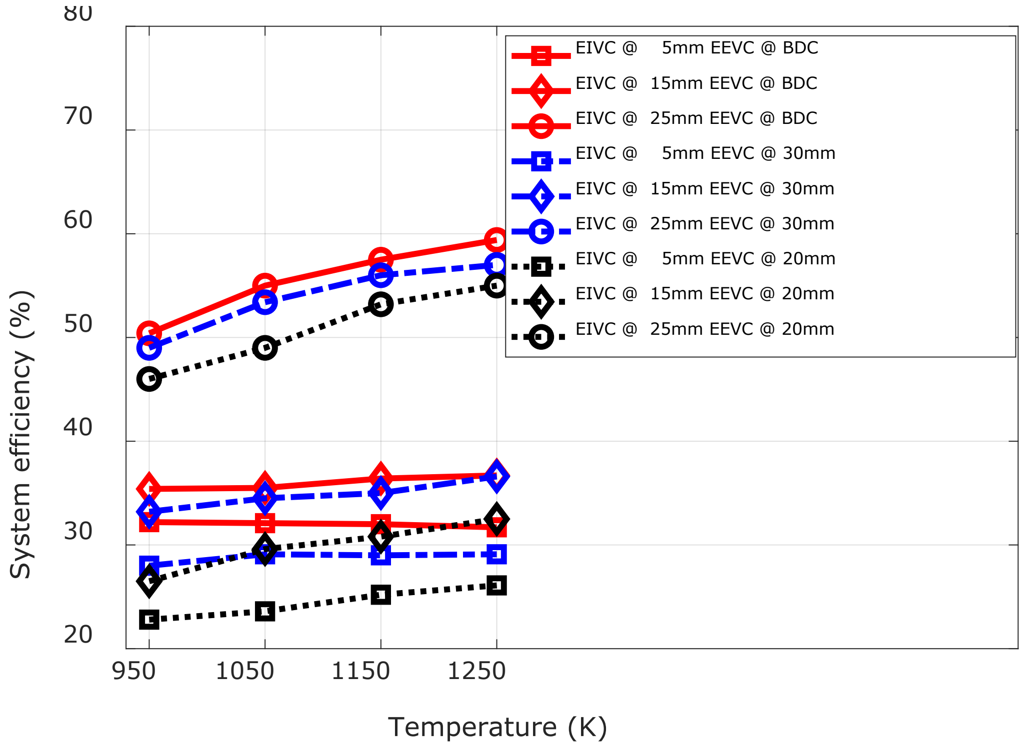

Figure 8-22. System efficiency and temperature at CER 0.823.

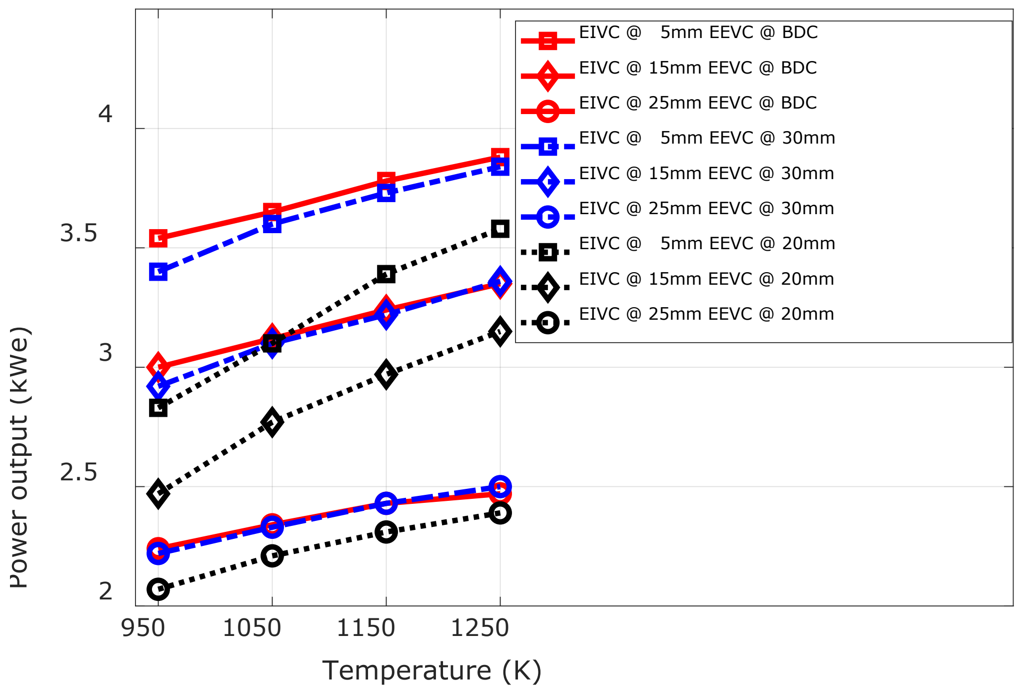

Figure 8-23. Power output and temperature at CER 0.823.

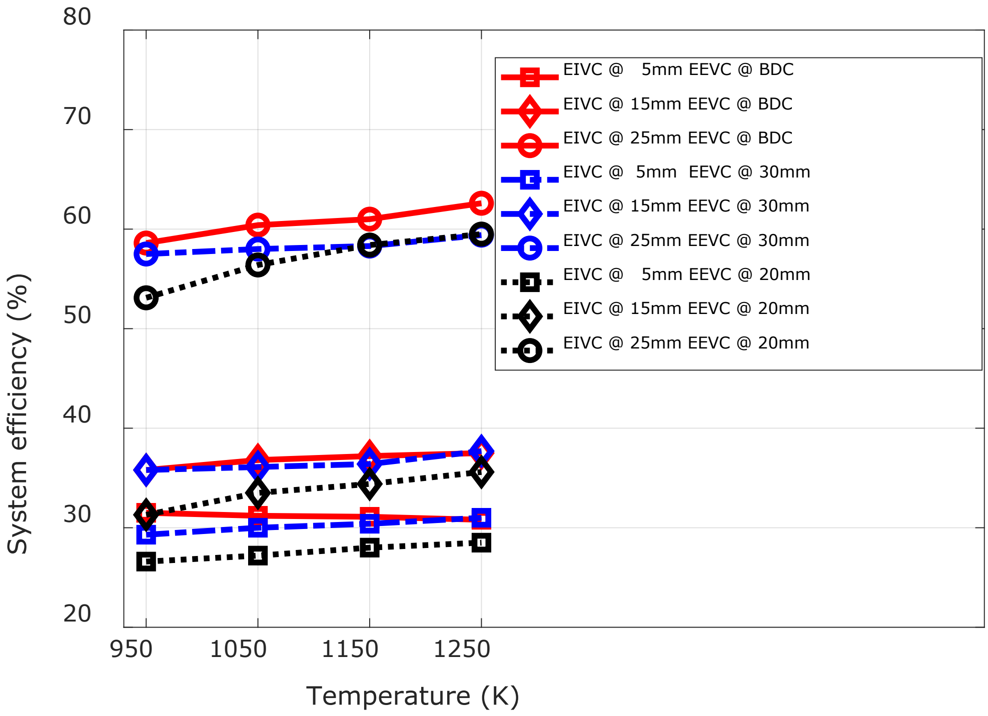

Figure 8-24. System efficiency and temperature at CER 0.933.

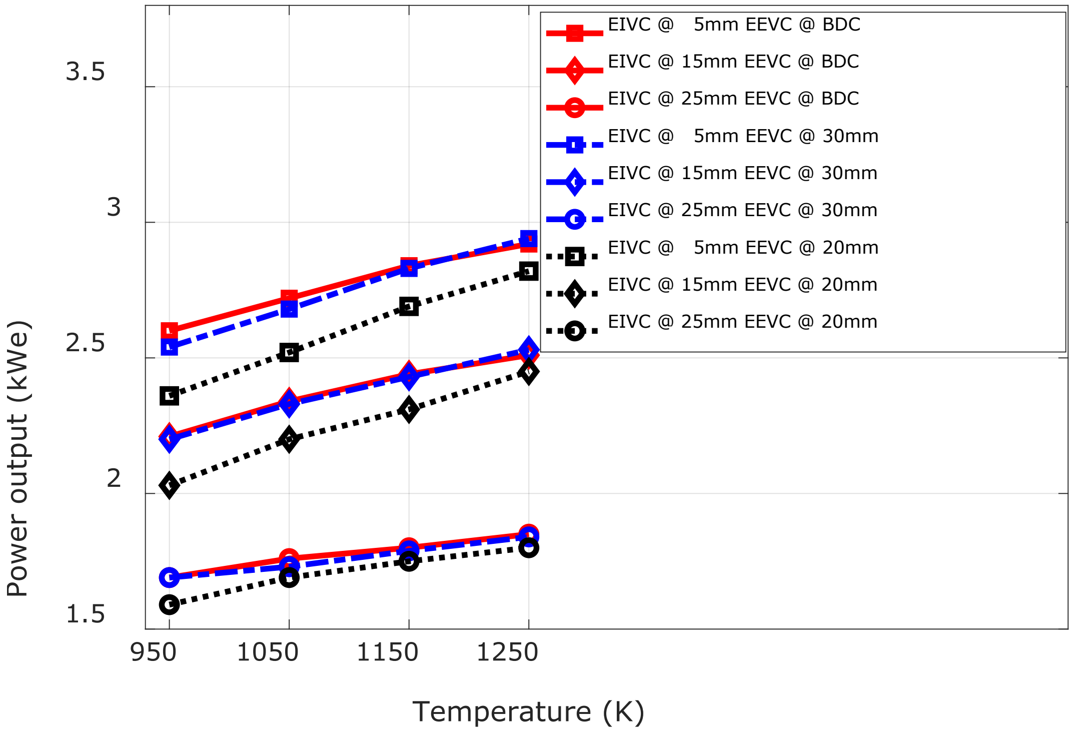

Figure 8-25. Power output and temperature at CER 0.933.

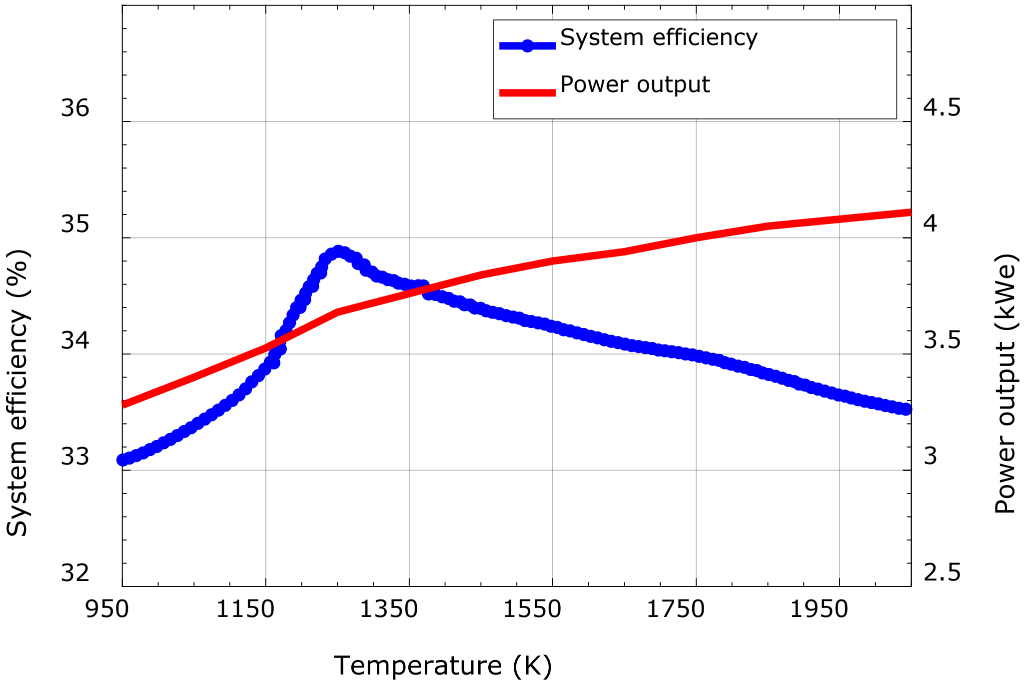

Figure 8-26. Power output and system efficiency with expander intake temperature, CER 0.823, EIVC at 10 mm and EEVC at OBDC.

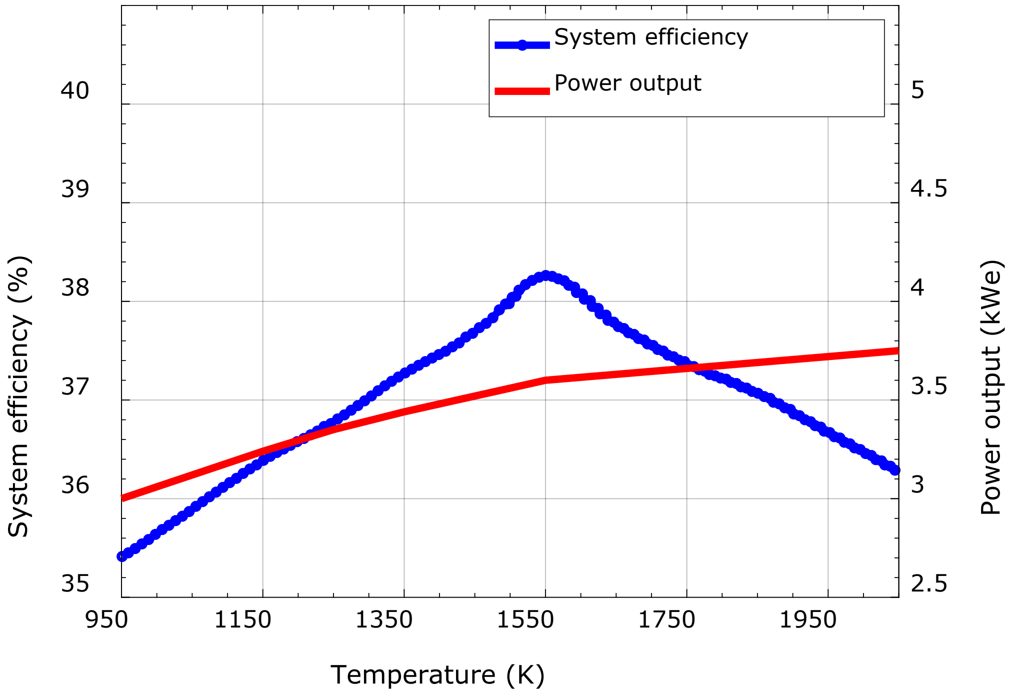

Figure 8-27. Power output and system efficiency with expander intake temperature, CER 0.823, EIVC at 15 mm and EEVC at OBDC.

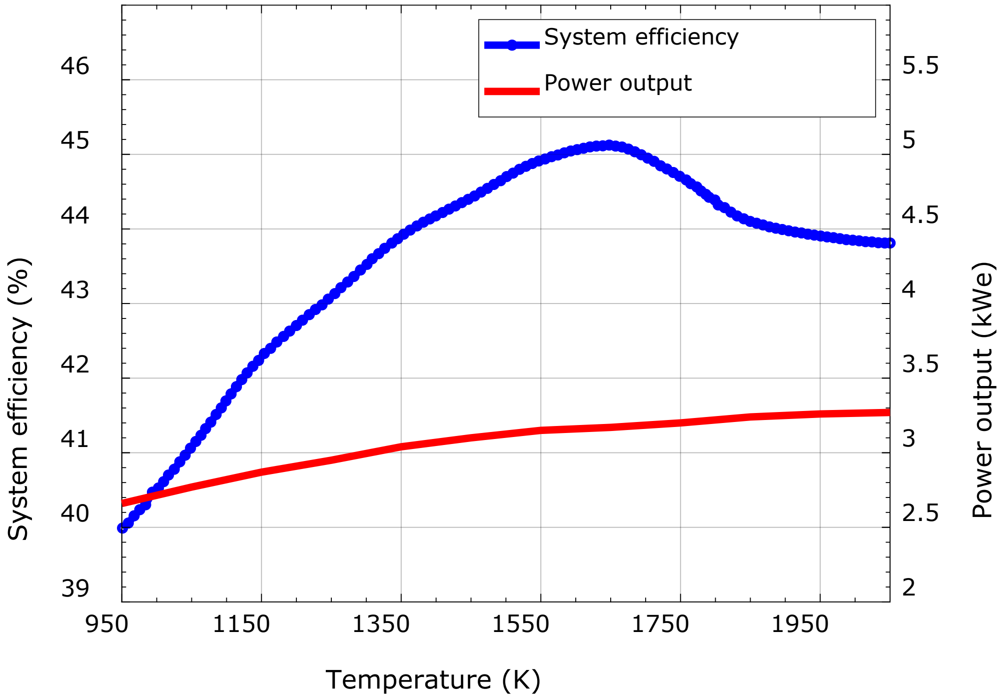

Figure 8-28. Power output and system efficiency with expander intake temperature, CER 0.823, EIVC at 20 mm and EEVC at OBDC.

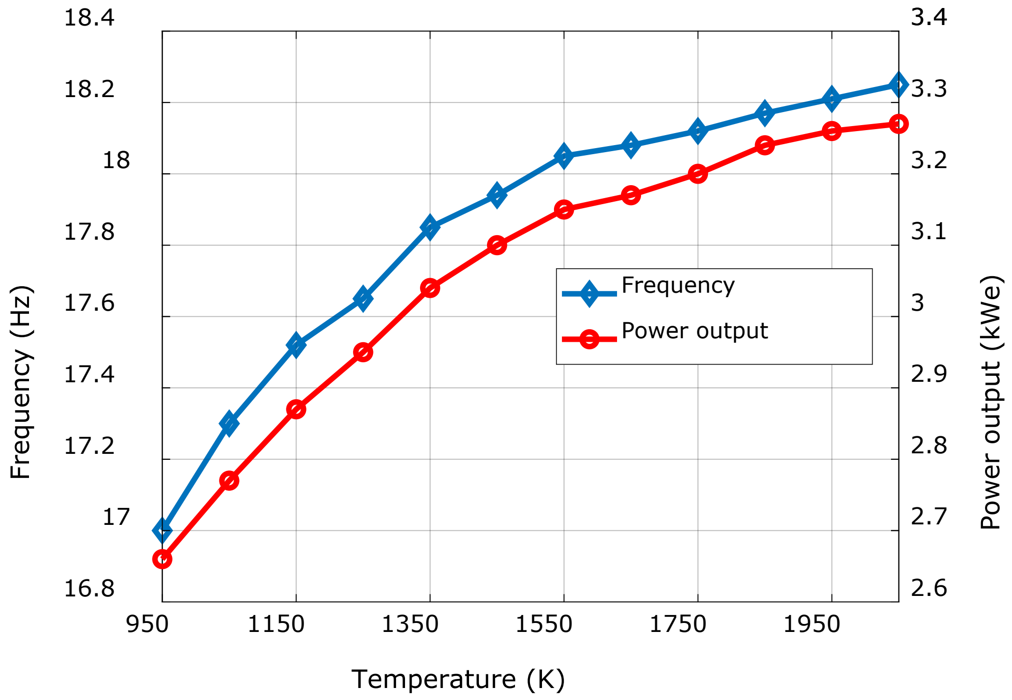

Figure 8-29. Power output and system frequency with expander intake temperature, CER 0.823, EIVC at 20 mm and EEVC at OBDC.

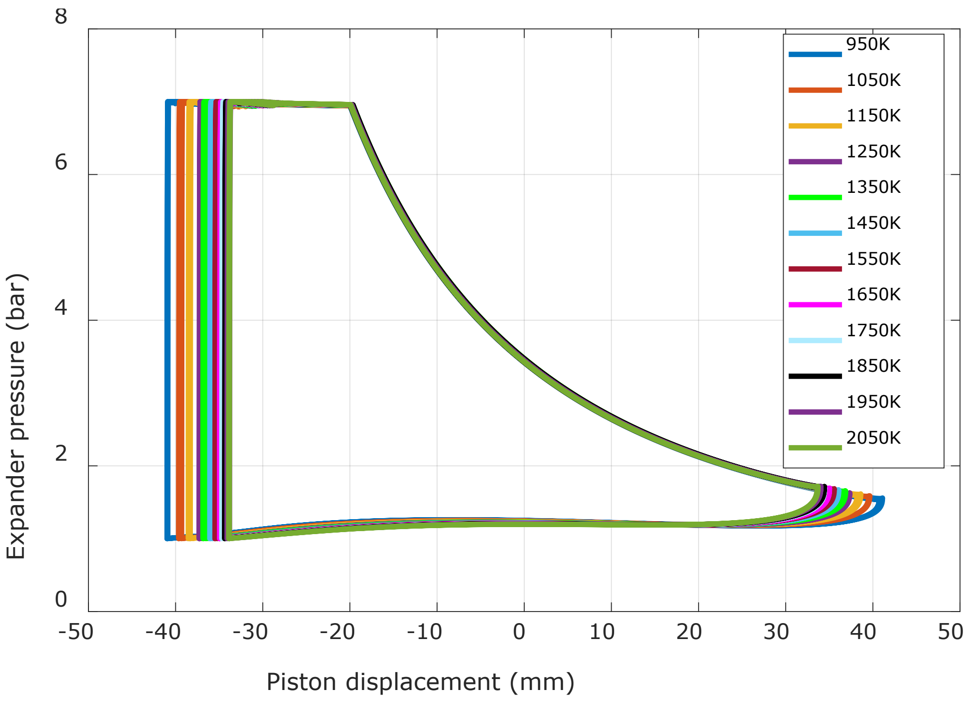

Figure 8-30. Expander in-cylinder pressure with displacement, EIVC at 20 mm, EEVC at OBDC, CER 0.823 and different intake temperature.

The relationship between expander intake temperature and system efficiency and power output was investigated (presuming no metallurgical issue on the LJEG component material selection). The results are presented in Figure 8-26 to Figure 8-28. System efficiency increased with expander intake temperature until a specific optimal temperature was reached, depending on the adopted valve timings. Above that temperature, system efficiency started to decrease with a further increase in intake temperature. The decrease in efficiency at an increased temperature beyond the optimal temperature is because of the fixed system operating variables; perhaps if the pressure ratio were not fixed and are optimised, the system efficiency would always increase with the temperature. At post-optimal temperature, the proportionality of frequency increase with temperature is not comparable with the increased fuel consumption due to higher temperatures. If the other operating variables were not fixed and duly optimised, the system efficiency would increase with intake temperature. Power output increased continuously with intake temperature despite the optimal intake temperature point. However, the changing rate of power output differed in the pre-optimal and the post-optimal performance. In Figure 8-27, the changing rate of the power output is one Watt per Kelvin (1 W/K) until it gets to 1550 K (pre-optimal performance). Above 1550 K (post-optimal performance), the changing rate of power output drops to 0.3 Watts per Kelvin (0.3 W/K). It is apparent from Figure 8-26 to Figure 8-28 that the optimal performance temperature was dependent on the adopted intake valve timing. At a shorter intake duration, the frequency per fuel consumption is higher than the extended intake duration, resulting in a higher power density, thus a higher system efficiency. The proportionality of frequency increase with temperature is more subsistent with increased fuel consumption due to higher temperatures at shorter intake duration than extended intake duration. That is why the optimal temperature region shifts to the right at shorter intake duration. This is seen in Figure 8-20 to Figure 8-25 when the EIVC at 15 mm and 20 mm, respectively, and the optimal intake temperature was around 1550 K and 1650 K, respectively.

The relationship between power output and system frequency at varying intake temperature, as depicted in Figure 8-29, shows that the power output and the frequency increased with the intake temperature. The expander in-cylinder pressure and the piston stroke in complete cycles are shown in Figure 8-30 in terms of varying intake temperature.

It was observed that intake duration became shorter with increased expander intake temperature; because less working fluid was demanded from the compressor at increased expander intake temperature, i.e. higher temperatures would enhance the volumetric fluid quantity in the combustor. Therefore, most of the compressed fluid in the compressor at the end of compression was not used, and this loss was responsible for a decreased system efficiency of post-optimal performance.

8.5 Power density

The power density (power per expander swept volume) correlation with the CER and valve timings are presented in Figure 8-31 to Figure 8-39. The input parameters were the same as those presented in Table 8-1. At fixed CER, power density generally increased with extended inlet duration, especially when the EEVC at BDC or very close to the BDC. Additionally, it was evident from Figure 8-31 to Figure 8-39 that the early closure of exhaust valve undermined power density irrespective of the inlet duration adopted. Therefore, at fixed CER, power density was dependent on both expander intake and exhaust duration.

At fixed operational parameters (expander intake and exhaust duration), the power density increased with CER, and this was most likely associated with a reduction in the piston stroke at increased CER. Further investigation into Figure 8-31 to Figure 8-39 established that power density increased with CER irrespective of expander intake or the exhaust valve timing adopted. However, the relationship between power density and intake valve timing appeared complicated if the exhaust valve closed before the OBDC, and this relationship appeared to depend more on the CER. The power density decreased with a longer intake duration at low CER, but the trend tended to reverse at increased CER. In summary, power density increased with CER and with extended intake and exhaust duration. However, its relationship with intake duration seemed to be interdependent on CER.

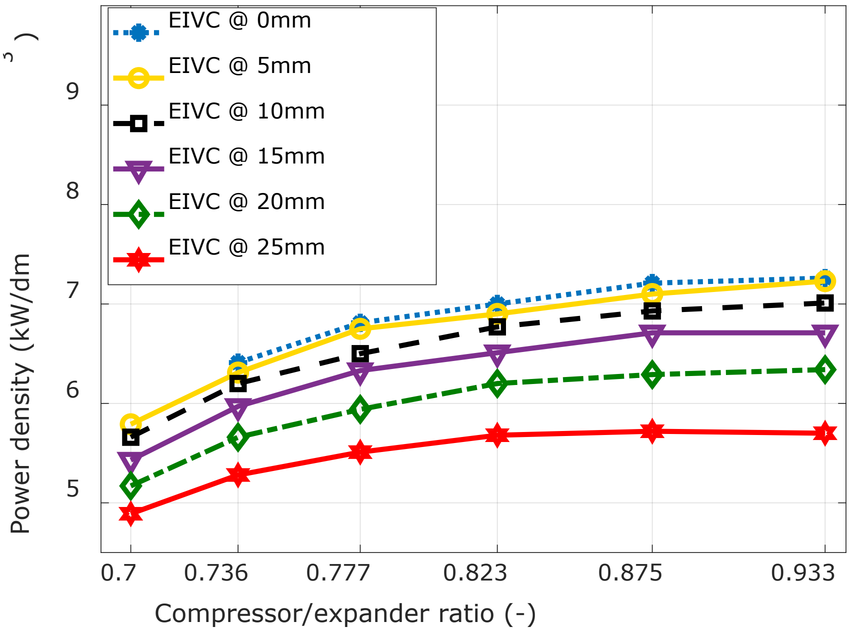

Figure 8-31. Power density with the compressor/expander ratio when exhaust closed at BDC.

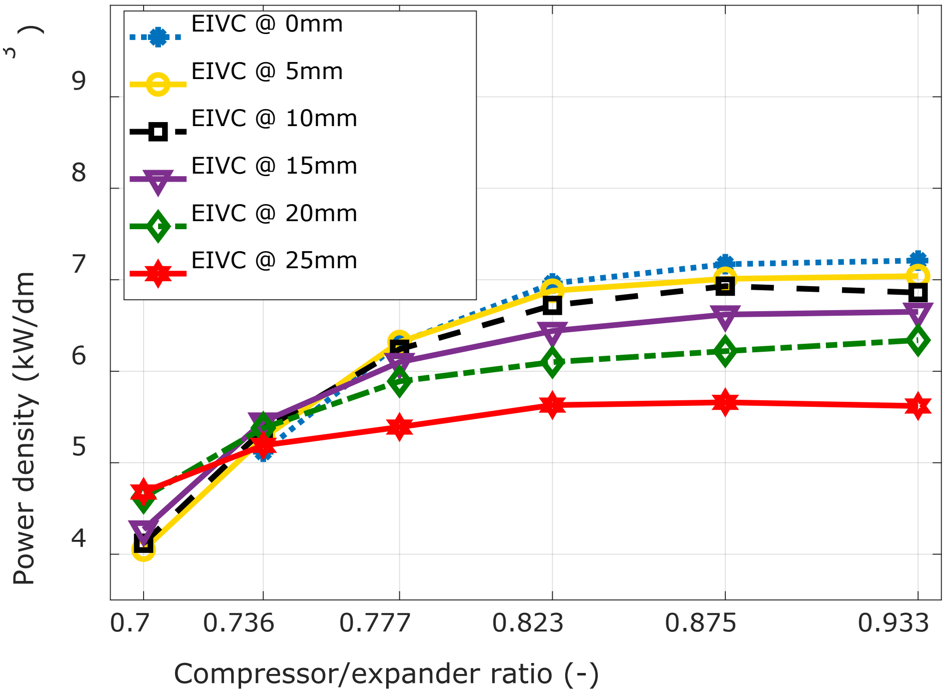

Figure 8-32. Power density with the compressor/expander ratio when exhaust closed at 30 mm.

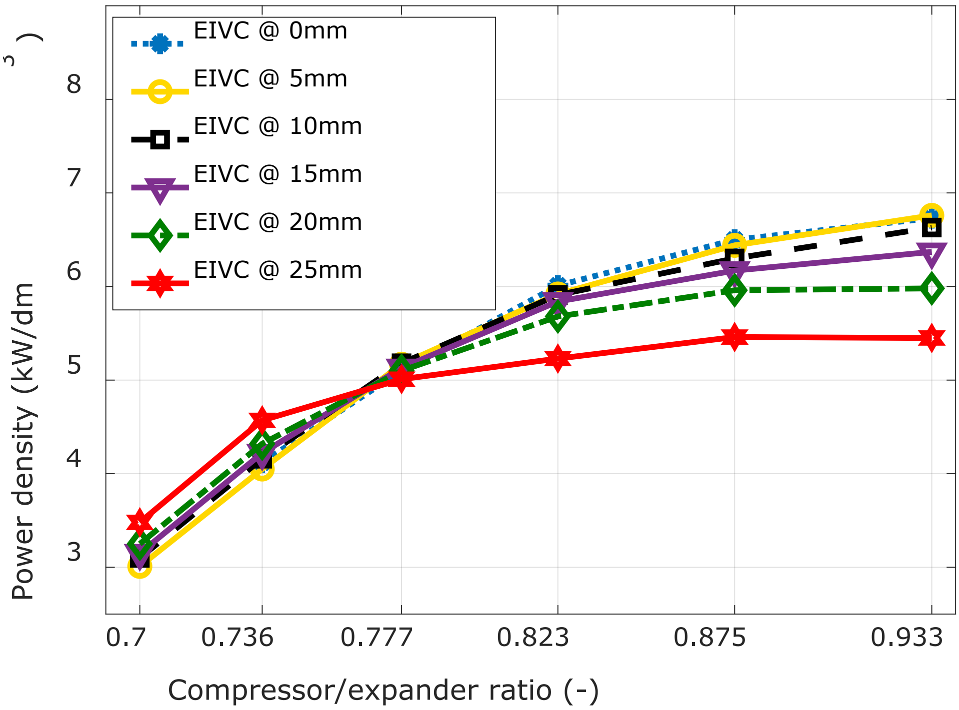

Figure 8-33. Power density with the compressor/expander ratio when exhaust closed at 20 mm.

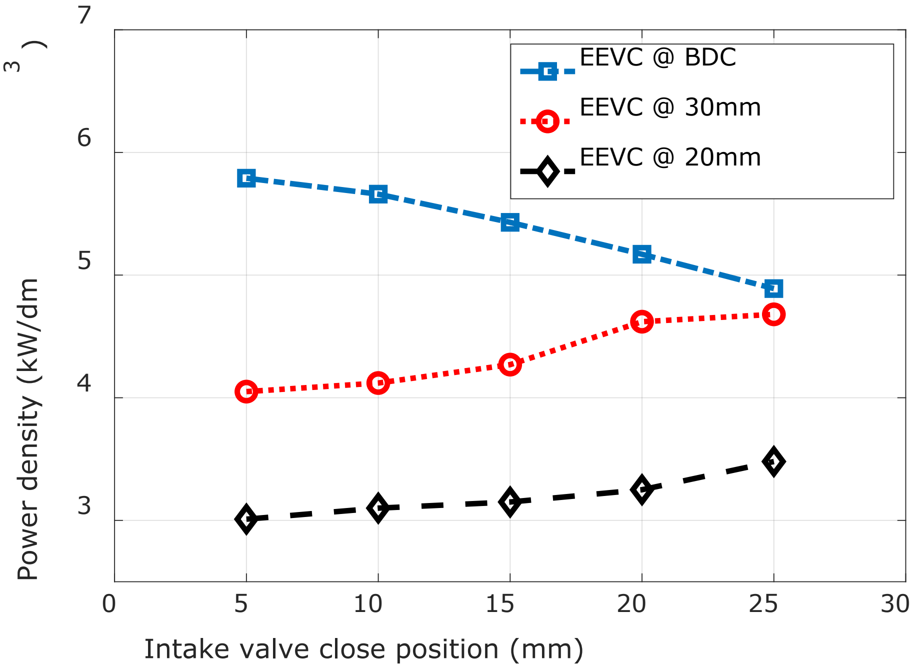

Figure 8-34. Power density with expander intake duration at CER of 0.7.

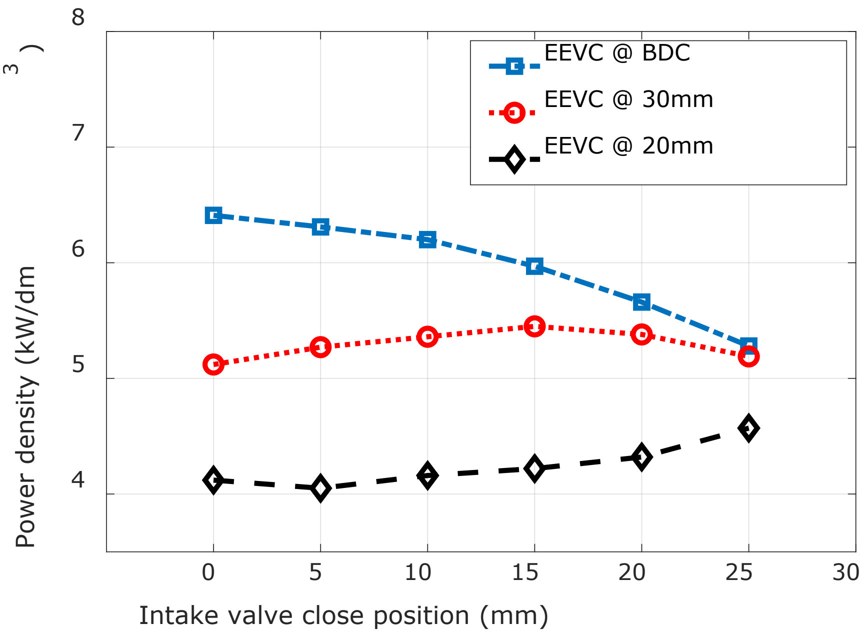

Figure 8-35. Power density with expander intake duration at CER of 0.736.

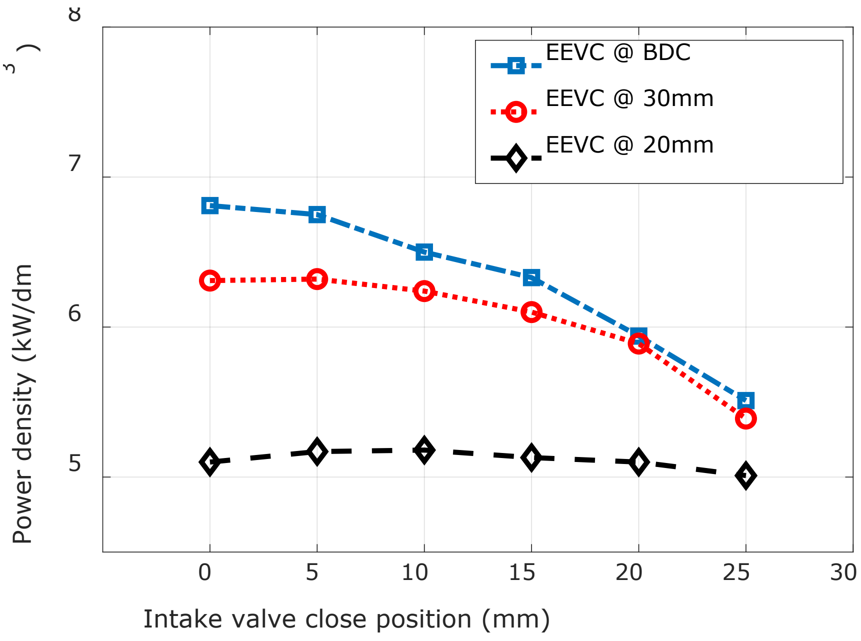

Figure 8-36. Power density with expander intake duration at CER of 0.777.

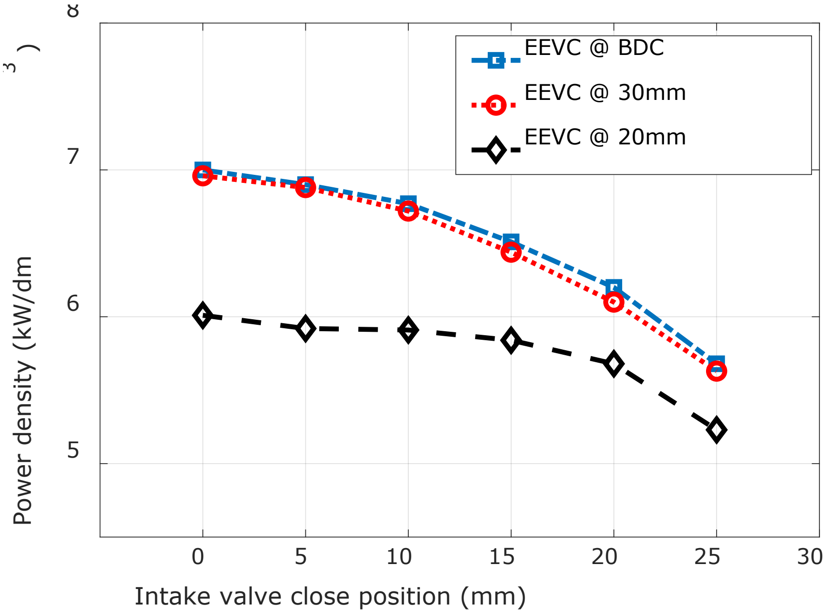

Figure 8-37. Power density with expander intake duration at CER of 0.823.

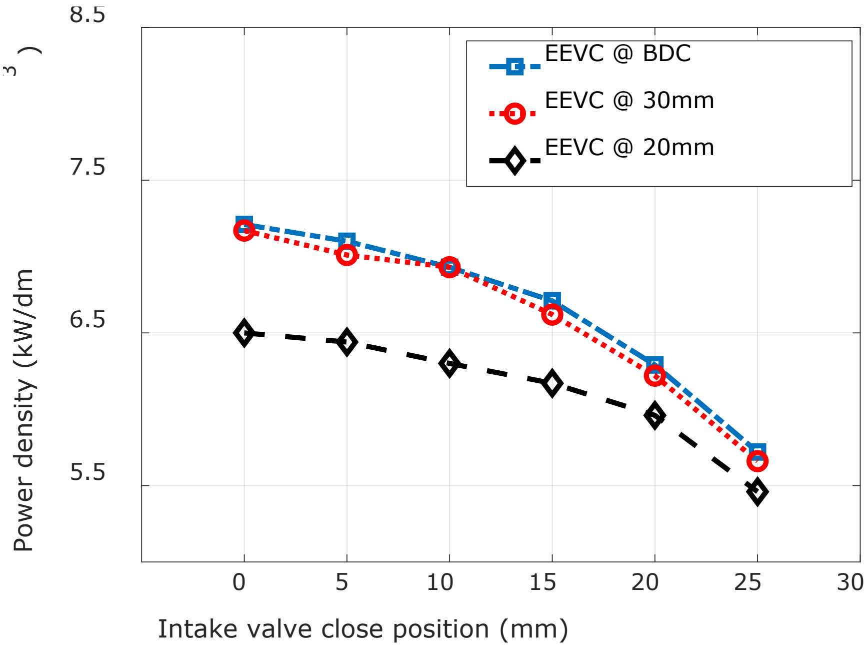

Figure 8-38. Power density with expander intake duration at CER of 0.875.

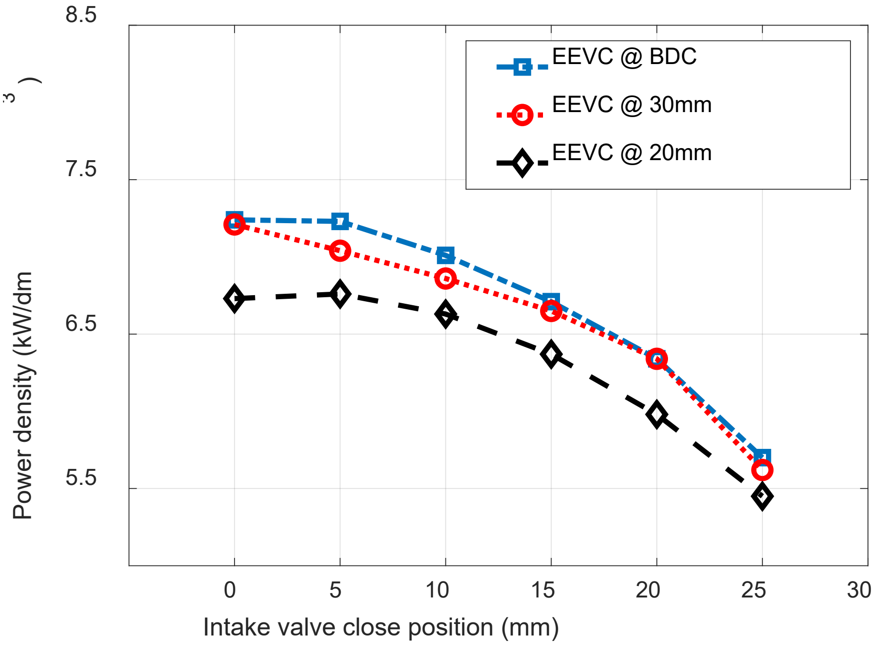

Figure 8-39. Power density with expander intake duration at CER of 0.933.

8.6 Reactor matching with multiple expander-compressor-generator set.

The reactor of an LJEG operated periodically because the fluid flow pattern in the compressors and expander are intermittent. In order to eliminate this periodic operation and increase the power density, the feasibility of using a single reactor coupled with multiple and identical expander-compressor-generator sets was investigated. The reactor active and idle operation per cycle is shown in Figure 8-40 for different expander intake valve timing and at optimal generator load, while other variables remained constant. Implementing the expander intake valve to close at 24 mm before mid-stroke (EIVC@24 mm) resulted in 18.5% reactor active and 81.5% idle per cycle, while implementing EIVC@6 mm resulted in 32.2% reactor active and 67.8% reactor idle operation. Any identical expander-compressor generator sets would use the reactor during reactor idling operation, represented by zero for the scenarios presented in Figure 8-40. Advancing the expander intake valve closing timing favoured a higher percentage of reactor idling time per cycle and vice versa when the expander intake closing timing is retarded.

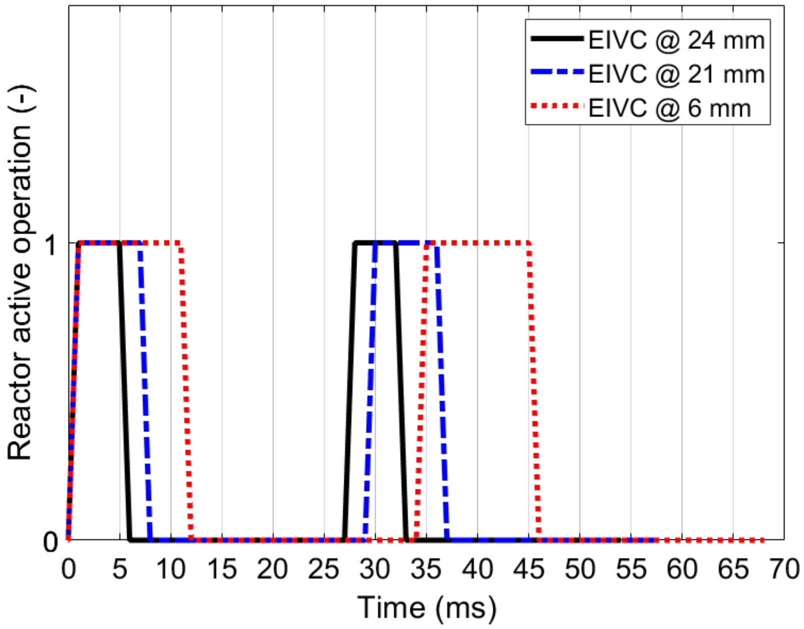

Figure 8-40. Reactor periodic operation per cycle, EIVC @ 24 mm, 21 mm and 6 mm, reactor temperature 1100 K, EEVC @ OBDC, CER 0.823.

The investigation results on the feasibility of coupling a single reactor with multiple identical expander-compressor-generator sets are presented in Table 8-2. From the selected expander intake valve operations presented in Table 8-2, EIVC @ 6 mm accommodated three identical expander-compressor-generator sets for a single reactor, and EIVC @ 21 mm and EIVC @ 24 mm accommodated four and five identical expander-compressor-generator sets for a single reactor, respectively. The results revealed that the number of the expander-compressor-generator set that could be matched to a reactor, the frequency, the efficiency and the total power output was favoured by retarding the expander intake duration.

Table 8-2. LJEG potential single reactor coupling, EEVC @ OBDC, CER 0.823, reactor temperature 1100 K.

Parameters [Unit]	EIVC @ 6 mm	EIVC @ 21 mm	EIVC @ 24 mm
Reactor active time per expander-compressor-generator set [ms]	11	7	5
Potential number of expander-compressor-generator sets to be coupled [-]	3	4	5
Frequency [Hz]	14.7	17.2	18
Efficiency [%]	32	44	55
Power output per set [kW]	3.6	2.75	2.3
Power density [kW/litre]	6.8	6.1	5.8
Total power from potential coupled sets [kW]	10.8	11	11.5

In any case, retarded expander intake duration with multiple identical expander-compressor-generator sets coupled to a single reactor would lead to increased total power at higher system efficiency. However, it would also lead to decreased power density (kW/litre) and specific power (kW/kg). Consequently, there would always be a trade-off between adopting a multi-set retarded expander intake duration scenario and a multi-set advanced expander intake duration scenario. This trade-off, for the case of retarded expander intake duration, would be higher capital cost (because a higher number of an expander-compressor-generator set would be needed), lower specific power, lower power density, higher operational efficiency and higher total power output. Against lower capital cost, higher specific power, higher power density, lower operational efficiency and lower total power output for advanced expander intake duration.

Nevertheless, the coupling of multiple and identical expander-compressor-generator sets to a single reactor would increase the specific power output compared to any case, in which a single reactor would power a single identical set of expander-compressor-generator, regardless of the preference of the expander intake duration adopted.

8.7 Conclusions

This chapter presents a novel semi-closed cycle Linear Joule Engine Generator (LJEG) model with a hydrogen-oxygen-argon reactor. The system performance with different operating conditions was examined, and it is found that:

1. A peak system efficiency of around 40% and 60% was achieved when the compressor/expander ratio is 0.70 and 0.93, respectively, and the exhaust valve closed at the piston bottom dead centre while the intake closed at 25 mm from mid-stroke.

2. The limit of extension of expander intake duration depended on the compressor/expander diameter ratio. Increased compressor/expander ratio supported longer intake duration up to the mid-stroke, and there was a narrow range of expander intake duration possibilities for stable operation in LJEG. The ability of an LJEG to recover from disturbance was considerably lower at shorter intake duration and more robust at longer intake duration.

3. The system efficiency increased with the compressor/expander ratio and decreased with extended intake duration. The system efficiency could be improved by extending the expander exhaust duration, and optimal efficiency was achieved if the expander exhaust duration was extended to the piston bottom dead centre.

4. Power output generally increased with longer expander intake duration, and the relationship between power output and the compressor/expander diameter ratio was dependent on the expander exhaust duration adopted. Power output was improved by extending the expander exhaust duration. Peak power was achieved at any set of parameters if the expander exhaust duration was extended to the piston bottom dead centre.

5. Piston stroke decreased with increased compressor/expander ratio, and power density increased with both compressor/expander diameter ratio and extended inlet and exhaust duration.

6. For every set of operating conditions, a particular range of electric load could ensure optimum system performance. Therefore, the system efficiency could be improved with a satisfactory electric load match for different operating conditions.

7. The system operating temperature for optimal performance was dependent on the adopted intake valve timing. However, a clear trend emerged that a longer intake duration led to lower optimal temperature while a shorter intake duration led to a higher optimal temperature.

8. The idle reactor operation could be eliminated by coupling multiple expander-compressor-generator set to a single reactor. This would increase total power, specific power and power density compared to a single reactor coupled to an expander-compressor-generator set. The percentage of reactor idling time determined the number of the expander-compressor-generator set that could be matched to a reactor, and this was favoured by retarding the expander intake duration.

Chapter 9: Conclusions and recommendation

This thesis described the research contributions to developing a semi closed-cycle linear Joule engine generator using argon as the primary working fluid and oxy-hydrogen external combustion heat input. The engine generator aims to provide a means for small to medium-sized, zero-carbon emissions hydrogen to electricity conversion. The investigation showed that the LJEG is technically feasible; however, there could be material constraints depending on system operating temperature. For example, a dry lubrication expander piston ring that could be reliable above 870 K temperature is very rare at the time of this report. The other essential research questions about the system performance, the variables that would influence the system operation and system optimisation were answered in Chapter 6 and Chapter 8 of the thesis.

Some conclusions have been highlighted at the end of each chapter; however, the more relevant ones are summarised in this Chapter and recommendations for potential future work are presented.

9.1 Summary of the results

A comprehensive literature review of technologies related to the LJEG was presented in Chapter 2; this background study focused on external powered free-piston technology, reciprocating Joule cycle engine and noble gas circulation in hydrogen combustion technology. In externally powered free-piston technology, most reported air-standard cycle experimental studies achieved a stable operation and attractive conversion efficiencies. The reciprocating Joule cycle engine technology appears attractive because of the performance output and its ability to utilise most conventional fuel sources, both processed and unprocessed, as well as solar energy. The notable recommended improvement for optimal engine performance is a reduction in friction losses and intelligent valve timing. Recent advances in control and automation would provide a solution to intelligent valve timing operation, and friction losses could be minimised by adopting free-piston technology. In order to ensure zero emissions in hydrogen combustion, the use of noble gas as the primary working fluid is proposed. Based on reported literature on the use of noble gases in hydrogen combustion, argon was selected; among other essential qualities, argon is abundantly available, compared with other available noble gases, and argon is relatively inexpensive and could be readily obtained as a by-product in cryogenic air separation.

The research methodology adopted was presented in Chapter 3, including experimental testing, dry friction force analysis, full-cycle modelling and system analysis, and optimisation. Based on the background study, a semi-closed-loop linear Joule engine generator using argon as the primary working fluid and employing oxy-hydrogen combustion was proposed and presented in Chapter 4. Detailed working principles of the proposed semi-closed cycle LJEG and the air-standard open cycle LJEG were presented in Chapter 4, and the experimental procedure on the air-standard open cycle LJEG rig was equally discussed in Chapter 4.

The development and coupling of the zero dimension, single-zone full-cycle model of the semi-closed cycle LJEG were presented in Chapter 5. The complete cycle model constitutes detailed sub-models included; hydrogen combustion model, dry friction model, system dynamic model, condenser model, linear electric generator model, valve operation models and the expander and compressor thermodynamic models. Both heat transfer and air leakage were calculated in the compressor and expander models. The simulation sub-models were developed in Matlab/Simulink coupled with Matlab/Thermolib. While Matlab/Thermolib was used to develop the sub-models of combustion, condenser, and fluid flow, the rest of the sub-models were developed in Matlab/Simulink. The valve timing operations were executed in the Stateflow function in Simulink.

Chapter 6 presented the numerical model validation of the open cycle LJEG with the LJEG prototype test data, while the combustion model was validated with test data from the literature. The simulation results were as well presented. The test results were in very reasonable similarity with the simulated results, which would mean that the numerical model was robust and could reasonably predict the engine's characteristics.

The preliminary investigation of the operational characteristics, performance evaluation and the influence of the main design variables were conducted. The results indicated that the LJEG design and operational variables are strongly interrelated, with variations in each variable influencing several aspects of the operation. The simulation results identified the working fluid and cycle pressure as the absolute essential parameters. At the same time, the valve timing and electric load would be described as the essential adjustable vital parameters. The valve timing and electric load are optimised depending on the preference between engine efficiency and power output. The valve timing was the most effective parameter to achieve a higher electric power from the generator, and the electric load was found to be the most influential parameter for efficiency improvement.

The novel friction model of the LJEG operating on dry friction principle is presented in Chapter 7 and validated with an LJEG prototype test data. The proposed numerical dry friction model is represented as a dry friction model of a mass-spring-damper mechanical system and friction force developed due to compression pressure. The model accounted for macroscopic sliding solely. Test results from an LJEG prototype were correlated with the numerical simulation results predicted by the proposed model and other published friction models relevant to describing the LJEG friction. The comparisons indicated that the proposed model described the friction behaviour of the LJEG. Aside from the surface properties of the piston ring and cylinder liner interface, the system pressure, piston velocity, and piston acceleration were the most influential parameters identified in describing the friction behaviour of the LJEG. The principal advantages of the proposed model were its simplicity in numerical development and the accuracy of numerical simulation results.

Detailed parametric evaluations of the proposed semi-closed-loop LJEG adopting argon as the primary working fluid and oxy-hydrogen combustion for heat addition were presented in Chapter 8. A comparison study confirmed the benefits of the proposed conceptual design; substituting air with argon as the primary working fluid resulted in over 60% indicated efficiency enhancement. Moreover, a parametric analysis was carried out to understand the impact of different variables like the expander intake and exhaust valve timing operation, electric load, the CER, and working temperature on the system performance. The investigation revealed that the power output increased with more extended expander intake duration; however, its relationship with the CER is dependent on the adopted expander exhaust valve timing. Efficiency decreased with the expander extended intake duration, although it could be enhanced with a more extended expander exhaust duration. Optimal efficiency was achieved if the expander exhaust duration was extended to the piston bottom dead centre. Peak efficiencies of 40% and 60% are accomplished when the CER is 0.70 and 0.93, respectively. The system working temperature for optimal performance depended on valve timing adopted; more prolonged intake duration led to lower optimal working temperature while briefer intake duration led to a higher optimal working temperature. Further results indicated that power density increased with CER and with extended intake and exhaust duration; however, the correlation with intake duration appeared to be interdependent on the CER. The investigation on the feasibility of coupling a single reactor with multiple identical expander-compressor-generator sets was presented.

The insight from this research and the test results of the first-generation prototype led to the developing of the second-generation LJEG prototype. Some pictures of the second-generation LJEG prototype are in Figure 9-1. All the processes and components of a semi-closed-loop LJEG described in section 4.1 Engine description, including the argon-oxy-hydrogen reactor and condenser, were fully incorporated in the prototype. However, when writing this thesis, the second-generation rig was still under installation and, therefore, not ready for testing.

Figure 9-1. The Second-generation prototype of the Linear Joule Engine Generator.

9.2 Recommendations and future works

The LJEG exhibits promising benefits for a zero-emissions medium-scale power generation. However, meaningful progress would be needed to develop the technology into a commercially viable package. The following areas are considered paramount to the advancement of this technology and would need to be investigated further.

9.2.1 Fluid flow investigation

Since the fluid flow in the LJEG is considered pulsating, and the internal volume of the expander and compressor are not fixed but could vary according to operation. There is a need to optimise the valve design operation to enhance the volumetric efficiency of both the expander and the compressor, the general flow design, and ensure stable combustion through enhanced flow patterns. Perhaps this investigation would determine if there will be the need to integrate resonators in the flow system or otherwise. Moreover, if there is a need, analyse the natural frequency of the piping segments and tune the resonator frequencies properly with the engine frequency. Furthermore, investigate the effect of out-of-system tuning would have on the performance of the engine.

9.2.2 Multidimensional simulation

This current research adopted zero-dimensional, single-zone modelling for developing the LJEG. This practice is prevalent in conventional engines development, especially in engine performances and dynamics. Because the argon-oxy-hydrogen combustion LJEG is a semi-closed cycle type, it would be imperative to analyse the design and integration of the reactor and flow processes. Because of this need, a multi-dimensional simulation model seems to be the most appropriate type of model. Therefore, a multi-dimensional simulation model needed to be developed based on the results from the single zone, zero-dimensional model of the LJEG and the enhanced fluid flow investigation described in subsection 9.2.1. By incorporating the fluid flow investigation results together with the results of the zero-dimensional model in the multi-dimensional simulation model, the engine performance and flow design will be further optimized.

9.2.3 Prototype testing

The semi-closed cycle LJEG prototype using argon as the major working fluid and oxy-hydrogen combustion for heat addition has been built, and it is currently being installed. The operation optimisation parameters identified from this study should be implemented and investigated on the prototype to verify how these parameters variations would affect the system performance. Implementing the instantaneous calculation of the quantity of fuel/oxidant needed based on the prevailing engine condition adopted in this study should be implemented in the prototype control system because of safety concerns. Further investigations into LJEG response to disturbances and operational stability should be accomplished through testing.

References

[1] "I.E.A. World Energy Outlook 2019," 2019.

[2] "E.I.A. International Energy Outlook 2019," 2019.

[3] "EXXONMOBIL. Outlook for Energy: A View to 2040," 2018.

[4] "B.P. Energy Outlook 2019," 2019.

[5] M. Maslin, *Global Warming: a Very Short Introduction*. Oxford: OUP, 2008.

[6] F. Li, D. R. MacFarlane, and J. Zhang, "Recent advances in the nanoengineering of electrocatalysts for CO2 reduction," *Nanoscale*, vol. 10, no. 14, pp. 6235–6260, 2018, doi: 10.1039/c7nr09620h.

[7] Z. Fu *et al.*, "Photocatalytic conversion of carbon dioxide: From products to design the catalysts," *J. CO2 Util.*, vol. 34, pp. 63–73, 2019, doi: 10.1016/j.jcou.2019.05.032.

[8] M. Y. Haller, D. Carbonell, M. Dudita, D. Zenhäusern, and A. Häberle, "Seasonal energy storage in aluminium for 100 percent solar heat and electricity supply," *Energy Convers. Manag. X*, vol. 5, 2020, doi: 10.1016/j.ecmx.2019.100017.

[9] C. Bae and J. Kim, "Alternative fuels for internal combustion engines," *Proc. Combust. Inst.*, vol. 36, no. 3, pp. 3389–3413, 2017, doi: 10.1016/j.proci.2016.09.009.

[10] W. Bou Nader, "Thermoelectric generator optimization for hybrid electric vehicles," *Appl. Therm. Eng.*, vol. 167, 2020, doi: 10.1016/j.applthermaleng.2019.114761.

[11] C. Zhang and Z. Sun, "Trajectory-based combustion control for renewable fuels in free piston engines," *Appl. Energy*, vol. 187, pp. 72–83, 2017, doi: 10.1016/j.apenergy.2016.11.045.

[12] I. Vinoth Kanna, A. Vasudevan, and K. Subramani, "Internal combustion engine efficiency enhancer by using hydrogen," *Int. J. Ambient Energy*, vol. 41, no. 2, pp. 237–240, 2020, doi: 10.1080/01430750.2018.1456961.

[13] R. Mikalsen and A. P. Roskilly, "The Free-Piston Reciprocating Joule Cycle Engine: A New Approach To Efficient Domestic CHP Generation," in *International Conference on Applied Energy 2012*, 2012.

[14] D. Wu and A. P. Roskilly, "Design and parametric analysis of Linear Joule-cycle Engine with out-of-cylinder combustion," in *Energy Procedia*, 2014, doi: 10.1016/j.egypro.2014.11.1034.

[15] U. Ngwaka, B. Jia, C. Lawrence, D. Wu, A. Smallbone, and A. P. Roskilly, "The

characteristics of a Linear Joule Engine Generator operating on a dry friction principle," *Appl. Energy*, vol. 237, 2019, doi: 10.1016/j.apenergy.2018.12.081.

[16] B. Jia, D. Wu, A. Smallbone, C. Lawrence, and A. P. Roskilly, "Design, modelling and validation of a linear Joule Engine generator designed for renewable energy sources," *Energy Convers. Manag.*, vol. 165, pp. 25–34, Jun. 2018, doi: 10.1016/J.ENCONMAN.2018.03.050.

[17] M. A. Bell and T. Partridge, "Thermodynamic design of a reciprocating Joule cycle engine," *Proc. Inst. Mech. Eng. Part A J. Power Energy*, 2003, doi: 10.1243/095765003322066475.

[18] M. Creyx, E. Delacourt, C. Morin, B. Desmet, and P. Peultier, "Energetic optimization of the performances of a hot air engine for micro-CHP systems working with a Joule or an Ericsson cycle," *Energy*, 2013, doi: 10.1016/j.energy.2012.10.061.

[19] R. W. Moss, A. P. Roskilly, and S. K. Nanda, "Reciprocating Joule-cycle engine for domestic CHP systems," *Appl. Energy*, 2005, doi: 10.1016/j.apenergy.2004.03.007.

[20] B. Jia, D. Wu, A. Smallbone, U. C. Ngwaka, and A. P. Roskilly, "Dynamic and thermodynamic characteristics of a linear Joule engine generator with different operating conditions," *Energy Convers. Manag.*, vol. 173, 2018, doi: 10.1016/j.enconman.2018.07.098.

[21] R. L. Edwards, C. Font-Palma, and J. Howe, "The status of hydrogen technologies in the UK: A multi-disciplinary review," *Sustain. Energy Technol. Assessments*, vol. 43, no. July 2020, p. 100901, 2021, doi: 10.1016/j.seta.2020.100901.

[22] U. Ngwaka *et al.*, "Parametric Analysis of a Semi-Closed-Loop Linear Joule Engine Generator using Argon and Oxy-Hydrogen Combustion," *Energy*, vol. 217, 2021, doi: https://doi.org/10.1016/j.energy.2020.119357.

[23] H. Blanco, W. Nijs, J. Ruf, and A. Faaij, "Potential for hydrogen and Power-to-Liquid in a low-carbon EU energy system using cost optimization," *Appl. Energy*, vol. 232, no. September, pp. 617–639, 2018, doi: 10.1016/j.apenergy.2018.09.216.

[24] J. O. Bockris, "Environmentally Clean Fuels for Transportation," *Environ. Chem.*, pp. 583–604, 1977, doi: 10.1007/978-1-4615-6921-3_18.

[25] J. O. M. Bockris, "The hydrogen economy: Its history," *Int. J. Hydrogen Energy*, vol. 38, no. 6, pp. 2579–2588, 2013, doi: 10.1016/j.ijhydene.2012.12.026.

[26] J. O. Bockris, "The Hydrogen Economy," *Environ. Chem.*, pp. 549–582, 1977, doi:

10.1007/978-1-4615-6921-3_17.

[27] International Energy Agency, “Hydrogen,” *https://www.iea. org/fuels-and-technologies/hydrogen (accessed on 2020-12-17)*, 2020. .

[28] International Energy Agency, “Technology Roadmap: Hydrogen and fuel cells,” 2015.

[29] “The Roadmap Report-Towards 2040: A Guide to Automotive Propulsion Technologies.,” Coventry, 2018.

[30] C. Cluzel and A. Hope-Morley, “Transport Energy Infrastructure Roadmap to 2050,” 2015.

[31] J. Adolf *et al.*, “Energy of the future: Sustainable mobility through fuel cells and H2; Shell hydrogen study,” 2017.

[32] R. Pinsky, P. Sabharwall, J. Hartvigsen, and J. O’Brien, “Comparative review of hydrogen production technologies for nuclear hybrid energy systems,” *Prog. Nucl. Energy*, vol. 123, May 2020, doi: 10.1016/j.pnucene.2020.103317.

[33] International Energy Agency, “Global hydrogen demand by sector in the Sustainable Development Scenario, 2019-2070,” *https://www.iea.org/data-and-statistics/charts/global-hydrogen-demand-by-sector-in-the-sustainable-development-scenario-2019-2070 (accesses on 2020/12/17)*, 2020. .

[34] C. San Marchi *et al.*, “Overview of the DOE hydrogen safety, codes and standards program, part 3: Advances in research and development to enhance the scientific basis for hydrogen regulations, codes and standards,” *Int. J. Hydrogen Energy*, vol. 42, no. 11, pp. 7263–7274, 2017, doi: 10.1016/j.ijhydene.2016.07.014.

[35] A. Baroutaji, T. Wilberforce, M. Ramadan, and A. G. Olabi, “Comprehensive investigation on hydrogen and fuel cell technology in the aviation and aerospace sectors,” *Renew. Sustain. Energy Rev.*, vol. 106, no. September 2018, pp. 31–40, 2019, doi: 10.1016/j.rser.2019.02.022.

[36] J. D. Holladay, J. Hu, D. L. King, and Y. Wang, “An overview of hydrogen production technologies,” *Catalysis Today*. 2009, doi: 10.1016/j.cattod.2008.08.039.

[37] P. Nikolaidis and A. Poullikkas, “A comparative overview of hydrogen production processes,” *Renew. Sustain. Energy Rev.*, vol. 67, pp. 597–611, Jan. 2017, doi: 10.1016/j.rser.2016.09.044.

[38] M. El-Shafie, S. Kambara, and Y. Hayakawa, “Hydrogen Production Technologies Overview,” *J. Power Energy Eng.*, vol. 07, no. 01, pp. 107–154, 2019, doi:

10.4236/jpee.2019.71007.

[39] H. Nazir *et al.*, “Is the H2 economy realizable in the foreseeable future? Part I: H2 production methods,” *Int. J. Hydrogen Energy*, vol. 45, no. 27, pp. 13777–13788, May 2020, doi: 10.1016/j.ijhydene.2020.03.092.

[40] K. Harrison and J. I. Levene, “Electrolysis of water,” in *Solar Hydrogen Generation: Toward a Renewable Energy Future*, 2008.

[41] P. R. Pateras, “MOTOR COMPRESSOR APPARATUS,” US Patent 1,629,928, 1927.

[42] P. R. Pateras, “Motor-compressor apparatus,” U.S. Patent 1,657,641, 1928.

[43] C. Guo, Z. Zuo, H. Feng, B. Jia, and T. Roskilly, “Review of recent advances of free-piston internal combustion engine linear generator,” *Appl. Energy*, vol. 269, p. 115084, Jul. 2020, doi: 10.1016/j.apenergy.2020.115084.

[44] M. R. Hanipah, R. Mikalsen, and A. P. Roskilly, “Recent commercial free-piston engine developments for automotive applications,” *Applied Thermal Engineering*. 2015, doi: 10.1016/j.applthermaleng.2014.09.039.

[45] R. Mikalsen and A. P. Roskilly, “The design and simulation of a two-stroke free-piston compression ignition engine for electrical power generation,” *Appl. Therm. Eng.*, 2008, doi: 10.1016/j.applthermaleng.2007.04.009.

[46] B. Jia, A. Smallbone, Z. Zuo, H. Feng, and A. P. Roskilly, “Design and simulation of a two- or four-stroke free-piston engine generator for range extender applications,” *Energy Convers. Manag.*, 2016, doi: 10.1016/j.enconman.2015.12.063.

[47] Y. Wang, L. Chen, B. Jia, and A. P. Roskilly, “Experimental study of the operation characteristics of an air-driven free-piston linear expander,” *Appl. Energy*, 2017, doi: 10.1016/j.apenergy.2017.03.032.

[48] H. Feng *et al.*, “Research on combustion process of a free piston diesel linear generator,” *Appl. Energy*, 2016, doi: 10.1016/j.apenergy.2015.10.069.

[49] B. Jia, A. Smallbone, R. Mikalsen, K. V. Shivaprasad, S. Roy, and A. P. Roskilly, “Performance analysis of a flexi-fuel turbine-combined free-piston engine generator,” *Energies*, vol. 12, no. 14, 2019, doi: 10.3390/en12142657.

[50] B. Jia, Z. Zuo, H. Feng, G. Tian, A. Smallbone, and A. P. Roskilly, “Effect of closed-loop controlled resonance based mechanism to start free piston engine generator: Simulation and test results,” *Appl. Energy*, vol. 164, pp. 532–539, Feb. 2016, doi: 10.1016/j.apenergy.2015.11.105.

[51] H. Geng *et al.*, “Study on HCCI combustion improvement by using dual assisted compression ignition (DACI) on a hydraulic free piston engine fueled with methanol fuel,” *Appl. Therm. Eng.*, vol. 167, Feb. 2020, doi: 10.1016/j.applthermaleng.2019.114782.

[52] P. Heyl and H. Quack, “Free piston expander-compressor for CO2-design, applications and results,” in *the 20th international congress of refrigeration Sydney*, 1999.

[53] A. A. Kornhauser, “Dynamics and Thermodynamics of a Free-Piston Expander-Compressor,” in *International Mechanical Engineering Congress & Exposition*, 2011.

[54] Y. Xu, X. Xue, Y. Wang, and M. Ai, “Performance characteristics of compressed air-driven free-piston linear generator (FPLG) system – A simulation study,” *Appl. Therm. Eng.*, vol. 160, Sep. 2019, doi: 10.1016/j.applthermaleng.2019.114013.

[55] B. Zhang, X. Peng, Z. He, Z. Xing, and P. Shu, “Development of a double acting free piston expander for power recovery in transcritical CO2 cycle,” *Appl. Therm. Eng.*, 2007, doi: 10.1016/j.applthermaleng.2006.05.034.

[56] B. S. Preetham and L. Weiss, “Investigations of a new free piston expander engine cycle,” *Energy*, 2016, doi: 10.1016/j.energy.2016.03.082.

[57] S. P. Burugupally and L. Weiss, “Design and performance of a miniature free piston expander,” *Energy*, vol. 170, pp. 611–618, Mar. 2019, doi: 10.1016/j.energy.2018.12.158.

[58] S. P. Burugupally, L. Weiss, and C. Depcik, “The effect of working fluid properties on the performance of a miniature free piston expander for waste heat harvesting,” *Appl. Therm. Eng.*, vol. 151, pp. 431–438, Mar. 2019, doi: 10.1016/j.applthermaleng.2019.02.035.

[59] Y. Han, J. Kang, G. Zhang, Z. Liu, J. Tian, and J. Chai, “Performance evaluation of free piston compressor coupling organic Rankine cycle under different operating conditions,” *Energy Convers. Manag.*, vol. 86, pp. 340–348, 2014, doi: 10.1016/j.enconman.2014.05.041.

[60] Y. Han, J. Kang, X. Wang, Z. Liu, J. Tian, and Y. Wang, “Modelling and simulation analysis of an ORC-FPC waste heat recovery system for the stationary CNG-fuelled compressor,” *Appl. Therm. Eng.*, vol. 87, pp. 481–490, Jun. 2015, doi: 10.1016/j.applthermaleng.2015.05.039.

[61] X. Hou *et al.*, "Free piston expander-linear generator used for organic Rankine cycle waste heat recovery system," *Appl. Energy*, 2017, doi: 10.1016/j.apenergy.2017.09.024.

[62] Y. Xu *et al.*, "Experimental investigation of a free piston expander-linear generator with different valve timings," *Appl. Therm. Eng.*, vol. 142, pp. 555–565, Sep. 2018, doi: 10.1016/j.applthermaleng.2018.07.050.

[63] G. Li *et al.*, "Preliminary development of a free piston expander-linear generator for small-scale Organic Rankine Cycle (ORC) waste heat recovery system," *Energies*, 2016, doi: 10.3390/en9040300.

[64] F. Yang, H. Zhang, X. Hou, Y. Tian, and Y. Xu, "Experimental study and artificial neural network based prediction of a free piston expander-linear generator for small scale organic Rankine cycle," *Energy*, vol. 175, pp. 630–644, May 2019, doi: 10.1016/j.energy.2019.03.099.

[65] Y. Tian *et al.*, "Experimental study on free piston linear generator (FPLG) used for waste heat recovery of vehicle engine," *Appl. Therm. Eng.*, vol. 127, pp. 184–193, Dec. 2017, doi: 10.1016/j.applthermaleng.2017.08.031.

[66] Y. Xu *et al.*, "Experimental and simulation study of a free piston expander–linear generator for small-scale organic Rankine cycle," *Energy*, vol. 161, pp. 776–791, Oct. 2018, doi: 10.1016/j.energy.2018.07.171.

[67] X. Hou *et al.*, "Performance investigation of a free piston expander-linear generator for small scale organic Rankine cycle," *Appl. Therm. Eng.*, vol. 144, pp. 209–218, Nov. 2018, doi: 10.1016/j.applthermaleng.2018.08.059.

[68] T. Zhao *et al.*, "Modelling and validation of a free piston expander-linear generator for waste heat recovery system," *Appl. Therm. Eng.*, vol. 163, Dec. 2019, doi: 10.1016/j.applthermaleng.2019.114377.

[69] X. Hou *et al.*, "A comparison study and performance analysis of free piston expander-linear generator for organic Rankine cycle system," *Energy*, vol. 167, pp. 136–143, Jan. 2019, doi: 10.1016/j.energy.2018.10.196.

[70] J. Li *et al.*, "Comparative analysis of different valve timing control methods for single-piston free piston expander-linear generator via an orthogonal experimental design," *Energy*, vol. 195, Mar. 2020, doi: 10.1016/j.energy.2020.116966.

[71] Y. Tian *et al.*, "Development and validation of a single-piston free piston expander-

linear generator for a small-scale organic Rankine cycle," *Energy*, vol. 161, pp. 809–820, Oct. 2018, doi: 10.1016/j.energy.2018.07.192.

[72] J. Li *et al.*, "Performance analysis of a single-piston free piston expander-linear generator with intake timing control strategy based on piston displacement," *Appl. Therm. Eng.*, vol. 152, pp. 751–761, Apr. 2019, doi: 10.1016/j.applthermaleng.2019.02.121.

[73] G. B. Warren and J. W. Bjerkiie, "Proppsed Reciprocating Internai Combustion Engine with Constant Pressure Combustion Combustion Chamber Separateci from Cylinders (Modified Brayton Cycle) soc," *SAE Tech. Pap.*, 1969.

[74] R. Decher, "The Britalus Brayton Cycle Engine," *Int. Gas Turbine Conf. Exhib. Am. Soc. Mech. Eng. Digit. Collect.*, 1984.

[75] G. A. Tsongas and T. J. White, "A Parametric Analysis Microcomputer Model for Evaluating the Thermodynamic Performance of a Reciprocating Brayton Cycle Engine," *J. Eng. Gas Turbines Power* , pp. 587–594, 1989.

[76] R. J. Rosa, "Characteristics of a closed Brayton cycle piston engine.," in *[Proceedings] WESCANEX'91 IEEE*, 1991, pp. 153–159.

[77] K. Craven, N. Clark, and J. E. Smith, "Initial Investigations of a Novel Engine Concept for Use with a Wide Range of Fuel Types," *SAE Tech. Pap.*, vol. No 920057, 1992.

[78] K. Craven and N. Clark, "Ideal Computer Analysis of a Novel Engine Concept," *SAE Tech. Pap.*, vol. (No. 96008, 1996.

[79] S. Bonnet, M. Alaphilippe, and P. Stouffs, "Exergy and exergo-economic analysis of a microcogeneration system based on an Ericsson engine," in *ECOS 2005 - Proceedings of the 18th International Conference on Efficiency, Cost, Optimization, Simulation, and Environmental Impact of Energy Systems*, 2005, pp. 453–460.

[80] S. Bonnet, M. Alaphilippe, and P. Stouffs, "Energy, exergy and cost analysis of a micro-cogeneration system based on an Ericsson engine," *Int. J. Therm. Sci.*, 2005, doi: 10.1016/j.ijthermalsci.2005.09.005.

[81] M. ALAPHİLİPPE, S. BONNET, and P. STOUFFS, "Low Power Thermodynamic Solar Energy Conversion: Coupling of a Parabolic Trough Concentrator and an Ericsson Engine," *Int. J. Thermodyn.*, vol. 10, no. 1, pp. 37–45, Mar. 2007.

[82] J. Wojewoda and Z. Kazimierski, "Numerical model and investigations of the externally heated valve Joule engine," *Energy*, vol. 35, no. 5, pp. 2099–2108, 2010,

doi: 10.1016/j.energy.2010.01.028.

[83] A. Touré and P. Stouffs, "Modeling of the Ericsson engine," *Energy*, vol. 76, pp. 445–452, 2014, doi: 10.1016/j.energy.2014.08.030.

[84] F. Lontsi, O. Hamandjoda, K. Fozao, P. Stouffs, and J. Nganhou, "Dynamic simulation of a small modified Joule cycle reciprocating Ericsson engine for micro-cogeneration systems," *Energy*, 2013, doi: 10.1016/j.energy.2013.10.061.

[85] F. Lontsi, O. Hamandjoda, K. F. Djanna, P. Stouffs, and J. Nganhou, "Dynamic modeling of a small open joule cycle reciprocating Ericsson engine: Simulation results," *Energy Sci. Eng.*, vol. 1, no. 3, pp. 109–117, 2013, doi: 10.1002/ese3.13.

[86] M. Creyx, E. Delacourt, C. Morin, and B. Desmet, "Dynamic modelling of the expansion cylinder of an open Joule cycle Ericsson engine: A bond graph approach," *Energy*, vol. 102, pp. 31–43, May 2016, doi: 10.1016/J.ENERGY.2016.01.106.

[87] H. Hachem *et al.*, "Comparison based on exergetic analyses of two hot air engines: A Gamma type Stirling engine and an open joule cycle Ericsson engine," *Entropy*, vol. 17, no. 11, pp. 7331–7348, 2015, doi: 10.3390/e17117331.

[88] D. Stanciu and V. Bădescu, "Solar-driven Joule cycle reciprocating Ericsson engines for small scale applications. From improper operation to high performance," *Energy Convers. Manag.*, vol. 135, pp. 101–116, 2017, doi: 10.1016/j.enconman.2016.12.070.

[89] J.-F. Oudkerk and V. Lemort, "Development of an Ericsson Heat Engine for biomass Combined Heat and Power," in *the 30th International conference on Efficiency, Cost, Optimization, Simulation and Environmental Impact of Energy Systems (ECOS)*, 2017.

[90] N. P. Komninos and E. D. Rogdakis, "Design considerations for an Ericsson engine equipped with high-performance gas-to-gas compact heat exchanger: A numerical study," *Appl. Therm. Eng.*, vol. 133, pp. 749–763, 2018, doi: 10.1016/j.applthermaleng.2018.01.078.

[91] N. P. Komninos and E. D. Rogdakis, "Numerical investigation into the effect of compressor and expander valve timings on the performance of an Ericsson engine equipped with a gas-to-gas heat exchanger," *Energy*, vol. 163, pp. 1077–1092, 2018, doi: 10.1016/j.energy.2018.08.132.

[92] M. N. Ngangué and P. Stouffs, "Dynamic simulation of an original Joule cycle liquid pistons hot air Ericsson engine," *Energy*, vol. 190, Jan. 2020, doi:

10.1016/j.energy.2019.116293.

[93] D. Wu, A. S. Jalal, and N. Baker, “A Coupled Model of the Linear Joule Engine with Embedded Tubular Permanent Magnet Linear Alternator,” in *Energy Procedia*, 2017, doi: 10.1016/j.egypro.2017.03.571.

[94] U. Ngwaka *et al.*, “Evaluation of performance characteristics of a novel hydrogen fuelled free-piston engine generator,” *Int. J. Hydrogen Energy*, 2020, doi: https://doi.org/10.1016/j.ijhydene.2020.02.072.

[95] N. M. Hafiz, M. R. A. Mansor, W. M. F. Wan Mahmood, and M. Shioji, “Simulation of the Effect of Initial Temperature and Fuel Injection Pressure on Hydrogen Combustion Characteristics in Argon-Oxygen Compression Ignition Engine,” in *SAE Technical Papers*, 2016, vol. 2016-Octob, doi: 10.4271/2016-01-2227.

[96] N. M. Hafiz, M. R. A. Mansor, W. M. F. W. Mahmood, F. Ibrahim, S. Abdullah, and K. Sopian, “Numerical study of hydrogen fuel combustion in compression ignition engine under argon-oxygen atmosphere,” *J. Teknol.*, vol. 78, no. 6–10, pp. 77–83, 2016, doi: 10.11113/jt.v78.9192.

[97] M. A. A. Nasruldin and M. R. A. Mansor, “Simulation of Hydrogen Combustion Characteristics in Argon-Oxygen Compression Ignition Engine using Large Eddy Simulation (LES) Turbulence Model,” in *IOP Conference Series: Earth and Environmental Science*, 2019, vol. 354, no. 1, doi: 10.1088/1755-1315/354/1/012056.

[98] L. Li, Y. Gong, J. Deng, and X. Gong, “CO2 Reduction Request and Future High-Efficiency Zero-Emission Argon Power Cycle Engine,” *Automot. Innov.*, vol. 1, no. 1, pp. 43–53, Jan. 2018, doi: 10.1007/s42154-018-0007-y.

[99] M. Shahsavan, M. Morovatiyan, and J. H. Mack, “A Computational Investigation of Nonpremixed Combustion of Natural Gas Injected into Mixture of Argon and Oxygen,” *J. Eng. Gas Turbines Power*, vol. 141, no. 8, Aug. 2019, doi: 10.1115/1.4043277.

[100] M. Shahsavan, M. Morovatiyan, and J. H. Mack, “The influence of mixedness on ignition for hydrogen direct injection in a constant volume combustion chamber,” in *2018 Spring Technical Meeting of the Eastern States Section of the Combustion Institute, ESSCI 2018*, 2018, vol. 2018-March.

[101] M. Shahsavan, M. Morovatiyan, and J. H. Mack, “A numerical investigation of

hydrogen injection into noble gas working fluids," *Int. J. Hydrogen Energy*, vol. 43, no. 29, pp. 13575–13582, 2018, doi: 10.1016/j.ijhydene.2018.05.040.

[102] N. J. Killingsworth, V. H. Rapp, D. L. Flowers, S. M. Aceves, J.-Y. Chen, and R. Dibble, "Characteristics of knock in hydrogen-oxygen-argon SI engine," in *Western States Section of the Combustion Institute Spring Technical Meeting 2010*, 2010, pp. 772–778.

[103] M. Shahsavan and J. H. Mack, "The Effect of Heavy Working Fluids on Hydrogen Combustion," in *110th U. S. National Combustion Meeting*, 2017, pp. 1–6, doi: 10.17605/OSF.IO/94S8D.

[104] M. Shahsavan and J. H. Mack, "Mixedness Measurement in Gaseous Jet Injection," in *American Society for Engineering Education Northeast Section (ASEE-NE) Annual Conference April 27-29,, Massachusetts*, 2017, pp. 1–4.

[105] R. V. Ravikrishna and A. B. Sahu, "Advances in understanding combustion phenomena using non-premixed and partially premixed counterflow flames: A review," *International Journal of Spray and Combustion Dynamics*, vol. 10, no. 1. SAGE Publications Inc., pp. 38–71, 01-Mar-2018, doi: 10.1177/1756827717738168.

[106] N. M. Hafiz, M. R. A. Mansor, and W. M. F. Wan Mahmood, "Simulation of the combustion process for a CI hydrogen engine in an argon-oxygen atmosphere," *Int. J. Hydrogen Energy*, vol. 43, no. 24, pp. 11286–11297, Jun. 2018, doi: 10.1016/J.IJHYDENE.2018.05.022.

[107] R. Kuroki, A. Kato, E. Kamiyama, and D. Sawada, "Study of High Efficiency Zero-Emission Argon Circulated Hydrogen Engine," in *SAE Technical Paper Series*, 2010, doi: 10.4271/2010-01-0581.

[108] M. S. Aznar *et al.*, "Experimental Investigation of Port and Direct Injection Strategies for Internal Combustion Engines with Argon as the Working Fluid," in *Proceedings of the European Combustion Meeting 2017*, 2017, doi: 10.17605/OSF.IO/PT67Q.

[109] M. R. A. Mansor, S. Nakao, K. Nakagami, M. Shioji, and A. Kato, "Ignition Characteristics of Hydrogen Jets in an Argon-Oxygen Atmosphere," in *SAE Technical Paper Series*, 2012, doi: 10.4271/2012-01-1312.

[110] E. A. Laumann and R. K. Reynolds, "Hydrogen-fueled engine," *U.S. Pat.*, vol. 4, no. 112, p. 875, 1978.

[111] P. C. T. De Boer and J. F. Hulet, "Performance of a hydrogen-oxygen-noble gas

engine.," *Int. J. Hydrogen Energy*, vol. 5, no. 4, pp. 437–452, 1980.

[112] M. Ikegami, K. Miwa, and M. Shioji, "A study of hydrogen fuelled compression ignition engines," *Int. J. Hydrogen Energy*, 1982, doi: 10.1016/0360-3199(82)90127-6.

[113] N. J. Killingsworth, V. H. Rapp, D. L. Flowers, S. M. Aceves, J. Y. Chen, and R. Dibble, "Increased efficiency in SI engine with air replaced by oxygen in argon mixture," *Proc. Combust. Inst.*, 2011, doi: 10.1016/j.proci.2010.07.035.

[114] E. Zhang *et al.*, "Cyclic Variations of Argon Power Cycle Engine with Fuel of Hydrogen," in *SAE Technical Paper Series*, 2017, doi: 10.4271/2017-01-2409.

[115] Y. Gong, Y. Zhan, J. Deng, and Z. Wu, "Experimental and Numerical Study on Combustion Characteristics of Hydrogen-Argon Jet in a Hot Vitiated Co-flow," *SAE Tech. Pap.*, 2018.

[116] M. R. A. Mansor, S. Nakao, K. Nakagami, and Shioji M., "Study on Hydrogen-Jet Development in the Argon Atmosphere," *Yao T. Zero-Carbon Energy Kyoto 2011. Green Energy Technol. Springer, Tokyo* , 2012.

[117] M. R. A. Mansor and M. Shioji, "Characterization of hydrogen jet development in an argon atmosphere," *Yao T. Zero-Carbon Energy Kyoto 2012. Green Energy Technol. Springer, Tokyo.* , pp. 133–140, 2013.

[118] M. R. A. Mansor and M. Shioji, "Investigation of the combustion process of hydrogen jets under argon-circulated hydrogen-engine conditions," *Combust. Flame*, 2016, doi: 10.1016/j.combustflame.2016.07.032.

[119] M. Sierra-Aznar *et al.*, "Working fluid replacement in gaseous direct-injection internal combustion engines: A fundamental and applied experimental investigation," in *10th U.S. National Combustion Meeting*, 2017, vol. 2017-April.

[120] M. S. Aznar, F. Chorou, J.-Y. Chen, A. Dreizler, and R. W. Dibble, "Experimental and Numerical Investigation of the Argon Power Cycle," in *ASME 2018 Internal Combustion Engine Division Fall Technical Conference.*, 2018.

[121] W. F. Li, Z. C. Liu, J. Tian, Z. S. Wang, and Y. Xu, "Effects of argon dilution on the thermal efficiency and exhaust emissions of a NG engine," *Int. J. Automot. Technol.*, vol. 16, no. 5, pp. 721–731, 2015, doi: 10.1007/s12239-015-0073-7.

[122] W. Li, Z. Liu, Z. Wang, C. Li, L. Duan, and H. Zuo, "Effect of CO 2, N 2, and Ar on Combustion and Exhaust Emissions Performance in a Stoichiometric Natural Gas

Engine," *SAE Tech. Pap.*, vol. No. 2014-01-2693, 2014.

[123] H. A. Moneib, M. Abdelaal, M. Y. E. Selim, and O. A. Abdallah, "NOx emission control in SI engine by adding argon inert gas to intake mixture," *Energy Convers. Manag.*, vol. 50, no. 11, pp. 2699–2708, Nov. 2009, doi: 10.1016/J.ENCONMAN.2009.05.032.

[124] J. Deng, H. Zhong, Y. Gong, X. Gong, and L. Li, "Studies on injection and mixing characteristics of high pressure hydrogen and oxygen jet in argon atmosphere," *Fuel*, vol. 226, pp. 454–461, Aug. 2018, doi: 10.1016/j.fuel.2018.04.038.

[125] J. Deng, X. Gong, Y. Zhan, Y. Gong, and L. Li, "Experiment on combustion characteristics of natural gas in cylinder under Ar-O atmosphere," *Neiranji Xuebao/Transactions CSICE (Chinese Soc. Intern. Combust. Engines)*, vol. 35, no. 1, pp. 38–43, 2017, doi: 10.16236/j.cnki.nrjxb.201701006.

[126] J. Zhang, D. Han, and Z. Huang, "Second-law thermodynamic analysis for premixed hydrogen flames with diluents of argon/nitrogen/carbon dioxide," *Int. J. Hydrogen Energy*, vol. 44, no. 10, pp. 5020–5029, Feb. 2019, doi: 10.1016/J.IJHYDENE.2019.01.041.

[127] A. Korsunovs, F. Campean, G. Pant, O. Garcia-Afonso, and E. Tunc, "Evaluation of zero-dimensional stochastic reactor modelling for a Diesel engine application," *Int. J. Engine Res.*, vol. 21, no. 4, pp. 592–609, Apr. 2020, doi: 10.1177/1468087419845823.

[128] U. C. Ngwaka, C. Diyoke, and N. Anosike, "Single Zone, Zero Dimensional Model of Diesel Multiple-Injection," *Energy Power Eng.*, vol. 08, no. 09, pp. 297–312, 2016, doi: 10.4236/epe.2016.89028.

[129] R. Mikalsen and A. P. Roskilly, "Coupled dynamic-multidimensional modelling of free-piston engine combustion," *Appl. Energy*, 2009, doi: 10.1016/j.apenergy.2008.04.012.

[130] S. S. Goldsborough and P. Van Blarigan, "Optimizing the Scavenging System for a Two-Stroke Cycle, Free Piston Engine for High Efficiency and Low Emissions: A Computational Approach," in *SAE Technical Paper Series*, 2010, doi: 10.4271/2003-01-0001.

[131] J. Mao, Z. Zuo, and H. Feng, "Parameters coupling designation of diesel free-piston linear alternator," *Appl. Energy*, 2011, doi: 10.1016/j.apenergy.2011.05.051.

[132] J. Mao, Z. Zuo, W. Li, and H. Feng, "Multi-dimensional scavenging analysis of a free-

piston linear alternator based on numerical simulation," *Appl. Energy*, 2011, doi: 10.1016/j.apenergy.2010.10.003.

[133] M. W. CHASE Jr., "NIST-JANAF Thermochemical Tables Fourth Edition," *J. Phys. Chem. Ref. Data, Monogr.*, vol. 9, 1998.

[134] P. K. Bansal and T. C. Chin, "Modelling and optimisation of wire-and-tube condenser," *Int. J. Refrig.*, vol. 26, no. 5, pp. 601–613, 2003.

[135] T. L. Bergman, F. P. Incropera, D. P. DeWitt, and A. S. Lavine, *Fundamentals of Heat and Mass Transfer*, 7th ed. John Wiley & Sons, 2011.

[136] B. R. Munson, D. F. Young, T. H. Okiishi, and W. W. Huebsch, *Fundamentals of Fluid Mechanics*, Sixth. John Wiley & Sons, 2009.

[137] B. Jia, Z. Zuo, G. Tian, H. Feng, and A. P. Roskilly, "Development and validation of a free-piston engine generator numerical model," *Energy Convers. Manag.*, vol. 91, pp. 333–341, Feb. 2015, doi: 10.1016/J.ENCONMAN.2014.11.054.

[138] G. F. Hohenberg, "Advanced Approaches for Heat Transfer Calculations," in *SAE Technical Paper Series*, 1979, pp. 2788–2806, doi: 10.4271/790825.

[139] J. B. Heywood, *Internal Combustion Engine Fundamentals by John B. Heywood*. New York: McGraw-Hill, 1988.

[140] S. A. Nasar, S. A., & Nasar, *Handbook of electric machines*. New York: Mcgraw-hill, 1987.

[141] S. A. Boldea, I., & Nasar, "Linear electric actuators and generators," *IEEE Trans. Energy Convers.*, vol. 14, no. 3, pp. 712–717, 1999.

[142] N. J. Baker, R. M. Korbekandi, D. Wu, and A. Jalal, "An investigation of short translator linear machines for use in a free piston engine," in *In 2019 IEEE International Electric Machines & Drives Conference (IEMDC)*, 2019, pp. 68–73.

[143] J. Subramanian and P. Famouri, "Analysis of Neutral position, Magnet–Spacer of Tubular Permanent Magnet Linear generator for FPE applications," in *In 2019 IEEE 28th International Symposium on Industrial Electronics (ISIE)*, 2019, pp. 232–237.

[144] H. Schillingmann, Q. Maurus, and M. Henke, "Linear Generator Design for a Free-Piston Engine with high Force Density," in *In 2019 12th International Symposium on Linear Drives for Industry Applications (LDIA)*, 2019, pp. 1–6.

[145] J. Wang and N. J. Baker, "A linear laminated cylindrical transverse flux machine for use with a free piston engine," *IEEE Trans. Energy Conversion,* vol. 33, no. 4, pp.

1988–1997, 2018.

[146] N. J. Baker, A. Sa Jalal, J. Wang, and R. M. Korbekandi, “Experimental comparison of two linear machines developed for the free piston engine,” *J. Eng.*, vol. 2019, no. 17, pp. 4406–4410, Jun. 2019, doi: 10.1049/joe.2018.8214.

[147] J. F. Gieras, “Linear Electric Motors,” in *Electric power generation, transmission, and distribution*, 3rd ed., L. L. Grigsby, Ed. CRC press, 2016.

[148] B. Jia, “Analysis and control of a spark ignition free-piston engine generator,” Newcastle University, 2016.

[149] B. Jia, Z. Zuo, G. Tian, H. Feng, and A. P. Roskilly, “Development and validation of a free-piston engine generator numerical model,” *Energy Convers. Manag.*, 2015, doi: 10.1016/j.enconman.2014.11.054.

[150] H. Polinder, J. G. Slootweg, M. J. Hoeijmakers, and J. C. Compter, “Modelling of a linear PM machine including magnetic saturation and end effects: Maximum force to current ratio,” in *IEMDC 2003 - IEEE International Electric Machines and Drives Conference*, 2003, doi: 10.1109/IEMDC.2003.1210328.

[151] L. Luo, Y. Wang, H. Chen, X. Zhang, and T. Roskilly, “ORC units driven by engine waste heat - A simulation study,” in *Energy Procedia*, 2017, vol. 142, pp. 1022–1027, doi: 10.1016/j.egypro.2017.12.349.

[152] Z. Qiao and S. Sun, “Two-phase fluid simulation using a diffuse interface model with Peng--Robinson equation of state,” *SIAM J. Sci. Comput.*, vol. 36, no. 4, pp. 708–728, 2014.

[153] B. J. McBride, S. Gordon, and M. A. Reno, “Coefficients for Calculating Thermodynamic and Transport Properties of Individual Species,” NASA, 1993.

[154] C. L. Yaws, *The Yaws handbook of vapor pressure: Antoine coefficients*. Gulf Professional Publishing., 2015.

[155] P. J. Linstrom and G. Mallard, M, Eds., “NIST Chemistry WebBook,” *NIST Standard Reference Database Number 69*. .

[156] R. C. Reid, J. M. Prausnitz, and B. E. Poling, *The Properties of Gases and Liquids*, 4th ed. New York: McGraw-Hill, 1987.

[157] B. E. Poling, J. M. Prausnitz, and J. P. O’connell, *The properties of gases and liquids*, 5th ed. New York: Mcgraw-hill, 2001.

[158] I. L. Drell and F. E. Belles, “Survey of hydrogen combustion properties,” 1957.

[159] U. Ngwaka *et al.*, “Evaluation of performance characteristics of a novel hydrogen-fuelled free-piston engine generator,” *Int. J. Hydrogen Energy*, 2020, doi: 10.1016/j.ijhydene.2020.02.072.

[160] F. Cater, M. S., Bolander, N. W., & Sadeghi, “Experimental investigation of surface modifications for piston-ring/cylinder-liner friction reduction,” in *In ASME 2008 Internal Combustion Engine Division Spring Technical Conference*, 2008, pp. 355–365.

[161] B. Jia, R. Mikalsen, A. Smallbone, and A. P. Roskilly, “A study and comparison of frictional losses in free-piston engine and crankshaft engines,” *Appl. Therm. Eng.*, 2018, doi: 10.1016/j.applthermaleng.2018.05.018.

[162] C. L. Tian, H. H. Feng, and Z. X. Zuo, “Oscillation Characteristic of Single Free Piston Engine Generator,” *Adv. Mater. Res.*, 2011, doi: 10.4028/www.scientific.net/amr.383-390.1873.

[163] C. Zhang *et al.*, “A free-piston linear generator control strategy for improving output power,” *Energies*, 2018, doi: 10.3390/en11010135.

[164] Y. Xu *et al.*, “Experimental and simulation study of a free piston expander–linear generator for small-scale organic Rankine cycle,” *Energy*, vol. 161, pp. 776–791, 2018, doi: 10.1016/j.energy.2018.07.171.

[165] S. S. Goldsborough and P. Van Blarigan, “A Numerical Study of a Free Piston IC Engine Operating on Homogeneous Charge Compression Ignition Combustion,” in *SAE Technical Paper Series*, 2010, doi: 10.4271/1999-01-0619.

[166] C. Lee, “Turbine-Compound Free-Piston Linear Alternator Engine,” University of Michigan, 2014.

[167] S. Gusev, D. Ziviani, J. Vierendeels, and M. De Paepe, “Variable volume ratio free-piston expander: Prototyping and experimental campaign | Détendeur à piston libre à rapport volumique variable : Prototypage et étude expérimentale,” *Int. J. Refrig.*, vol. 98, pp. 70–79, 2019, doi: 10.1016/j.ijrefrig.2018.10.004.

[168] C. M. Atkinson *et al.*, “Numerical Simulation of a Two-Stroke Linear Engine-Alternator Combination,” in *SAE Technical Paper Series*, 2010, vol. 1, doi: 10.4271/1999-01-0921.

[169] H. Feng, Y. Song, Z. Zuo, J. Shang, Y. Wang, and A. P. Roskilly, “Stable operation and electricity generating characteristics of a single-cylinder free piston engine linear

generator: Simulation and experiments," *Energies*, 2015, doi: 10.3390/en8020765.

[170] C. Yuan, J. Xu, and Y. He, "Parametric study on the starting of a free-piston engine alternator," *Int. J. Engine Res.*, 2018, doi: 10.1177/1468087417712161.

[171] Y. Wakuri, M. Soejima, Y. Ejima, T. Hamatake, and T. Kitahara, "Studies on Friction Characteristics of Reciprocating Engines," in *SAE Technical Paper Series*, 2010, doi: 10.4271/952471.

[172] D. Taraza, N. Henein, and W. Bryzik, "Friction Losses in Multi-Cylinder Diesel Engines," in *SAE Technical Paper Series*, 2010, doi: 10.4271/2000-01-0921.

[173] B. Jia, A. Smallbone, H. Feng, G. Tian, Z. Zuo, and A. P. Roskilly, "A fast response free-piston engine generator numerical model for control applications," *Appl. Energy*, 2016, doi: 10.1016/j.apenergy.2015.10.108.

[174] B. Jia, Z. Zuo, A. Smallbone, H. Feng, and A. P. Roskilly, "A decoupled design parameter analysis for free-piston engine generators," *Energies*, 2017, doi: 10.3390/en10040486.

[175] M. Wiercigroch, V. W. T. Sin, and Z. F. K. Liew, "Non-reversible dry friction oscillator: Design and measurements," *Proc. Inst. Mech. Eng. Part C J. Mech. Eng.*, 1999, doi: 10.1243/0954406991522752.

[176] A. Stefański, J. Wojewoda, M. Wiercigroch, and T. Kapitaniak, "Chaos caused by non-reversible dry friction," *Chaos, Solitons and Fractals*, 2003, doi: 10.1016/S0960-0779(02)00451-4.

[177] J. Powell and M. Wiercigroch, "Influence of non-reversible Coulomb characteristics on the response of a harmonically excited linear oscillator," *Mach. Vib*, vol. 1, no. 2, pp. 94–104, 1992.